

A modeling study of  
teleconnections and their  
tropical sources

Iris Manola

The cover is designed by Vasilis Revezikas. The theme is based on “The Starry Night” by Vincent van Gogh.

ISBN: 978-90-5335-900-6

Printing: Ridderprint BV

# A modeling study of teleconnections and their tropical sources

Een modelstudie van teleconnecties en hun tropische herkomst  
(met een samenvatting in het Nederlands)

Μελέτη μοντελοποίησης τηλεσυνδέσεων και των τροπικών πηγών  
τους  
(με περίληψη στα Ελληνικά)

Proefschrift

ter verkrijging van de graad van doctor aan de Universiteit Utrecht  
op gezag van de rector magnificus, prof.dr. G.J. van der Zwaan,  
ingevolge het besluit van het college voor promoties in het  
openbaar te verdedigen op

maandag 22 september 2014 des ochtends te 10.30 uur

door

**Iris Manola**

geboren 9 september 1982  
te Athene, Griekenland

Promotoren: Prof. dr. W.P.M. de Ruijter  
Prof. dr. ir. W. Hazeleger

Copromotor: Dr. ir. F. M. Selten

This thesis was accomplished at KNMI with financial support from NWO in the INATEX project part of the ZKO program number 83908434.

*Nature is so powerful, so strong.  
Capturing its essence is not easy -  
your work becomes a dance with light and the weather.  
It takes you to a place within yourself.*  
– Annie Leibovitz



# Contents

<b>1</b>	<b>Introduction</b>	<b>1</b>
1.1	Prologue . . . . .	1
1.2	Jet streams and Rossby waves . . . . .	2
1.3	Extratropical teleconnections due to Rossby waves . . . . .	9
1.4	Tropical teleconnections connected to Indian Ocean variability . . . . .	14
1.5	An overview of this thesis . . . . .	20
<b>2</b>	<b>“Waveguidability” of idealized jets</b>	<b>23</b>
2.1	Introduction . . . . .	24
2.2	Characteristics of Observed Jets . . . . .	27
2.3	Numerical Experiments . . . . .	30
2.4	Waveguidability of Idealised Jets . . . . .	32
2.5	Resonance . . . . .	35
2.6	Conclusions and Discussion . . . . .	38
<b>3</b>	<b>Drivers of North Atlantic Oscillation Events</b>	<b>43</b>
3.1	Introduction . . . . .	44
3.2	The NAO Events . . . . .	47
3.3	Sources of NAO Forcing . . . . .	48
3.4	Model and Experimental Set-Up . . . . .	51
3.5	Tropical and Extratropical Influence on NAO Patterns . . . . .	52
3.6	Summary and Conclusions . . . . .	61
<b>4</b>	<b>An evaluation of the EC-Earth climatology in the Indian Ocean</b>	<b>65</b>
4.1	Introduction . . . . .	66
4.2	Data . . . . .	67
4.3	Boreal Winter Evaluation . . . . .	69

4.4	Boreal Summer Evaluation . . . . .	74
4.5	Monsoon seasonal cycle, SST variability and Indian Ocean thermocline . . . . .	80
4.6	Summary and Conclusions . . . . .	82
<b>5</b>	<b>The Ocean-Atmosphere response to wind-induced Ther- mocline changes in the tropical South Western Indian Oce- an</b>	<b>85</b>
5.1	Introduction . . . . .	87
5.2	Data and Model . . . . .	90
5.3	Experimental Set-Up . . . . .	93
5.4	Simulation Results . . . . .	94
5.5	Summary and Discussion . . . . .	109
<b>6</b>	<b>Conclusions and discussion</b>	<b>113</b>
6.1	Summary of work . . . . .	114
6.2	Outlook . . . . .	116
	<b>Bibliography</b>	<b>119</b>
	<b>Summary</b>	<b>129</b>
	<b>Samenvatting</b>	<b>135</b>
	<b>Περίληψη</b>	<b>141</b>
	<b>Acknowledgements</b>	<b>147</b>
	<b>Curriculum vitae</b>	<b>149</b>



---

# CHAPTER 1

---

## Introduction

### 1.1 Prologue

The weather in Western Europe is dominated by transient disturbances leading to large variations in the weather that are hard to predict as these disturbances have a chaotic character. These weather systems interact with and are steered by large-scale westerly flows that dominate the mid-latitudes. They find their origin in the instability of these large-scale westerly flows. Longer spells of dry, wet, cold or warm weather are caused by persistent configurations of the large scale westerly flows. It is known that these anomalous circulations can be forced remotely by, for instance, the interaction of the circulation with topography, or the forced outflows from tropical deep convection. The physics of these teleconnections is controlled by large-scale waves in the velocity field of the atmosphere, such as Rossby waves.

In this thesis we will study the interaction between the tropical forcing of Rossby waves and the tropical and extratropical response. We will focus on variations in the Indian Ocean, as studies have shown that even the weather in Europe is influenced by variations in the Indian Ocean.

To provide a background of the phenomena and theoretical concepts that are subjects of this thesis, we will first introduce these and conclude this introduction with a brief overview of the later chapters.

## 1.2 Jet streams and Rossby waves

### 1.2.1 Origin of the jet streams

The temporal and spatial scales of the atmospheric motions vary greatly, from the centimeter scale turbulent motions in the planetary boundary layer close to the surface, lasting only for seconds, to the largest 10000 km long waves in the meandering jet streams encompassing each Hemisphere with slow variations well into the decadal time scales. Each scale has its own characteristics and plays its own role in the atmospheric variations. Averaging the motions over the standard climate timescale of 30 years reveals a large scale, well-organised flow structure that is commonly referred to as the “General Atmospheric Circulation”.

Ultimately, it is the energy of the sun that sets the atmosphere into motion. Without this energy input, the atmosphere would just rotate with the planet in a solid body rotation with no relative motions with respect to the surface. At the top of the atmosphere the net incoming solar radiation balances the outgoing longwave radiation in the global and long-term mean. However, in the tropical regions this balance is positive and in the polar regions it is negative. This radiation imbalance creates an equator to pole temperature gradient, with warm air masses in the tropics and cold air masses at the poles. This thermal structure is a reservoir of potential energy that can be used to set the atmosphere into motion with gravity doing the work as cold air is located underneath the warm air. In the warm, less dense air, a pressure gradient develops with higher pressure in the upper tropical atmosphere accelerating the warm tropical air polewards aloft. This lowers the tropical pressure at surface and air is accelerated towards the tropics at surface. The air converges from both Hemispheres in the Inter Tropical Convergence Zone (ITCZ) and moves upwards, fuelled by the release of latent heat in the deep convective systems in the ITCZ. In the upper branch of this circulation cell, referred to as the Hadley Cell, the poleward moving air retains its angular momentum and since it moves closer to the axis of rotation as it moves polewards, the air gains westerly momentum to form a belt of westerly winds, referred to as the jet stream. Around  $30^\circ$  latitude the westerly jet attains its maximum value and becomes unstable and turbulent eddies are formed. These eddies, also known as depressions, unstable baroclinic waves or weather systems, mix the westerly momentum to the surface to form the belts of westerly winds at surface in the mid-latitudes where by

friction the westerly momentum is transferred to the solid Earth and the oceans. In the surface equatorward return flow, conservation of angular momentum leads to easterly winds, the trade winds blowing steadily from the northeast in the Northern Hemisphere and southeast in the Southern Hemisphere. In the Hadley circulation the net poleward heat transport compensates the radiation imbalance at the top of the atmosphere. At the poleward termination of the Hadley cells around  $30^\circ$  latitude, the poleward heat transport is accomplished by the turbulent eddies that advect cold and dry polar air masses equatorward and warm and moist subtropical air masses poleward. In the region of these turbulent eddies, on average air descends around  $30^\circ$  latitude and rises at around  $60^\circ$  latitude forming the so called “Ferrell cell”.

The structure of the annual mean zonal wind for both Hemispheres is shown in Fig. 1.1. We can see the prevailing easterly trade winds in the tropics and the westerlies almost everywhere else. Around the latitude of  $30^\circ\text{N}$  at the height of 200hPa the westerlies gain maximum speed, indicating the position of the major subtropical jet streams. The wind at the surface and the attendant stress is a primary driver of the ocean circulation.

The jet streams have a strong impact on local weather conditions, as they steer the weather systems with their associated temperature fronts and precipitation bands and determine the position of the storm tracks.

The existence of the westerly jets has profound implications for the propagation of Rossby waves as discussed in the next section.

### 1.2.2 Rossby waves and their propagation characteristics

Atmospheric Rossby waves are disturbances from the zonal symmetry in the atmospheric circulation that move westward under the influence of the rotation of the Earth. In this thesis we study Rossby waves that are excited by tropical Rossby wave sources and travel into the extratropics, creating so-called teleconnection patterns. Rossby waves are named after Carl-Gustaf Arvid Rossby (Rossby (1939)) who identified them and explained their westward propagation in 1939. Rossby waves are dispersive, the longer the wavelength the faster the westward propagation. Their propagation is offset by the background winds such that in the region of the westerly winds, only the longest waves retrograde, move against the flow westward, while the smaller waves are carried eastward. The largest waves are called planetary waves. The planetary Rossby waves determine

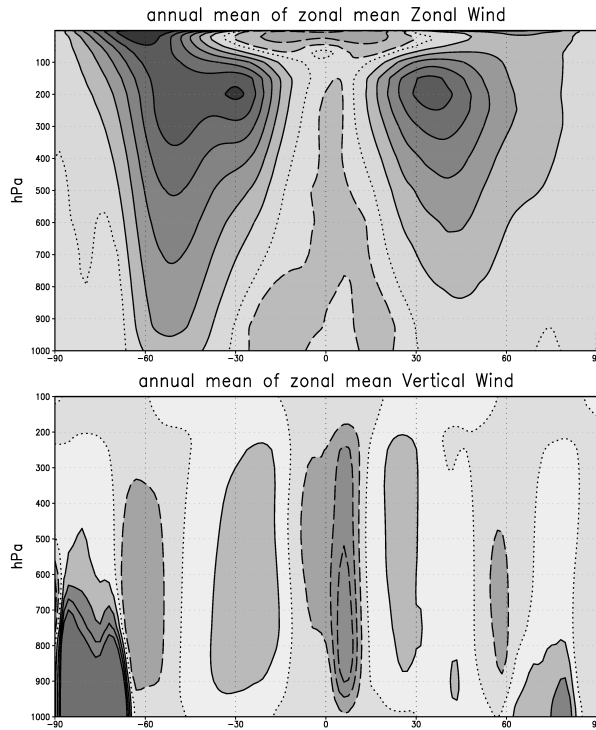


**Figure 1.1:** Top panel: The annual and zonal mean zonal wind. Bottom panel: The annual mean zonal mean vertical wind. The horizontal axis is the latitude from the south to the north pole and the vertical axis is the height in hPa. The data are 5 years averages, from 2008 to 2012, from the ERA-Interim reanalysis (Dee and Coauthors (2011)). For the top panel: the continuous contours indicate the westerly winds and the zero line is indicated by the short dashed contour. The contour interval is  $5\text{ms}^{-1}$  and the first interval is  $25\text{ms}^{-1}$ . The two maxima of the westerly winds at around  $30^\circ\text{N}$  and  $30^\circ\text{S}$  indicate the position of the subtropical jet streams. For the bottom panel: the ascending wind is indicated by the continuous contours and the zero line is the short dashed contour. This figure shows the structure of the meridional circulation cells, where the maximum descending winds, around  $30^\circ$  latitude, indicate where the Hadley cell meets the Ferrel cell and the secondary maximum upward motions, around  $60^\circ$ , indicate where the Ferrel cell meets the polar cell.

the position of the climatological ridges and troughs. At intermediate scales slowly propagating Rossby waves cause slow meanders in the jet stream that steer the path of the weather systems that are transported

eastward by the jet stream.

A mathematical treatment of a Rossby wave is most straight forward in a barotropic atmosphere. In this approximation the atmosphere is described by a single layer of fluid with no temperature advection as isotherms and isobars are aligned. In a barotropic atmosphere the absolute vorticity of an air parcel is conserved:

$$\frac{d\eta}{dt} = \frac{d(\zeta + f)}{dt} = 0 \quad (1.1)$$

$\frac{d}{dt}$  is the material derivative following the motion,  $\zeta$  is the relative vorticity

$$\zeta = \frac{\partial V}{\partial x} - \frac{\partial U}{\partial y} \quad (1.2)$$

and  $f$  is the Coriolis parameter:

$$f = 2\Omega \sin \varphi \quad (1.3)$$

with  $U$  and  $V$  the zonal and the meridional wind components respectively. This equation is known as the barotropic vorticity equation. This conservation is the driving principle behind the Rossby wave propagation mechanism with the change of the Coriolis parameter with latitude acting as the restoring force for meridional displacements of air parcels, called the  $\beta$ -effect:

$$\beta = \frac{\partial f}{\partial y} = 2\Omega \cos \varphi. \quad (1.4)$$

To further analyse the characteristics and behaviour of Rossby waves we derive the dispersion relation of waves in a westerly flow  $\bar{U}$  (see Hoskins and Karoly (1981) and Hoskins and Ambrizzi (1993)). We assume a wave-like solution for the equation of motion (Eq. 1.1) of the form  $\exp[i(kx + ly - \omega t)]$ , where  $k$  is the zonal wave number,  $l$  the meridional wave number and  $\omega$  is the frequency for deviations from the westerly flow  $\bar{U}$ . The dispersion relation for the barotropic Rossby wave is:

$$\omega = \bar{U}k - \frac{\beta^*k}{K^2} \quad (1.5)$$

where  $\beta^*$  is the meridional gradient of absolute vorticity

$$\beta^* = \beta - \frac{\partial^2 \bar{U}}{\partial y^2} \quad (1.6)$$

and  $K$  the total wave number  $K = \sqrt{k^2 + l^2}$ . This equation shows that the propagation of Rossby waves depends on the meridional profile of the jet ( $\bar{U}(y)$ ). Shorter waves tend to move eastwards and longer waves westwards. For a given latitude the stronger the wind, the smaller the critical wavenumber for which the wave is stationary. For stationary waves  $\omega$  is zero and the critical total stationary wavenumber becomes:

$$K = K_s = \sqrt{\frac{\beta^*}{\bar{U}}} \quad (1.7)$$

Fig. 1.2 presents an example of the structure of Rossby waves on different temporal and spatial scales using the geopotential height field at the 500hPa level. In the top panel the daily field is shown: synoptic scale waves of about wavenumber 7 dominate. These tend to move fast eastwards, tend to break and mix heat, moisture and momentum. In the bottom panel the 10 day average field of the same date is shown: larger waves of wavenumber 4-5 are visible that move slower or can even be stationary. Within this time frame of 10 days and longer there is adequate time for the larger waves to be excited and propagate around the Hemisphere and therefore these longer waves have a larger and more persisting impact on the global scale. For this reason the larger and lower frequency Rossby waves are those that lead to teleconnection patterns (read more on teleconnections in section 1.3.1).

If we now consider a flow that is slowly varying with latitude, the propagation of the energy of barotropic Rossby waves can be traced by following rays along which the zonal wave number  $k$  and the angular frequency  $\omega$  are constant. The speed of the energy propagation is equal to the group velocity.

The Rossby ray paths are refracted in a way similar to the Snell's law for optics. For stationary Rossby waves  $\omega = 0$ , the rays are refracted stronger towards latitudes with larger stationary wavenumber  $K_s$ . When moving with the group velocity  $c_g$ , the bending of the ray can be approximated as:

$$\frac{d\alpha}{dt} = \frac{k}{K_s^2} c_g \frac{dK_s}{dy} \quad (1.8)$$

where  $\alpha$  is the angle that the direction of  $K_s$  makes with the  $x$  axis (zonal direction):

$$\tan \alpha = \frac{l}{k}. \quad (1.9)$$

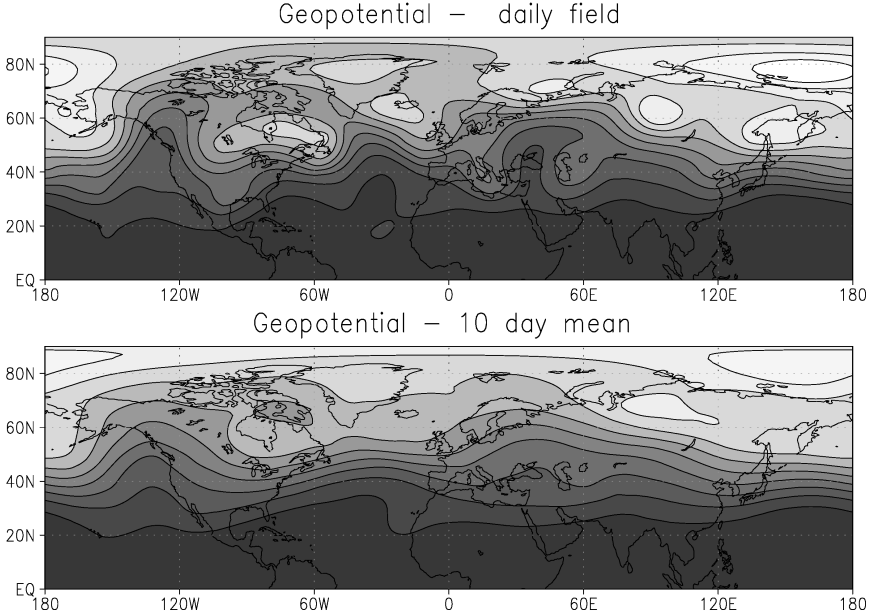


**Figure 1.2:** An illustration of Rossby waves as an example of the structural differences between the higher and the slower frequency circulation structures. Plotted is the geopotential height at the level of 500hPa on the 2<sup>nd</sup> of December 2012 from the ERA-Interim data set. The top panel contains the daily field and the bottom the 10 day averaged field around the same day. The contour intervals are 100 m and the highest contour in the subtropics is 5700 m.

We will use this property to illustrate the role of the jet stream in guiding Rossby wave energy.

### 1.2.3 The effect of the jet stream on Rossby wave propagation

The jet stream is a fast westerly current flowing around the globe in the upper troposphere with a sharp meridional profile, that is a consequence of the Earth's rotation and its differential heating (section 1.2.1). Due to its sharp profile  $\beta^*$  tends to have a larger relative maximum than  $\bar{U}$  (see Eq. 1.6). Therefore  $K_s$  (Eq. 1.7) takes its maximum values along the jet core and reduces quickly toward the flanks of the jet. This curvature and the attribute of the rays to bend towards larger  $K$ -values allows the

jet stream to trap Rossby waves and act as an efficient Rossby waveguide (see Eq. 1.8).

Each Hemisphere has subtropical and subpolar jets. Depending on the season their characteristics change following the temperature differences between poles and tropics. In the winter Hemisphere the meridional temperature gradient is enhanced and hence the jet stream is stronger.

The Northern Hemisphere jets are the subpolar Atlantic jet and the subtropical African-Asian jet. In the Southern Hemisphere the Australian subtropical jet and the polar jet are formed. The strongest waveguide is formed by the Asian jet in the boreal winter. This jet can support a circumglobal stationary wave pattern with a zonal wavenumber 5, referred to as the circumglobal waveguide pattern (Branstator (2002)). Secondary waveguides, but still important, are the Atlantic jet, usually supporting a stationary wavenumber of around 5 and the Southern Hemisphere jet with a  $K_s$  of about 7 (Hoskins and Ambrizzi (1993)).

The high mountain ridges in the Northern Hemisphere, such as the Rockies and the Himalayas cause stationary planetary waves and disrupt the zonal symmetry. Absence of mountain ridges make the Southern Hemisphere jets more zonally oriented and continuous. A detailed analysis of the winter and summer jet streams in both Hemispheres will follow in chapter 2.

#### 1.2.4 Excitation of Rossby waves by the Rossby wave source

So far we have discussed how the jet streams act as waveguides for the propagation of the Rossby waves that can change the weather patterns locally and remotely. Now we discuss how Rossby waves can be excited initially. A local vorticity anomaly will propagate as a Rossby wave. Local vorticity anomalies can be induced mechanically by a mountain ridge by vortex stretching or compression, or diabatically by heating that creates upper level convergence or divergence, or through baroclinic instabilities, whereby an initial vorticity disturbance grows through the convergence of background potential energy into kinetic energy. When strong surface convergence (divergence) is imposed mechanically or diabatically the air lifts (descends) and due to the mass conservation leads to upper level divergence (convergence). This vorticity change is a source of Rossby wave energy. Sardeshmukh et al (1987) derived an equation for such a Rossby wave source:

$$S = -(\zeta + f)D - v_\chi \nabla(\zeta + f) \quad (1.10)$$



where  $\zeta$  is the relative vorticity,  $f$  the Coriolis parameter,  $D$  the divergence and  $v_\chi = -\nabla\chi$ , where  $\chi$  is the velocity potential. The first term refers to the vortex stretching and the second to the advection of the vorticity by the divergent wind. A reasonable approximation of a diabatic Rossby wave source is usually reduced to:

$$S = -fD \quad (1.11)$$

Such a vorticity source in upper troposphere is most likely to occur in the tropics and the subtropics where surface heating by the sun is strongest and deep convection systematically takes place along the ITCZ. The upper tropospheric vorticity anomaly propagates away from the tropics, moving polewards and eastwards as a Rossby wave.

## 1.3 Extratropical teleconnections due to Rossby waves

### 1.3.1 General description of teleconnections

Heating inhomogeneities in the atmosphere are responsible for local or extended pressure and circulation anomalies. Since the atmosphere is highly interactive and vigorous, it will respond fast to an induced anomaly. The response can influence even the most remote regions and change the weather patterns. Some of those vast spanning patterns are recurring and persisting. This linkage of large scale weather patterns is called “teleconnection” or else preferred mode of low-frequency variability (Wallace and Gutzler (1981), Barnston and Livezey (1987), Kushnir and Wallace (1989), Trenberth et al (1998)). The term was first used by the British meteorologist Sir Gilbert Walker in the late 19th century, where he found a correlation between time series of atmospheric pressure, temperature and precipitation and moved the understanding of atmospheric variability one step forward.

Wallace and Gutzler (1981) used the technique of one point correlation maps to systematically track and study global teleconnections. They used sea level pressure or 500hPa height maps to correlate a variable at one point of the globe with the same variable at every other point. Such maps of correlations show preferred ridges or troughs locations, known as areas of preferred nodes or antinodes. As an example of a one point correlation map we show their figure 12b (here Fig. 1.3). The chosen point is in the North Atlantic (55°N, 20°W) and shows the teleconnectivity of the

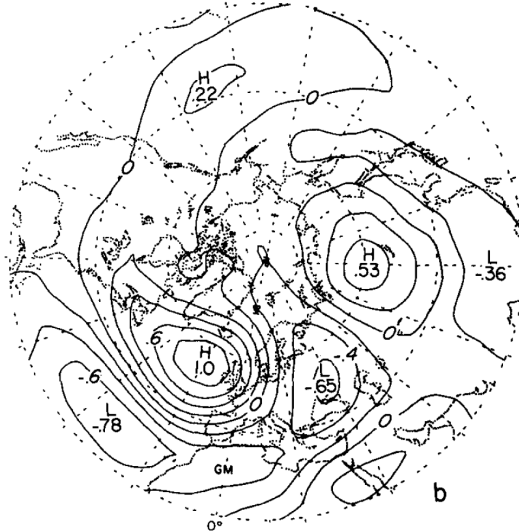


**Figure 1.3:** One point correlation map by Wallace and Gutzler (1981). The figure shows the correlation coefficient between 500hPa height at base grid point 55°N, 20°W and 500hPa height at every other point. Based on 45 winter months for the winters of 1972-63 to 1976-77.

region, where the positive correlation areas indicate the preferred nodes and the negative the antinodes.

The lifetime of a teleconnection pattern can be from a few days or weeks up to years or even decades. Extratropical teleconnections can be understood from diagnostics of Rossby waves. The teleconnection patterns tend to be most robust during winter, when the mean circulation is strongest, especially in the Northern Hemisphere. The teleconnections can influence the weather conditions, such as temperature, rainfall, wind, storm tracks and the jet stream. They have a large impact in nature, on humans and on society. They are often associated with floods, droughts, heat waves and cold spells. They can be responsible for changes in the water supply and fisheries, energy demand and supply and can modify air quality, fire risk and influence human health.

Fig. 1.4 contains a geographical map of the most important tropical and extratropical teleconnection patterns. Among the extratropical teleconnections, in this thesis we focus on the North Atlantic Oscillation (NAO).

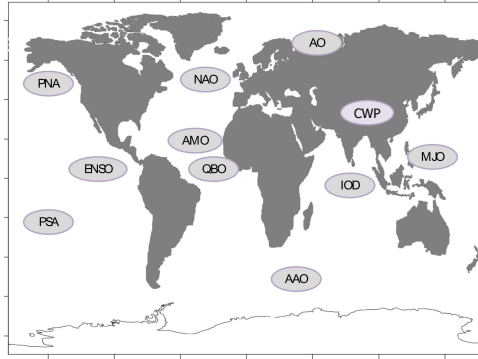


**Figure 1.4:** Names and location of some of the most important teleconnections. PNA: Pacific North American Pattern. NAO: North Atlantic Oscillation. AO: Arctic Oscillation. CWP: Circumglobal Waveguide Pattern. ENSO: El Niño-Southern Oscillation. AMO: Atlantic Multidecadal Oscillation. QBO: Quasi-Biennial Oscillation. IOD: Indian Ocean Dipole. MJO: Madden-Julian Oscillation. PSA: Pacific-South American teleconnection. AAO: Antarctic Oscillation.

### 1.3.2 The North Atlantic Oscillation

Among the most prominent extratropical teleconnection patterns we find the NAO. It is the major source of atmospheric variability over the North-east Atlantic, Europe and North America (Barnston and Livezey, 1987). Understanding the processes that govern its variability is highly valuable in the context of weather prediction and climate change. The NAO is a large-scale atmospheric seesaw between the subtropical Azores High and the subpolar Iceland Low. This north-south sea level pressure dipole is associated with changes in the the westerlies across North Atlantic into Europe and a displacement of the storm tracks and of the jet stream that is reflected in changes in the large-scale zonal and meridional heat and moisture transports. The displacement and modification of the jet stream changes the waveguiding properties and hence influence the formation and propagation characteristics of Rossby waves. The pattern is most vigorous in the boreal winter when the circulation is strongest. The effect of NAO variability on the local weather conditions are distinct over Eastern North America, North Atlantic and Northern Europe and often across Southern Europe and the Middle East.

Contrary to the extratropical mean flow, the NAO has a pronounced

barotropic structure (Thompson et al (2003)), with the amplitude of anomalies increasing with the height, in proportion to the strength of the mean zonal wind.

There is no unique way to define the NAO index. One approach is the difference of normalized sea level pressure (SLP) between Lisbon, Portugal and Stykkisholmur/Reykjavik, Iceland (Hurrell (1995)). Another index is extracted by a Rotated Principal Component Analysis (RPCA) applied to 500hPa height anomalies in the region  $20^{\circ}N - 90^{\circ}N$  (Barnston and Livezey (1987)). In this thesis, the NAO index is obtained by the first empirical orthogonal function (EOF) of the stream function at the level of 850hPa from  $90^{\circ}W$  to  $30^{\circ}E$  over the Northern Hemisphere (Branstator (2002)).

The NAO index is positive when the pressure difference between the subtropical high and the subpolar low is larger than usual. A positive NAO results in stronger westerlies and a northward shift of the North Atlantic jet, followed by a similar shift and intensification of the storm tracks. During this phase the winters in Northern Europe, Scandinavia and Eastern United States are milder and wetter, while in Greenland, Southern Europe, Northern Canada and Middle East winters are colder and drier.

The pattern is practically opposite during the negative NAO phase. Then the north-south pressure gradient is weaker, the Atlantic jet stream is more zonally oriented and displaced to the south and the winter storms are fewer and weaker. The southern position of the jet results in an outflow of cold air towards Northern Europe, and warm moist air into the Mediterranean. The Eastern United States experience heavier winters, while the conditions in Canada are milder. The negative phase is often associated with atmospheric blocking patterns in the jet stream, that are responsible for unusual prolonged weather conditions. In Fig. 1.5 the north-south dipole pattern of a selection of negative NAO events is illustrated, together with the accompanying temperature anomalies over the Northern Hemisphere.

The NAO is mostly governed by internal atmospheric dynamics arising primarily from interactions between breaking synoptic Rossby waves and the mean jet stream (Hurrell et al (2003)). Both tropical and extratropical processes contribute to the formation of the NAO pattern, but the latter play a leading role. For example, the fundamental timescale for NAO fluctuations of about 10 days is attributed to the interactions between the mean flow and the extratropical transient eddies (Feldstein (2000)).

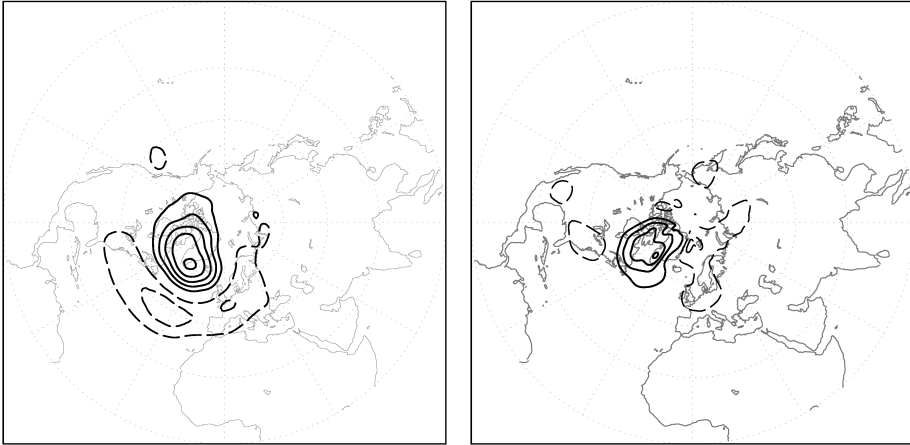


**Figure 1.5:** A representation of the NAO dipole as a composite of geopotential height anomalies at 500hPa at the left panel and as a composite of surface temperature anomalies at the right panel for a selection of negative NAO events. The events are selected from the period 1979-2010 for December-January-February months of ERA-Interim reanalysis data where the NAO index is obtained by the first EOF of the stream function at the level of 850hPa from  $90^{\circ}\text{W}$  to  $30^{\circ}\text{E}$  over the Northern Hemisphere. Further explanation on the dataset and the selection of the events follows in chapter 3. The contour interval for the geopotential height is 35m. The contour interval for the temperature anomalies is  $2^{\circ}\text{C}$ . In both plots the negative values are indicated with dashed contours.

Changes in the rate and location of tropical heating due to deep convection play a secondary role in forcing NAO variations. Anomalies in tropical SSTs modify the tropical convection, the Rossby wave source, which in turn impacts the extratropical circulation and possibly the NAO.

The NAO interacts with the North Atlantic ocean as well. The air-sea coupling in determining the overall variability of the NAO is of interest, especially for understanding the details of the amplitude of the NAO and its long-term temporal evolution, as well as its predictability (Czaja et al (2003)). On seasonal time scales the ocean responds to changes associated with the NAO, such as alternations in the surface stress, ocean-atmosphere heat fluxes and fresh water fluxes (Cayan (1992a), Cayan (1992b)). On longer time scales it is found that the NAO has some impact on the Atlantic thermohaline circulation and hence on the poleward heat transport and distribution of the SSTs (Dickson et al (1996)). The interaction with

the ocean is of interest but not subject of study in this thesis.

## **1.4 Tropical teleconnections connected to Indian Ocean variability**

The tropical teleconnections, apart from the propagation of Rossby waves, involve excitation and propagation of atmospheric and oceanic Kelvin waves and strong atmosphere-ocean interactions. Within the tropical band, the tropical Indian Ocean (IO) is important as it exhibits notable atmospheric variability influencing the climate not only on regional, but also on a global scale through teleconnection patterns. Its impact on the surrounding countries on the food supplies, the water resources and the general welfare is crucial. The bounding of the basin to the north by the Asian continent drives the strongest monsoon on Earth and is responsible for the creation of one of the strongest deep convection centers globally. The precipitation variability of East and South Africa as well as of Australia is often modulated by changes in the IO SSTs (Cook (2000), Latif et al (1999), Gupta et al (2010), Cai et al (2011)). Recent studies suggest that the tropical IO plays a key role on the evolution of important teleconnection patterns, such as the NAO (Hoerling et al (2004)) or the El Niño-Southern Oscillation (ENSO) (Yu et al (2002), Annamalai et al (2005b)).

The main governors of the IO variability are the Indian monsoon system, the Indian Ocean Dipole (IOD) and ENSO (El Niño-Southern-Oscillation). These phenomena will be further discussed below. Other sources of variability are the ocean circulation, local air-sea interaction, the Madden-Julian Oscillation (Madden and Julian (1994), Zhang (2005)), fresh water fluxes from the Indonesian Throughflow, river runoff and heavy oceanic precipitation (Saji et al (2005)).

### **1.4.1 The Indian Monsoon**

The major driver of IO variability is the seasonal monsoon winds (Yamagata et al (2004)). The monsoon is predominantly created by the different heat capacities of the ocean and the Asian continent, that results in a warmer Asian continent during summer, compared to the North IO, and a warmer North IO during winter. The warmer continent during summer creates a large low surface pressure anomaly over Asia and acceler-

ates large moisture-laden southwesterly air masses towards the continent. When they reach the continental slopes they are forced to ascend, drop in temperature, saturate and bring heavy precipitation over the Arabian Sea, the Indian continent and Southeast Asia. Along the Western IO, the south-west monsoon winds induce Ekman upwelling of fresh, cold water and a raise of the thermocline depth that cools the SSTs. The change in the SSTs in turn modify the pressure systems and the convection. During winter the system reverses and the winds become north-east and the dry monsoon season develops. The north-east winds hamper the upwelling over Western IO and the SSTs become warmer. The equatorial westerlies force the oceanic equatorial currents that transport the heat into the Eastern IO basin.

The strong influence of the monsoon system on the reversing winds extends southwards until  $10^{\circ}\text{S}$ . Unlike the other tropical oceans, the IO near-Equator winds have a weak westerly annual mean. Easterlies blow only during late winter and early spring, in the late winter monsoon season. South of  $10^{\circ}\text{S}$  the winds are southeasterly and are relatively steady throughout the year (Schott et al (2009)).

Forecasting the distribution, strength and timing of the Indian monsoon has proven a challenging task, as the monsoon is generated by complex interactions between sea and land and is influenced by both the Indian and the Pacific oceans. Global warming only adds up to this uncertainty. Despite this complexity, these days important steps have been made towards better short and longer range prediction of the monsoon, due to improved model and data assimilation techniques (Wang et al (2005), Wu et al (2009)).

### 1.4.2 The Indian Ocean Dipole

Another important source of IO variability is the atmosphere-ocean coupled phenomenon widely known as the Indian Ocean Dipole (IOD) (Saji et al (1999)). On a regional scale the IOD has a significant impact on the atmospheric circulation and precipitation anomalies and on a larger scale the phenomenon correlates with temperature and precipitation anomalies in remote regions, such as Europe, America, South Africa and Northeast Asia (Saji and Yamagata (2003a)). The IOD is characterized by an east-west SST gradient along the central tropical IO that strongly impacts the atmospheric convection over the basin. When the Central-West IO is warmer than the Eastern IO the event is called a positive event and vice-

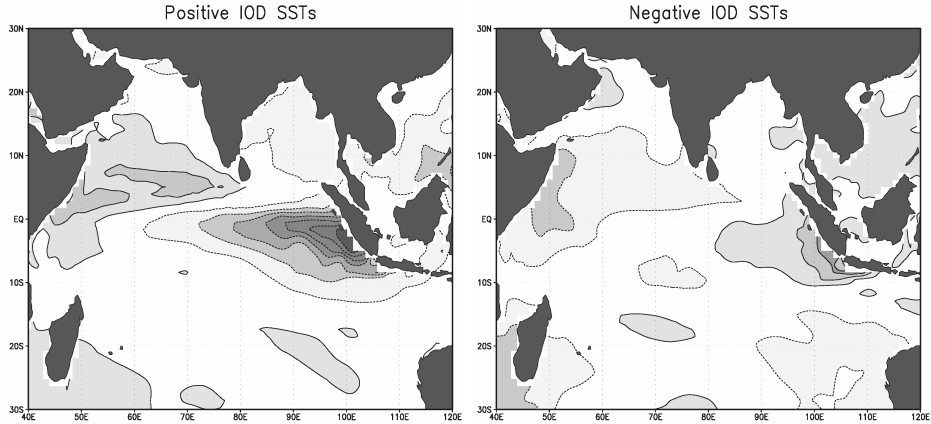


**Figure 1.6:** Representative positive and negative IOD conditions in the SST anomalies over Indian Ocean during October. The data are taken from the 40 years control run of the model EC-Earth with constant year 2000 forcing conditions (more details about the model will follow in chapters 4 and 5). The left panel corresponds to the October with the most positive IOD Index and the right panel the October month with the most negative IOD Index. Solid lines indicate positive SST anomalies and dashed negative anomalies in  $^{\circ}\text{C}$ . The contour interval is  $0.5^{\circ}\text{C}$ .

versa for the negative event. The events usually develop during June, peak in October and decay in November. During the positive phase the warm pool is shifted to the west, causing heavy precipitation over Eastern Africa and droughts over Indonesia and Australia. The wind response to the colder SSTs in the East IO enhance the upwelling in the region, which raises the thermocline and enhances the cooling of SSTs. The warmer SSTs in the West IO on the contrary lead to reduced upwelling, a deepening of the thermocline and further enhance the warming of the SSTs. The changes in the thermocline depth initiate the excitation of westward traveling oceanic Rossby waves south of  $10^{\circ}\text{S}$  and eastward traveling oceanic Kelvin waves along the equator. The waves raise or deepen the thermocline, followed by changes in oceanic mixing and atmospheric circulation affecting the evolution of the event. During the negative phase the atmospheric and oceanic responses are approximately the opposite.

The structure of the SST anomalies over the IO basin during the positive and the negative IOD events is shown in figure 1.6.



### 1.4.3 The Seychelles Dome

The Seychelles Dome (SD) is the thermocline ridge just south of the equator in the Western Indian Ocean basin, between  $5^{\circ}S - 10^{\circ}S$  and  $50^{\circ}E - 80^{\circ}E$ . It is characterized by strong atmospheric convection and a shallow thermocline and is associated with large intraseasonal convection and SST variability (Harrison and Vecchi, (2001)). The large variability and strong coupling of the SD with the atmosphere suggests that it can play an important role in the formation of teleconnection patterns, provided that the conditions are favorable. The SD is influenced by surface and subsurface processes, such as air-sea fluxes, Ekman upwelling in response to wind stress curl, ocean dynamics (vertical mixing) and oceanic Rossby waves propagating from the southeastern Indian Ocean into the region. The favouring season for a strong SD is the boreal winter, when the thermocline is most shallow and variable and the coupling between ocean and atmosphere is strong.

It has been found that the subseasonal and interannual variability of the SD is influenced by large scale events, such as the IOD, ENSO and the Madden-Julian Oscillation (MJO) (Tozuka et al (2010), Lloyd and Vecchi (2010)). The SD is enhanced by cooling events in the Western Indian Ocean and westerly winds that raise the thermocline and increase the upwelling. This can be associated with a strong Walker circulation, such as the conditions in a negative IOD or La Niña-like conditions.

### 1.4.4 ENSO

The major mode of natural atmosphere-ocean variability on the globe is ENSO. This is the combination of the El Niño (or La Niña if the phase is opposite), which is the recurrent warming and cooling of the equatorial Pacific ocean and the Southern Oscillation (SO), which is the see-saw in atmospheric pressure between the eastern and Western tropical Pacific. The phenomenon is phase locked to the annual cycle and peaks during the boreal winter.

Along the equator the strong east to southeasterly trade winds allow the cold deep currents, that flow from Antarctica to the west coast of South America, to upwell and keep the SSTs relatively cool along the equatorial cold tongue. In the Western Pacific the trade winds deepen the thermocline and the surface water is warmer. This area of warm ocean waters, the Pacific warm pool, is a major source for atmospheric convection

and is associated with deep convective systems and strong rainfall. During an El Niño year the trade winds weaken, the upwelling is reduced and the central and Eastern tropical Pacific warm up. The change in ocean temperature drives a shift in atmospheric convection and accompanying precipitation from the Western to the Central tropical Pacific Ocean causing severe droughts over Australia, Indonesia and parts of Southern Asia, while floods occur over Peru and Southern United States. Due to propagating Rossby waves excited by the changes in the upper tropospheric divergence due to the shifts in convection, teleconnections are created that form an arch of alternating high and low pressure anomalies extending into the North American continent impacting the seasonal temperatures and precipitation in those areas. A similar mechanism exists in the Southern Hemisphere with teleconnections that influence the climate conditions in South America.

A La Niña year is characterized by almost the reversed anomalies with the opposite consequences. An example of SST anomalies during an El Niño and during a La Niña from climate model simulation data of the climate model EC-Earth is shown in Fig. 1.7.

The Indian ocean basin is strongly affected by ENSO. An El Niño event causes a gradual warming of the IO that peaks about one season after the maximum phase of El Niño (Nigam and Shen (1993), Liu and Alexander (2007), Schott et al (2009)). During an El Niño the convection over the IO is suppressed, allowing more solar radiation to reach the surface and warm the ocean. Most of the ENSO-induced warming is explained by wind induced surface heat fluxes. An exception to that is the Southwestern IO region, where the ocean dynamics play a major role (Klein et al (1999)). In the Western IO between  $5 - 10^{\circ}\text{S}$  we find a thermocline ridge and the surface water is cooler. During an El Niño anomalous anticyclonic wind stress curl is created over the tropical Southeastern IO that excites a downwelling oceanic Rossby wave. The wave travels to the west and several months later reaches the thermocline ridge. There it deepens the thermocline and further warms the surface water (Xie et al (2002a)).

Some studies suggest that the ENSO and the IOD evolve independently (Saji and Yamagata (2003a), Behera et al (2006)), while others suggest that they are often linked (Nagura and Konda (2007), Fischer et al (2005)). The linkage can take place through atmosphere, by an extension of the Walker circulation to the west, and through the ocean by the Indonesian Troughflow and transport of warm water from the Pacific to the Indian ocean. Therefore El Niño is often associated with a positive

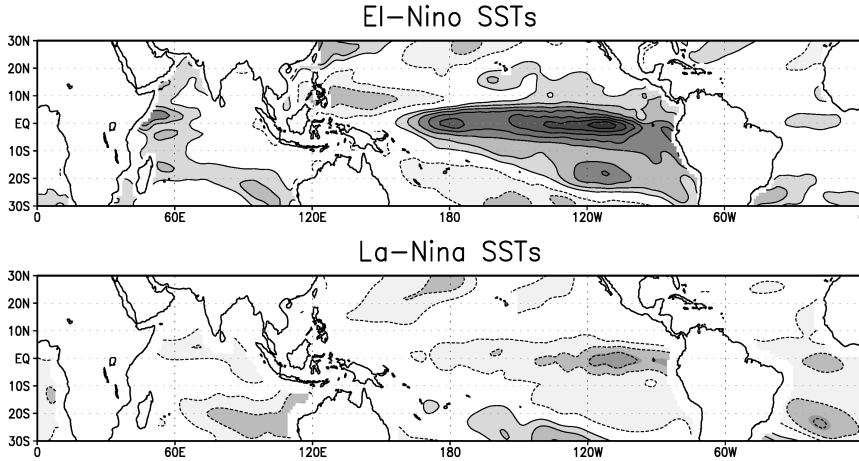


**Figure 1.7:** Representative El Niño and La Niña SST anomalies over the tropical regions during December. The data are taken from a 40 year control run of EC-Earth as in Fig. 1.6. The top panel corresponds to the December month with the most positive Nino3.4 Index and the bottom panel the December with the most negative Nino3.4 Index. The Nino3.4 index is the averaged SST anomaly over  $170^{\circ}W - 120^{\circ}W$  and  $5^{\circ}S - 5^{\circ}N$ . The solid lines indicate positive SST anomalies and the dashed negative anomalies in  $^{\circ}C$ . The contour interval is  $0.5^{\circ}C$ .

IOD and La Niña with a negative IOD. When these events co-occur the weather phenomena can reach their most extreme phases (mostly over Australia), while when they are opposite they are mitigated.

## 1.5 An overview of this thesis

Following the above general introduction on the relevant concepts and phenomena that are important for this thesis, we conclude with the research questions that will be addressed in the various chapters.

The main subject of this thesis is the study of the tropical and extratropical atmospheric response to tropical forcing through the propagation of atmospheric waves and ocean-atmosphere interactions, with a focus on Indian Ocean variations.

The study sets off with more theoretically oriented investigations about Rossby wave propagation using a relatively simple equation for large-scale atmospheric motions applied to idealised atmospheric flow configurations and subsequently to more realistic flows. It ends with a state-of-the-art modelling experiment to study the complex network of interactions in a realistic simulation of the climate variations in the Indian Ocean.

It is known that the jet streams act as waveguides to trap Rossby wave energy, a mechanism that is important for the formation of hemispheric wide teleconnections. We call the ability of jets streams to trap Rossby wave energy “waveguidability”. Theoretical concepts have been published, diagnostic studies have been conducted, but a systematic study on the waveguidability of jet streams is lacking. In this thesis we systematically investigate through a series of idealised modelling experiments the waveguidability of a jet stream on its key characteristics: strength, width and latitudinal position. This will be studied using a barotropic model in **chapter 2**.

The dominant teleconnection pattern NAO influencing the weather and climate in Europe, is primarily forced by processes in the extratropics. It is known however, that also tropical disturbances can affect the NAO. A quantitative study about the contribution of the tropical forcings on the NAO variations is lacking. The same barotropic model used in chapter 2 will be applied to observed atmospheric flow conditions in **chapter 3** in order to evaluate the contribution of tropical versus extratropical forcings to observed NAO events.

One of the tropical regions that is known to impact extratropical variability, including NAO variations, is the Indian Ocean region. A region of special interest is the Seychelles Dome region, as it is a region of potential strong atmosphere-ocean interactions. A lot of diagnostic studies have appeared in relation to SD variations and its covariation with other climate phenomena, but a detailed modelling study of the impact of SD

---

variations on the evolution of the coupled atmosphere-ocean system has not been done. In order to do so, the complex web of interactions involved needs to be adequately described, such as variations in the ocean thermocline depth, its effect on the SST, the exchange of heat and moisture between ocean and atmosphere, atmospheric convection, radiation, circulation, waves to name a few. In **chapter 4** we will conduct a control simulation with the state-of-the-art climate model EC-Earth and evaluate the ability of EC-Earth to reproduce the climatology and variations of the atmosphere and ocean evolution in the Indian Ocean basin. Having verified the ability of EC-Earth to give a reasonable description of the IO climate, we will conduct an ensemble experiment in **chapter 5** to specifically study the effect of a shallow SD event on the tropical atmosphere and beyond.

Finally, this thesis is concluded in **chapter 6** with a summary and a discussion of the main results.



---

## CHAPTER 2

---

### “Waveguidability” of idealized jets

Iris Manola, Frank Selten, Hylke de Vries, Wilco Hazeleger  
*Journal of Geophysical Research: Atmospheres* **118**, no.18: 10-432,  
(2013)

**Abstract** It is known that strong zonal jets can act as waveguides for Rossby waves. In this chapter we use the ECMWF reanalysis data to analyse the connection between jets and zonal waves at timescales beyond ten days. Moreover, a barotropic model is used to systematically study the ability of idealised jets to trap Rossby wave energy (“waveguidability”) as a function of jet strength, jet width and jet location. In general, strongest waveguidability is found for narrow, fast jets. In addition, when the stationary wave number is integer, a resonant response is found through constructive interference. In Austral summer the Southern Hemispheric jet is closest to the idealised jets considered and it is for this season that similar jet-zonal wave relationships are identified in the ECMWF reanalysis data.

## 2.1 Introduction

It has been long known that strong zonal jets can act as waveguides for Rossby waves (Hoskins and Karoly 1981, Branstator 1983, Hoskins and Ambrizzi 1993). Circumglobal quasi-stationary zonal waves with wavenumber between 3-6 are often observed along Northern and Southern Hemisphere jet streams and have an equivalent barotropic structure (Salby 1982, Branstator 2002). The existence of these zonal Rossby waves leads to co-variability of atmospheric variations between remote locations and they play a role in the response of the atmosphere to tropical sea-surface temperature variations (Haarsma and Hazeleger 2007, Trenberth et al 1998) and increasing levels of greenhouse gases (Selten et al 2004, Brandefelt and Körnich 2008, Branstator and Selten 2009). Recent studies focusing on the Northern Hemisphere summer season highlight the connection between such recurrent zonal wave anomalies along the jet and large regional temperature and precipitation anomalies, including the U.S. 1988 drought (during June) and the 1993 US Midwest flooding (during July) (Lau and Weng 2002, Wang et al 2010, Ding et al 2011, Schubert et al 2011).

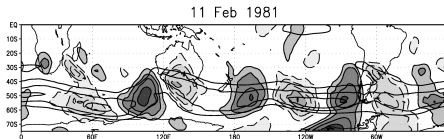


**Figure 2.1:** An example of a strong zonal wave anomaly in the Southern Hemisphere Jet. The date is the 11<sup>th</sup> of Feb 1981. It is a 10-day running mean state from the ERA-Interim dataset. The meridional wind anomalies are shaded with intervals of  $4 \text{ ms}^{-1}$ . The negative values are indicated with dashed lines. The total wind speed exceeding  $20 \text{ ms}^{-1}$  is plotted in contours. The interval is  $10 \text{ ms}^{-1}$ .

An example of a zonal wave anomaly along the jet is plotted in Fig. 2.1. Following Branstator (2002) we use the meridional wind anomaly  $v'$  at 300 hPa as an indicator of the zonal wave anomaly and the jet is characterized by the total wind speed  $u_{tot}$ . In this case, the zonal wavenumber of this 10-day mean anomaly field is 4 and the maximum amplitude is co-aligned with the jet axis circumglobally. An Empirical Orthogonal Function (EOF) analysis of the meridional wind variations of 10-day averaged fields in the Southern Hemisphere summer (see Fig. 2.2) shows that this



zonal wave is the dominant mode of variability of the meridional wind. More specifically, the first two principal modes have zonal wavenumber 4 with phases that are in quadrature. Together they describe wavenumber 4 anomalies of arbitrary phase and account for 25% of the variance of 10-day mean anomalies. The third and fourth EOF modes also form a pair, now with zonal wavenumber 5 and describe 12.8% of the variance. A cross-correlation analysis of the amplitude time series of these two pairs of EOFs (not shown) indicates that both waves weakly propagate eastwards with about  $2 \text{ ms}^{-1}$  for EOF 1-2 and  $4 \text{ ms}^{-1}$  for EOF 3-4. A correlation analysis between the amplitude time series of the dominant meridional wind anomaly EOF at 300hPa with the meridional wind anomaly at 300, 500, 650, 800 and 1000 hPa along latitude  $50^\circ\text{S}$  tells us that this circum-global wave has an equivalent barotropic structure (see Fig. 2.3). In a recent paper by (Zappa et al 2011) wavenumber 5 anomalies were studied in a baroclinic aquaplanet model. These waves had a baroclinic structure below 800hPa and were phase locked with a wavenumber 5 anomaly in tropical precipitation. Both attributes are not typical of the waves we study here. A barotropic theory thus seems adequate to describe the dynamics of these waves.

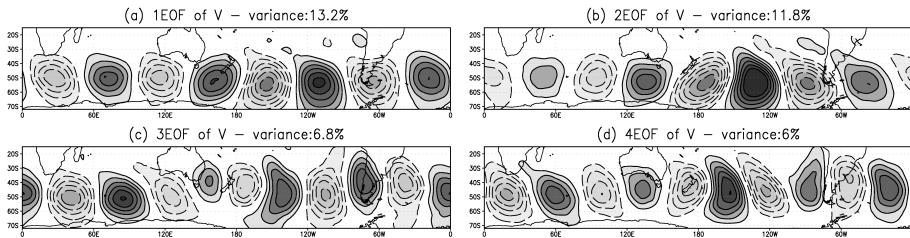


**Figure 2.2:** The first four Empirical Orthogonal Functions of the meridional wind anomalies between latitudes  $15^\circ - 70^\circ\text{S}$  for Southern Hemisphere Summers for the years 1979 – 2010 of 10-day running mean ERA-Interim reanalysis data at 300 hPa. In (a) the principal mode is plotted and it describes 13.2% of the total variance. The second mode (b) describes 11.8% of the variance, the third (c) 6.8% and the fourth (d) 6%. The contour interval is  $0.5 \text{ ms}^{-1}$  and negative values are dashed.

In this chapter we focus on how different aspects of the jet constrain specific features of the trapped, zonal waves such as their wavenumber and amplitudes. An approximate theory that is able to explain some of the features of the zonal waves, such as the wave number and the geo-

graphical position, is based on the barotropic vorticity equation linearized around idealised or observed time-mean flows at upper tropospheric levels (Hoskins et al 1977, Branstator 1983, Hoskins and Ambrizzi 1993). In this chapter we apply this approach to systematically study the ability of idealized jets to trap Rossby wave energy (“waveguidability”) as a function of 3 parameters: jet strength, jet width and jet location. To use realistic values of these parameters we begin with an analysis of the characteristics of the observed Northern and Southern Hemisphere jets. Using these characteristics we define a range of idealised jets and study their waveguidability. The observed zonal waves owe their existence to the presence of sources of Rossby wave energy, such as the interaction of the atmospheric flow with mountain ridges, barotropic and baroclinic flow instabilities and upper tropospheric divergent flow connected to tropical, deep convection. We assume that due to these sources there is ubiquitous Rossby wave energy present at any time and that the dispersion of these Rossby waves on the existing background flow is a major contributor to the formation of the observed zonal wave anomalies in the 10-day mean fields. At the end we check in the observations whether the waveguidability indeed constrains features of zonal wave anomalies in the jet region.

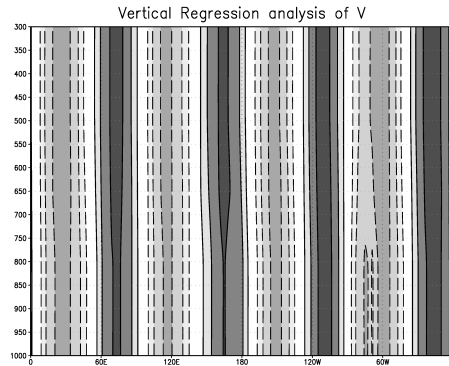


**Figure 2.3:** Correlation coefficient between the amplitude time series of the dominant meridional wind anomaly EOF at 300hPa with the meridional wind anomaly at 300, 500, 650, 800 and 1000 hPa along latitude  $50^{\circ}S$  in the period 1979 – 2010. The contour intervals are 0.2 and the maximum correlation is 0.65. Negative values are dashed.

The chapter is organised as follows. In section 2.2 we analyse the characteristics of observed jets in the Northern and Southern Hemisphere.

Next we introduce the barotropic model and the experimental design (section 2.3) that we follow in order to determine the waveguidability of idealised jets covering the range of observed jet characteristics in section 2.4. For specific jet configurations, a resonant waveguide response is found which is further analysed in section 2.5. In the final section (2.6) we return to the observations to check whether the “waveguidability” of the jet constrains the co-occurring zonal wave anomalies.

## 2.2 Characteristics of Observed Jets

The observational analysis is based on the ERA-Interim reanalysis dataset of the European Center for Medium-range Weather Forecast (ECMWF, Dee and Coauthors (2011)) from 1979 to present. We analyse 10-day running mean fields at the level of 300hPa in order to focus on the low-frequency variations of the jets and the zonal waves and to average out baroclinic disturbances. We will show in the barotropic model results that within 10 days Rossby wave energy is able to propagate all around the hemisphere and so a 10-day running mean filter is adequate to resolve the zonal waves of interest.

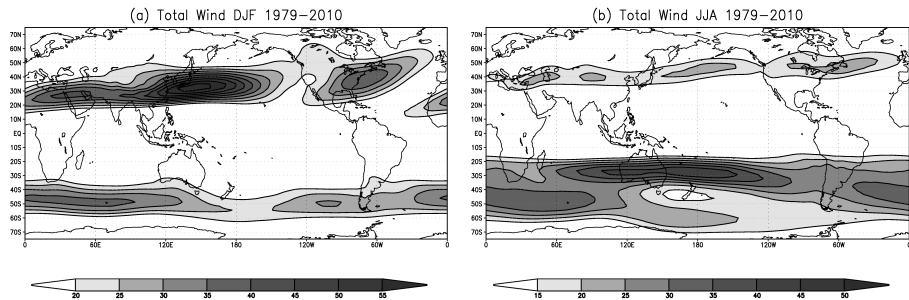


**Figure 2.4:** The major jet streams for both Hemispheres from the time-averaged 300 hPa total wind speed of ERA-Interim reanalysis for the years 1979 – 2010 at 300hPa, for (a) DJF and (b) JJA. The contour interval is  $5 \text{ ms}^{-1}$ .

As a first indication of observed jet characteristics we show the time-averaged total wind  $u_{tot}$  at 300 hPa for the DJF and JJA season in Fig. 2.4. The strongest mean jets are found in the winter hemispheres, with maxima of around  $60 \text{ ms}^{-1}$ . The jets in the winter hemispheres are split between subtropical and subpolar jets, for instance over the North-

Atlantic region. In the summer hemispheres the jets are weaker, with maxima of around  $40 \text{ ms}^{-1}$ , but more continuous.

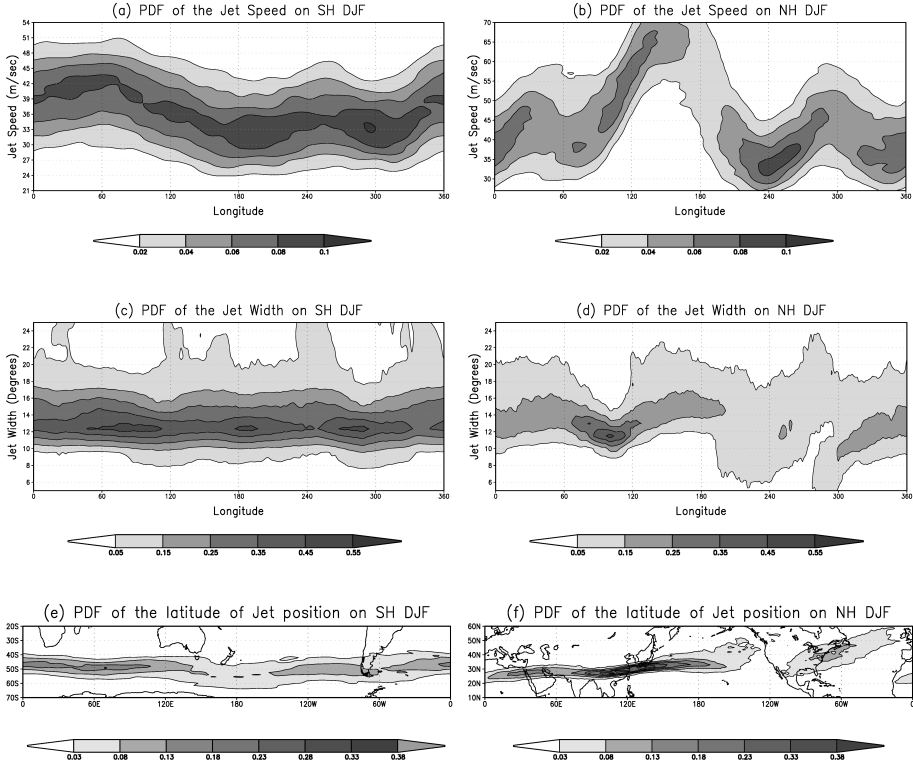


**Figure 2.5:** Probability density function of jet speed as a function of longitude for SH summer (a) and NH winter (b). The jet speed is defined as the maximum total wind at each longitude from the ERA-Interim reanalysis data for the years 1979 – 2010 at 300hPa. The PDF of the jet width as a function of longitude in SH summer (c) and NH winter (d). The jet width is defined as the distance between the inflection points of the meridional total wind profile. PDF of jet position in SH summer (e) and NH winter (f). The position is defined as the latitude of the maximum total wind. The values for the PDFs are the normalized probability.

To get an idea of the range of jet strengths, widths and positions that we should consider in the barotropic model experiments, we calculated the probability density function (PDF) of each characteristic as a function of longitude on the basis of 10-day running mean fields between 1979 and 2011, both for the Northern Hemisphere (NH) winter conditions and the

Southern Hemisphere (SH) summer. The SH summer conditions are closest to the zonally symmetric idealised jets that we will use as background flows in the barotropic model calculations. The three jet characteristics are defined as follows: the jet strength is given by the total wind speed at the jet maximum at each longitude. In case there are multiple maxima we take the one closest to the equator. The jet width is estimated as the region in which the meridional rate of change of the latitudinal gradient of the zonal flow is negative, or in other words, the meridional distance between the inflection points of the meridional jet profile (see Fig. 2.6 for a visual explanation of this definition of the jet width). Prior to the calculation of the second derivatives, the 10-day mean wind fields are smoothed with a Hanning window in order to reduce the scatter in the calculation of the inflection points due to small-scale variations in the wind fields. Finally, the jet position at each longitude is defined as the latitudinal position of the maximum total wind.

The PDF of the jet speed (Fig. 2.5a-b) shows a stronger dependence on longitude for the NH winter (b) than for the SH summer (a). In SH summer the fastest jets are found around  $60^{\circ}\text{E}$  and jet speeds typically vary between  $24 - 51\text{ms}^{-1}$ . In NH winter jet speeds are stronger and typically vary between  $30 - 70\text{ms}^{-1}$  with fastest jets over the Pacific region.

The PDF of the jet width as a function of longitude is plotted in Fig. 2.5c-d. In SH summer (c) the width varies roughly between  $10^{\circ}$  and  $20^{\circ}$  with the mode around  $12.5^{\circ}$ . There is little dependence on longitude. In contrast, in NH winter (d) a strong dependence of the PDF of the jet width on longitude is observed with smallest variations in the width at the beginning of the Pacific storm track. The PDF is weakly bimodal over the American-Atlantic sector with modes around  $8^{\circ}$  and  $16^{\circ}$ . This weak bi-modality could be due to small width values that belong to the subtropical jet and the larger widths values that belong to the eddy-driven jet at mid-latitudes.

Finally, the PDF of the jet position as a function of longitude is depicted in Fig. 2.5e-f. In the SH summer (e) the PDF is clearly uni-modal. The mode does depend somewhat on longitude with most southerly positions around the dateline. At these longitudes the jet position varies the most, roughly between  $40^{\circ}\text{S}$  to  $60^{\circ}\text{S}$  whereas at other longitudes around the zero meridian the positions are usually restricted between  $40^{\circ}\text{S} - 50^{\circ}\text{S}$ . In the NH winter (f) the PDF of the jet position is wider and is weakly bimodal over the Atlantic sector where the exit of the subpolar Atlantic

jet concurs in longitude with the entrance of the subtropical African-Asian jet. Positions range from  $20^{\circ}N - 60^{\circ}N$

Visual inspection of time series of 10-day mean anomalies of  $v$  plotted on top of the total wind as in for example Fig. 2.1 often reveals strong zonal waves co-aligned with zonal jets. The jet characteristics vary over wide enough ranges to expect that this could be reflected in the properties of observed variations of the zonal waves. To make this connection, we will use a barotropic model, introduced in the next section, to study the waveguidability of idealised jets.

## 2.3 Numerical Experiments

### 2.3.1 The barotropic model

The barotropic vorticity equation (BVE) basically describes conservation of absolute vorticity in the absence of forcing and dissipation:

$$\frac{d(\zeta + f)}{dt} = \frac{\partial \zeta}{\partial t} + \mathcal{J}(\Psi, \zeta + f) = -\nu\zeta - \mu\nabla^4\zeta + F \quad (2.1)$$

where  $\Psi$  is the streamfunction,  $\zeta$  the relative vorticity,  $f$  the Coriolis parameter,  $\mathcal{J}$  the Jacobi operator describing the advection of absolute vorticity,  $\nu$  the Ekman damping coefficient,  $\mu$  the strength of the hyperviscosity and  $F$  a time-independent, spatially varying forcing. The barotropic model solves this equation using a spectral method (Selten 1995). The stream function and vorticity fields are described by a sum of spherical harmonical functions with time-varying coefficients. The sum is triangularly truncated at total wavenumber 42 (T42). The streamfunction is related to the vorticity field by:

$$\Psi = \nabla^{-2}\zeta \quad (2.2)$$

so given an initial vorticity field eq. (2.1) can be integrated in time in order to obtain the evolution of the flow. We wish to calculate how Rossby wave energy propagates on a given background flow. Therefore we need to construct a stationary background flow. This is done as follows. Given a background flow  $\zeta_b$ , a forcing  $F$  is calculated that balances the dissipation and advection terms such that the tendency is zero:

$$F = \mathcal{J}(\Psi_b, \zeta_b + f) + \nu\zeta_b + \mu\nabla^4\zeta_b \quad (2.3)$$

Inserting the background streamfunction  $\Psi_b$  and vorticity field  $\zeta_b$  in this equation gives the desired forcing field  $F$  that keeps this background flow stationary provided that the dissipation is large enough. The values of the coefficients  $\nu$  and  $\mu$  are such that the e-folding timescale of the damping is 9 and 3 days respectively for the smallest waves. We verified that the sensitivity of the results to the exact values of these dissipation terms is low. In order to determine the Rossby wave energy propagation on a given background flow a Rossby wave source (RWS) is added to (2.1) as in Hoskins and Ambrizzi (1993). The RWS,  $F'$ , is given by

$$F' = fD = f\epsilon A \cos^2\left(\frac{\pi}{2}(\lambda - \lambda_c)/r_\lambda\right) \cos^2\left(\frac{\pi}{2}(\phi - \phi_c)/r_\phi\right) \quad (2.4)$$

with  $D$  the divergence of maximum amplitude  $A = 3 \cdot 10^{-6} \text{ s}^{-1}$ , which corresponds to the outflow consistent with about 5 mm per day of tropical precipitation (Hoskins and Ambrizzi 1993),  $\lambda$  denotes the longitude,  $\phi$  the latitude,  $r_\lambda$  and  $r_\phi$  the zonal and meridional extent of the source respectively and  $\lambda_c$  and  $\phi_c$  the position of the source. Here  $|\lambda - \lambda_c| \leq r_\lambda$  and  $|\phi - \phi_c| \leq r_\phi$ . Furthermore we linearise by setting  $\epsilon = 10^{-6}$  so that the non-linear terms are negligible. The response shown in the figures is the calculated response multiplied by  $\epsilon^{-1}$  so that it corresponds to the linear response to 5 mm precipitation per day.

### 2.3.2 Experimental design

For a range of idealized jet structures we quantify the ability of the jet to trap Rossby wave energy. The general idealised jet structure we use is zonally symmetric and has a gaussian profile. This simple profile is remarkably similar to the observed profile as can be seen in Fig. 2.6. For a given particular jet structure  $\zeta_b$ , we calculate the forcing  $F$  (2.3) that makes this jet stationary and add a particular  $F'$  according to (2.4). We then integrate the barotropic model for 20 days, starting from  $\zeta_b$ , and average the response  $\zeta' = \zeta - \zeta_b$  between day 10 and 20. The first 10 days are discarded to enable the Rossby wave energy to disperse around the hemisphere. We verified that averaging over days 20 – 30 does not change the results qualitatively. In the observational analysis we found that jets do not remain quasi-stationary for much longer than 10 – 20 days so it makes sense to look at the response at this timescale and not longer. As a quantitative measure of the “waveguidability” of the imposed jet we choose the area-average of the squared value of the meridional wind

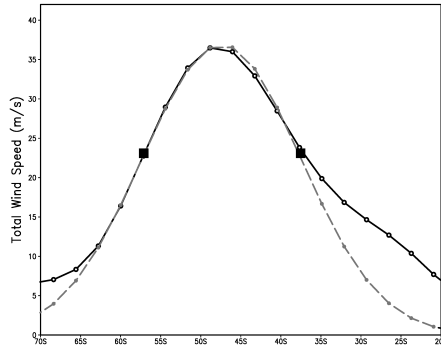


**Figure 2.6:** The black curve is the mean meridional total wind profile of the strongest part of the observed mean summer jet in the SH averaged over longitudes  $0 - 100^\circ E$ . The dashed grey curve is a fitted Gaussian function. The inflection points are indicated. The distance between the inflection points defines the width of the jet.

component of the response in the area of the jet as is defined in section 2.2:

$$wd = \frac{1}{A} \iint v'^2 d\lambda d\phi \quad (2.5)$$

Where  $v$  denotes the meridional wind and  $A$  the area of the jet. We call this measure the waveness  $wd$ .

We calculated the waveness of the response for a range of jet widths and strengths to an elliptical RWS at  $15^\circ S/0^\circ W$  with a meridional radius of  $r_\lambda = 15^\circ$  and a zonal radius of  $r_\phi = 30^\circ$ . This idealised RWS is not unreasonable for an outflow associated with a tropical precipitation anomaly. To check the sensitivity of the results for the particular choice of the RWS, we repeated the calculations for a circular RWS of  $15^\circ$  radius. The core of the jet was positioned at  $35^\circ S$  and  $50^\circ S$ . The results are discussed in the next section.

## 2.4 Waveguidability of Idealised Jets

Fig. 2.7 shows a few typical examples of the response for various idealised jets. The response in Fig. 2.7a is for a relatively weak and wide jet located at  $35^\circ S$ . The response is rather restricted locally to the region of the source with some downstream propagation along the waveguide but in



addition marked meridional propagation of Rossby wave energy is visible as well. For a stronger and narrower jet, the response is much stronger and of hemispheric nature and almost strictly zonal (Fig. 2.7b). For the same jet at a more southerly location of  $50^\circ S$  the response to the same RWS is weaker and the zonal wavenumber of the response drops from 4 to 3 (Fig. 2.7c). If the RWS is also moved southwards to keep the distance between the jet and the RWS the same as in Fig. 2.7b then the response retains a wavenumber 3 spatial structure but with a different phase and its amplitude is much larger (Fig. 2.7d).

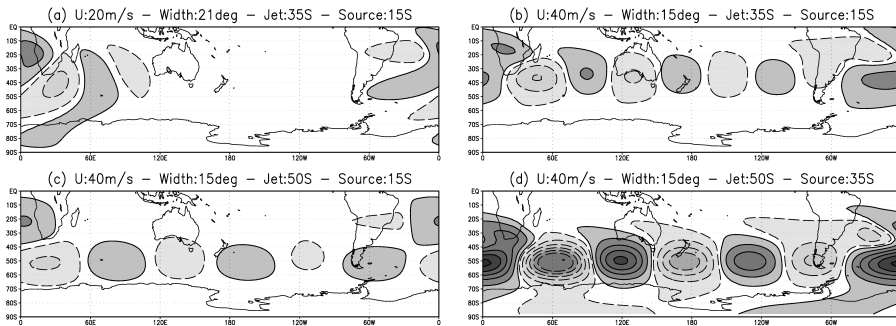


**Figure 2.7:** Meridional wind anomalies of the response of the barotropic model to a Rossby Wave Source (see text for details). The response is defined as the average over days 10 – 20. The forcing is elliptic with meridional radius of  $15^\circ$  and  $30^\circ$  zonal, centered at  $15^\circ S - 0^\circ E$ . In (a) the response is for a slow and wide jet ( $U = 20 \text{ m s}^{-1}$ , width =  $21^\circ$  with the jet core at  $35^\circ S$ ), in (b) for a fast and narrow jet ( $U = 45 \text{ m s}^{-1}$ , width =  $13^\circ$ , and in (c) a jet with same speed and width as in (b) but positioned at latitude  $50^\circ S$ . The contour interval is  $2 \text{ m s}^{-1}$  and negative values are dashed. In (d) the jet is as in (c) but the RWS is moved to  $30^\circ S$  to have the same distance to the jet as in (a) and (b).

A summary of the wavenumber of the response experiments for the range of jet widths and speeds as found in the observations at section 2.2 is plotted in Fig. 2.8 for a jet at  $35^\circ S$  (a) and  $50^\circ S$  (b) with the RWS set at  $15^\circ S$  and for a jet at  $50^\circ S$  and the RWS at  $30^\circ S$  (c). The jet speeds are increased in steps of  $1 \text{ m s}^{-1}$  speed and the jet width in steps of  $0.707^\circ$ . To check the sensitivity for the specification of the source, we repeated the calculations for the jet at  $35^\circ S$  but with a circular RWS of  $15^\circ$  radius (d). The white area marks narrow fast jets that are barotropically unstable with e-folding timescales of the most unstable normal mode shorter than 10 days verified independently with a normal mode computation (not

shown). These jets are excluded from our analyses since these jets do not survive long enough for Rossby wave energy to propagate around the hemisphere.

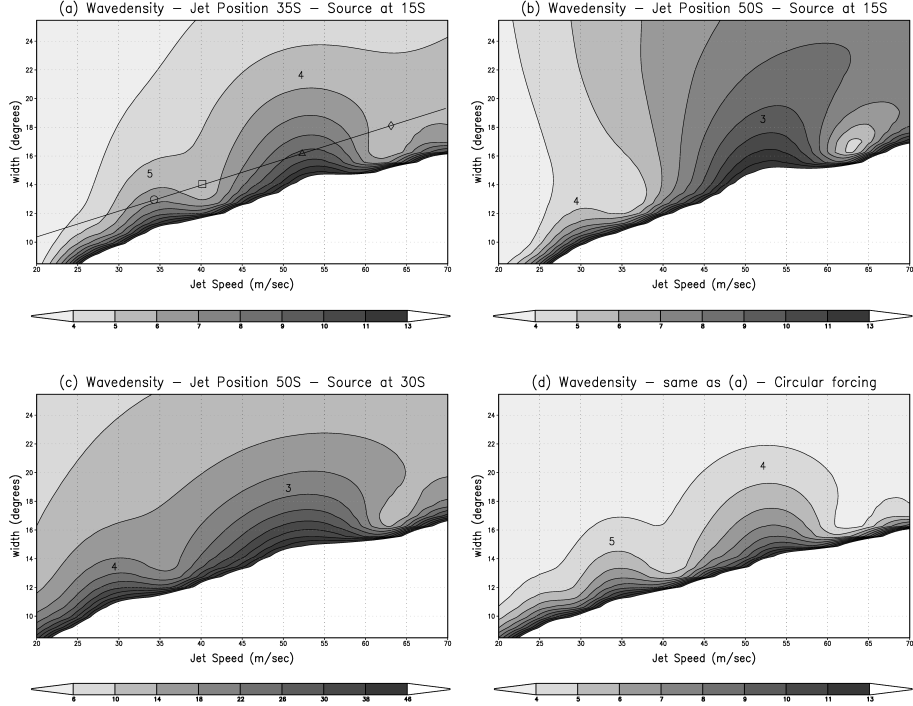


**Figure 2.8:** Averaged wavenumber from days 10 to 20 of the barotropic model response to the same RWS as in figure 2.7 for jets of various strengths and widths in steps of  $1 \text{ m s}^{-1}$  and  $0.707^\circ$  respectively. In (a) the jet is positioned at latitude  $35^\circ S$  and in (b) at latitude  $50^\circ S$ . The contour interval of the wavenumber is  $1 \text{ m s}^{-1}$ . In (c) the RWS is moved to  $30^\circ S$  for the same jet characteristics as (b). In (d) the jet is as in (a), the RWS is in the same position but it has a circular shape of  $15^\circ$ . The white area corresponds to barotropically unstable jets with the most unstable mode having an e-folding time shorter than 10 days. The area below the dashed lines indicates jets for which a necessary, but not sufficient condition for barotropic instability is satisfied. The condition is a change in sign of the meridional gradient of absolute vorticity. The symbols on the solid line in (a) indicate jet configurations for which the response pattern is shown in Fig. 2.9.

For a given jet speed, the wavenumber of the response increases monotonically when the jet becomes narrower. For instance for the jet at  $35^\circ S$

at a speed of  $35 \text{ ms}^{-1}$  (Fig. 2.8a) the wavenumber increases from below 4 for jet widths around  $24^\circ$  to around 11 for jet widths around  $11^\circ$ . For a given jet width, the wavenumber increases as the jet speed increases. For instance at a jet width around  $14^\circ$  the wavenumber increases from below 4 at jet speeds of  $20 \text{ ms}^{-1}$  to 12 for jet speeds around  $50 \text{ ms}^{-1}$ . However, this latter increase is non-monotonic. Maxima in the response are found for jet speeds around 35, 54 and  $68 \text{ ms}^{-1}$  for the jet at  $35^\circ S$ . For the jet at  $50^\circ S$  (Fig. 2.8b and 2.8c) maxima are found around 30 and  $53 \text{ ms}^{-1}$ . When for the jet at  $50^\circ S$  the RWS is moved  $15^\circ$  to the South (Fig. 2.8c) in order to have the same distance between the jet and the RWS as in Fig. 2.8a, the maxima occur around the same wind speeds, only the dependence of the response on the width of the jet changes. Also a different RWS does not change the values of the wind speed for which a maximum response is found (compare Fig. 2.8a and Fig. 2.8d). The positions of the maxima do not depend on the distance of the RWS to the jet, nor on the width of the jet or the particular shape of the RWS, but they do depend on the latitude and speed of the jet. So what causes these maxima ?

## 2.5 Resonance

A Rossby wave is stationary if its intrinsic westward phase velocity exactly matches the eastward background flow velocity. As the jet speed increases, the stationary wave number decreases due to the property of Rossby waves that the westward phase velocity increases for larger waves. Fig. 2.9 shows the response averaged over days 10 – 20 for various jet speed-width combinations along the black solid line at the position of the symbols in Fig. 2.8a. The maxima in the wavenumber response coincide with a stationary wave response with an integer number of zonal wavenumbers around the jet, 5 at a jet speed of around  $35 \text{ ms}^{-1}$  (circle) and 4 for jet speeds around  $54 \text{ ms}^{-1}$  (triangle). If the stationary zonal wavenumber is integer then the wave is in phase with the RWS and maximal constructive interference is expected and thus a maximum in the wavenumber response. On the other hand, if the stationary wave response is an integer number of wavenumbers around the jet plus half a wavelength, then maximum destructive interference is expected and a relative minimum in the wavenumber response. This situation occurs for jet speeds around 40 (square) and  $62 \text{ ms}^{-1}$  (diamond). For the jet at  $50^\circ S$  wavenumber 4 is stationary around  $30 \text{ ms}^{-1}$  and wavenumber 3 around  $53 \text{ ms}^{-1}$ .

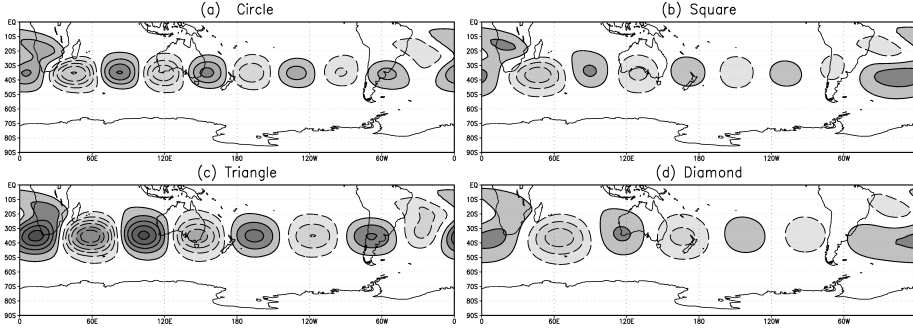


**Figure 2.9:** Meridional wind response patterns calculated with the barotropic model versus wind speed for the jet at  $35^\circ\text{S}$  for the speed-width combinations indicated by the symbols in Fig. 2.8a. The response is averaged over days 10 – 20. Contour intervals are  $3 \text{ m s}^{-1}$ .

In order to calculate the stationary wave number for the waves trapped in the idealized jets, we start from the barotropic vorticity eq. (2.1) without forcing and dissipation using cartesian coordinates

$$\frac{\partial \zeta}{\partial t} + \frac{\partial \psi}{\partial x} \frac{\partial(\zeta + f)}{\partial y} - \frac{\partial \psi}{\partial y} \frac{\partial(\zeta + f)}{\partial x} = 0. \quad (2.6)$$

Assuming stationarity and making the beta-plane approximation we get

$$\frac{\partial \psi}{\partial x} \left( \frac{\partial \zeta}{\partial y} + \beta_0 \right) - \frac{\partial \psi}{\partial y} \frac{\partial \zeta}{\partial x} = 0. \quad (2.7)$$

with

$$\beta_0 = \left. \frac{\partial f}{\partial y} \right|_{\phi=\phi_0} \quad (2.8)$$

evaluated at the latitude of the jet,  $\phi_0$ . Now we consider a stationary zonal basic state with a perturbation super imposed

$$\psi(x, y, t) = \overline{\psi(y)} + \psi'(x, y) \quad (2.9)$$

and substitution gives

$$\frac{\partial \psi'}{\partial x} \left( \frac{\partial \overline{\zeta}}{\partial y} + \frac{\partial \zeta'}{\partial y} + \beta_0 \right) - \frac{\partial \zeta'}{\partial x} \left( \frac{\partial \overline{\psi}}{\partial y} + \frac{\partial \psi'}{\partial y} \right) = 0. \quad (2.10)$$

which reduces to

$$\frac{\partial \psi'}{\partial x} \left( \frac{\partial \bar{\zeta}}{\partial y} + \beta_0 \right) - \frac{\partial \zeta'}{\partial x} \frac{\partial \bar{\psi}}{\partial y} = 0. \quad (2.11)$$

when we neglect second order terms. Using the relation between zonal wind and stream function  $U = -\frac{\partial \psi}{\partial y}$  and vorticity and stream function  $\zeta = \nabla^2 \psi$  this can be rewritten as

$$\frac{\partial \psi'}{\partial x} \left( -\frac{\partial^2 \bar{U}}{\partial y^2} + \beta_0 \right) + \bar{U} \frac{\partial \zeta'}{\partial x} = 0. \quad (2.12)$$

We approximate the behavior of Rossby waves trapped in the waveguide by Rossby waves in a channel centered at the latitude of the jet. For the waves we assume the following form

$$\psi'(x, y) = \sin(\tilde{l}y) e^{i\tilde{k}x} \quad (2.13)$$

where  $\tilde{l} = \frac{\pi}{W}$ ,  $\tilde{k} = k \frac{2\pi}{L}$ ,  $k$  is the zonal wavenumber,  $y \in [0, W]$  and  $x \in [0, L]$ ,  $W$  the width of the channel and  $L = 2\pi R \cos(\phi)$  the length of the channel,  $R$  the radius of the earth and  $\phi$  latitude. The vorticity field of these waves is given by

$$\zeta'(x, y) = -\left( \tilde{k}^2 + \tilde{l}^2 \right) \psi'(x, y) \quad (2.14)$$

An expression for the stationary zonal wavenumber can be found by substitution of (2.13) and (2.14) into (2.12)

$$i\tilde{k}\psi' \left[ -\frac{\partial^2 \bar{U}}{\partial y^2} + \beta_0 - \bar{U} \left( \tilde{k}^2 + \tilde{l}^2 \right) \right] = 0. \quad (2.15)$$

This can only be true for all  $x \in [0, L]$  if

$$\sin(\tilde{l}y) \left[ -\frac{\partial^2 \bar{U}}{\partial y^2} + \beta_0 - \bar{U} \left( \tilde{k}^2 + \tilde{l}^2 \right) \right] = 0. \quad (2.16)$$

Integrating over  $y$  gives

$$-A + \frac{2}{\pi} \beta_0 - B \left( \tilde{k}^2 + \tilde{l}^2 \right) = 0 \quad (2.17)$$

with

$$A = \frac{1}{W} \int_0^W \sin(\tilde{l}y) \frac{\partial^2 \bar{U}}{\partial y^2} dy \quad (2.18)$$

and

$$B = \frac{1}{W} \int_0^W \sin(\tilde{l}y) \bar{U} dy. \quad (2.19)$$

Rewriting gives the following expression for the stationary wave number

$$k = \frac{L}{2\pi} \sqrt{\frac{\frac{2}{\pi}\beta_0 - A}{B} - \frac{\pi^2}{W^2}} \approx \frac{L}{2\pi} \sqrt{\frac{2\beta_0}{\pi B}} \quad (2.20)$$

For a basic state given by

$$\bar{U}(y) = U_0 \sin(\tilde{l}y) \quad (2.21)$$

the expression for the stationary wavenumber reduces to

$$k = \frac{L}{2\pi} \sqrt{\frac{4\beta_0}{\pi U_0}} \quad (2.22)$$

In this expression the stationary wavenumber depends only on the latitude through  $L$  and  $\beta_0$  and on the speed of the jet  $U_0$ . In order to relate these results to the waveguide response calculations with the barotropic model, we need to take into account that the waveguide response pattern is different from the sinusoidal profile assumed here and that the idealized jet profile is Gaussian and not sinusoidal. Different profiles lead to different values of the integral  $B$ . This integral is proportional to the strength of the jet. Setting  $B = cU_0$  in (2.20) and choosing suitable values for  $c$ , we obtain an excellent agreement: the stationary zonal wave number is integer for the jet speeds with maximum waveguide response. This supports the hypothesis that the maximum response is due to constructive interference between the source and the Rossby wave energy that has propagated around the hemisphere. The stationary wavenumber is plotted in Fig. 2.10 for a jet at  $35^\circ S$  with  $c = 0.38$  and  $50^\circ S$  with  $c = 0.33$  and the solid dots indicate the jet speeds for which the waveguide response is maximum. The open dots mark the position of minimum waveguide response. These do not occur at exactly the jet speed for which the calculated stationary wavenumber is an integer and a half, especially for the fast jets beyond  $60 \text{ ms}^{-1}$ , but there will be destructive interference between the source and the Rossby wave energy that has propagated around the hemisphere.

## 2.6 Conclusions and Discussion

Characteristics of the SH summer and NH winter jet stream are analyzed from 10 day mean ERA-Interim reanalysis data for the years 1979 – 2011.

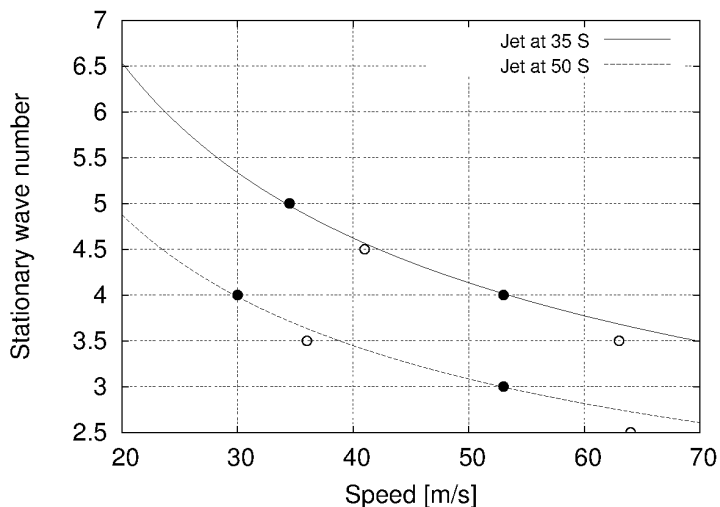


**Figure 2.10:** Stationary zonal wavenumber as a function of jet speed for a jet at  $35^{\circ}S$  and  $50^{\circ}S$ . The solid dots mark the position of the jet speeds with maximum response in the waveguide in the barotropic model calculations. These occur for jet speeds for which the stationary wave number is integer. The open dots mark the position of minimum response for which the stationary wavenumber is close to an integer and a half.

Idealized jets are constructed that cover the range of observed jet speeds and widths. With barotropic model calculations we determined the waveguidability of these jets by examining the linear response to a subtropical Rossby wave source. We find that the properties of the jet constrain the zonal waves that result from Rossby wave propagation from a subtropical Rossby wave source. The overall effect is that stronger and narrower jets lead to stronger zonal waves and the stronger the jet the smaller the wavenumber. A maximum response is found when the stationary wavenumber is integer through constructive interference between the source and the response.

In the Southern Hemisphere summer season, the season with the most zonally symmetric jets, we tried to verify these relationships. First we defined the area of the jet by considering regions with a total wind speed in excess of  $25 \text{ m s}^{-1}$ . Next we calculated at each longitude within these regions the value of the maximum total wind and the width of the jet and averaged these values over the longitudes within the jet regions. We

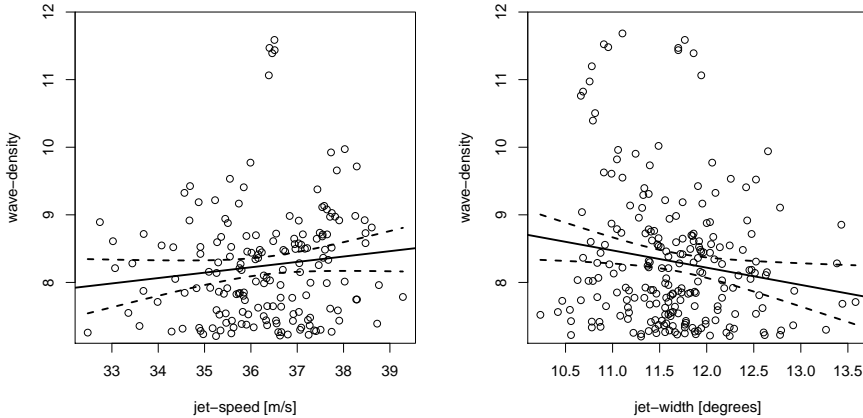


**Figure 2.11:** Wavedensity as a function of the jet width (left) and jet speed (right) based on the ERA-Interim dataset. The wavedensity as a function of jet width is calculated over areas where the jet speed lies between 20 and 35  $ms^{-1}$ . Only days are considered with the observed wavedensity in the jet region larger than one standard deviation. The wavedensity as a function of jet speed is calculated for jets with width's between  $11.5^{\circ}$  and  $12.5^{\circ}$ .

then calculated the area averaged value of the meridional wind anomaly inside the jet regions (= wavedensity). From the wavedensity distribution of the total 2880 SH summer days (32 years) we selected only the days where the wavedensity exceeds one standard deviation (one sigma). Fig. 2.11 shows the wavedensity as a function of jet width (left panel) and jet speed (right panel) for days with wavedensity in the jet region above one standard deviation. In accordance with the barotropic model results higher values of wavedensity tend to co-occur with faster and narrower jets. However, there is a large scatter in the results and the relation is barely significant. A couple of reasons can be given why the signal to noise ratio is so low in the observations. First of all, in reality there is no completely steady source of Rossby wave energy as in the idealised calculations. As a result days occur where there are strong, narrow jets but virtually no wavedensity due to the lack of sources of Rossby wave energy. That is the reason for restricting the analysis to days with wavedensity in the jet region above one standard deviation. We checked that the analysed relation between wavedensity and jet speed and width is not very sensitive to this exact value of the threshold of one sigma. In addition, in reality, Rossby waves may grow to large amplitudes, break



and strongly interact with the background flow. Moreover, the observational jet stream deviates from the zonal jets that we consider and has discontinuities that affect the wave and energy propagation. Finally, the baroclinicity of the jet may play a role in the generation and maintenance of the zonal waves. These processes are neglected in the barotropic model calculations. Notwithstanding, the predicted basic relationship between jet speed and width and waveguidability still seems to hold.

The results of this chapter may be of help in the interpretation of climate change projections. Often climate models simulate a change in the stationary wave pattern that has the character of a zonal wave co-aligned with the jet (Selten et al 2004), (Brandefelt and Körnich 2008), (Branstator and Selten 2009). Differences between different models might be due to differences in the simulation of a stationary Rossby wave source (for instance a change in the mean tropical precipitation) or differences in the strength, width or location of the jet.

*Acknowledgments.* ECMWF ERA-Interim data used in this chapter have been obtained from the ECMWF Data Server. This work is part of the research programme INATEX, which is (partly) financed by the Netherlands Organisation for Scientific Research (NWO).



---

## CHAPTER 3

---

# Drivers of North Atlantic Oscillation Events

Iris Manola, Reindert J. Haarsma and Wilco Hazeleger  
*Tellus A.65, (2013)*

### **Abstract**

This chapter is set out to quantify the contribution of tropical and extratropical atmospheric forcing mechanisms to the formation of the North Atlantic Oscillation (NAO) pattern. Although the NAO varies on a wide range of time scales we focus on 10 – 60 days. At these time scales mechanisms are at play in the atmosphere that can generate the characteristic dipole pattern. We focus on the tropical Rossby Wave Source (RWS) and extratropical eddy activity. Anomalous tropical and extratropical vorticity forcing associated with the NAO is derived from atmospheric reanalysis data and applied in an idealized barotropic model. Also, using winds from composites of the NAO, the vorticity forcing is derived inversely from the barotropic vorticity equation. Both types of forcing are imposed in the barotropic model in the tropics and extratropics respectively. An important result is that the tropics dampen the NAO as a result of a negative feedback generated in the extratropics. The damping is strongest, about 30%, for the negative phase of the NAO. For the positive phase the damping is about 50% smaller. The results show that the barotropic vorticity equation can represent the dynamics of both tropical and extratropical forcing related to the formation of the NAO patterns.

### 3.1 Introduction

The North Atlantic Oscillation (NAO) is the major source of atmospheric variability over the Northeast Atlantic, Europe and North America (Branstator (2002)). NAO plays an important role in the formation of the prevailing weather patterns and their day-to-day variations (Platzman (1968)). The NAO is predominantly generated by extratropical dynamics, which involves extratropical eddy fluxes, wave breaking activity and shifts in the storm tracks. In addition to that the NAO is affected by tropical deep convection associated with sea surface temperature (SST) anomalies. However the role of the tropical forcing in the development of the NAO pattern is yet to be fully clarified.

It is widely investigated and accepted that the NAO is primarily forced by extratropical atmospheric variability, such as the eddy activity and wave breaking (for instance, Feldstein (2003), Thompson et al (2003), Vallis et al (2004)). Results from model and observational studies by Franzke et al (2003), Benedict et al (2004) and Riviere and Orlanski (2007) indicate that the development of the NAO depends on synoptic scale wave breaking. They found that anticyclonic wave breaking is associated with the positive phase of the NAO and cyclonic wave breaking with the negative phase. Successive upstream wave breaking is responsible for the maintenance of the event. The phases of the winter NAO are also found to be associated with shifts in the storm tracks (Rogers (1990), Hurrell (1995)). The dependency of the development of the NAO on the eddy fluxes characterizes it as a phenomenon associated with non-linear processes. Li et al (2007) conclude, by imposing an idealized forcing on a linear baroclinic model, that transient eddy forcing induces the NAO dipole with a preferred location at the exit of the Atlantic jet stream.

Apart from the known extratropical origin of the NAO, there are also studies that show the importance of the tropical impact on the NAO. They suggest that tropical variability is an important source for forcing the prevailing wintertime extratropical patterns and atmospheric trends (Sardeshmukh et al (1987), Lin et al (2002), Lu et al (2004), Selten et al (2004) and more). Changes in the tropical SSTs can excite Rossby waves that can propagate from the tropics to the extratropics creating teleconnection patterns (Hoskins and Karoly (1981), Hoskins and Ambrizzi (1993)). It is argued that the upward trend of tropical-wide SSTs projects onto the polarity of the NAO (Hoerling et al (2004), Hurrell et al (2004)). Peterson et al (2002) used a dry primitive equation model forced with

diabatic heating in the tropics and extratropics to find that, although the overall influence of the extratropics is stronger, the trend in the NAO is related to the tropical forcing. Greatbatch et al (2012), in order to analyze the interannual trend of the NAO, applied a relaxation technique to argue that on timescales larger than 21 years the tropics are influential, while for shorter timescales the extratropics and the stratosphere are the major sources of variability.

Along the tropical belt there are preferred regions where the SST forcing projects more strongly onto the NAO. The phase of the NAO is related to the region of tropical forcing according to Cassou (2008). Positive NAO events mostly respond to Madden-Julian Oscillation disturbances in the tropical Western-Central Pacific, while negative NAO events are found to be influenced by the tropical Eastern Pacific-Western Atlantic, leading to changes along the North Atlantic storm track. Tropical Atlantic SST anomalies are found to induce a significant NAO dipole in late winter simulations but not in early winter (Peng et al (2005)). Another study by Okumura et al (2001) shows that tropical Atlantic forcing creates a barotropic teleconnection pattern projecting onto the NAO. The importance of the Indian Ocean is pointed out by Hoerling et al (2004). They used enhanced SSTs over the Indian Ocean, resembling the observed warming since 1950 to force a coupled model and concluded that Indian Ocean warming projects strongly onto the positive NAO (see also Lu et al (2004)).

Here, we aim to study the atmospheric forcing of the NAO with a focus on the tropics. Feldstein (2003) suggests that the NAO has an intrinsic timescale of about 10 days. However, the Rossby wave source (RWS, see Sardeshmukh et al (1987)), which is an estimate of the driving force from the tropics, and the consequent propagation of anomalies towards the extratropics has a longer time scale. Indeed, for the timescale of 1 – 10 days in boreal winter a selection of positive and negative NAO events is made (see section 3.2 for the definition of the NAO events) and for these events the composites of RWS anomalies are computed, there are almost no pattern similarities between the RWS patterns for the two NAO phases. This indicates that for timescales shorter than 10 days the NAO is mainly driven by the extratropics and the influence of the tropics is negligible. Because our focus is on the impact of the tropics, timescales shorter than 10 days are excluded in this study.

For the timescale of 10 – 60 days the equivalent RWS composites are shown in Fig. 3.1 (see section 3.3 for details). For the two NAO phases

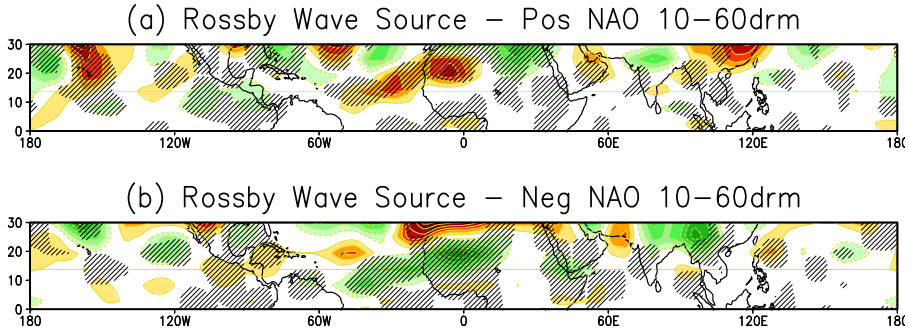


**Figure 3.1:** Composites of RWS anomalies at 300hPa for (a) positive and (b) negative NAO event days from 10 – 60 day means of DJF months for the period 1979–2010 using ERA-Interim data. The contour interval is  $7 \cdot 10^{-12} s^{-2}$ . Negative values are shown in green color. The hatched black lines indicate the areas exceeding the level of 99% significance.

the RWS anomalies show a similar structure with opposite sign and the patterns are -0.67 correlated in the areas of high significance. This anti-correlation of the RWS suggests the hypothesis that the NAO can affect the dynamical tropical forcing. Later in this chapter this hypothesis is verified. These tropical changes subsequently may affect the extratropical circulation and can be of importance for the formation of the NAO patterns. In addition, the stationary winter Rossby wave patterns develop within this timescale. Finally, this time scale also captures the intraseasonal variability in tropical convection which is an effective source of Rossby waves and excludes higher frequency phenomena such as breaking waves along the storm tracks and other transient eddies that make the flow sharper and more scattered, while their important impact on the larger scale is still evident.

Prompted by the above observations we attempt to quantify the tropical impact onto the NAO in addition to the dominant extratropical forcing within the timescale of 10 – 60 days, using extreme positive and negative NAO events in a barotropic model. We use the barotropic model as a diagnostic tool assuming that the dynamics of the NAO is equivalent barotropic. The NAO patterns are interpreted in meridional wind anomalies in order to highlight the wave-like structure of the NAO, similarly to Branstator (2002) and Watanabe (2004). The linearity of the tropical and

extratropical influence for the two phases is also discussed. Finally an effort is made to investigate whether there are preferred longitudinal regions in the tropics that force the NAO.

The chapter is structured as follows. In section 3.2 the data and the definition of the NAO events are introduced and the characteristics of the composites of the events are displayed. In section 3.3 we focus on the possible observational tropical and extratropical forcing sources. In section 3.4 the model and the experiment are described. The results of the model simulations are presented in section 3.5 and in section 3.6 a summary and discussion finalize this work.

## 3.2 The NAO Events

### 3.2.1 Characterization of the NAO events

We use the ERA-Interim reanalysis data (Dee and Coauthors (2011)) for Northern Hemisphere December-January-February months (DJF) from 1979 to 2010 and focus on the 10 – 60 days time scale. This time filtering was obtained by subtracting the 60 day running mean from the 10 day running mean. To retain the daily cycle the daily climatology was added to the resulting time series. The running means were applied over the period 1 December - 28 February. For winds we used the 300hPa level which is a good compromise between the Rossby wave propagation level (optimum at 200hPa) and the equivalent barotropic level at about 350hPa, (Hoskins and Ambrizzi (1993), Ting (1996)).

The NAO index is defined as in Branstator (2002), i.e. the first EOF of the streamfunction at 850hPa. The domain used is the Atlantic sector from 90°W to 30°E over the Northern Hemisphere. The leading EOF explains 35% of the total variance. The timescale of the index is similarly 10–60 days, while extra smoothing with a Hanning window of 11 days was needed in order to select the NAO events. The selection of the positive (negative) NAO events was based on the following criteria: the NAO index increases (decreases) monotonically for one week to reach a value above one standard deviation (below minus one standard deviation) at least for one day and then decreases (increases) monotonically for the following week. From the event the middle day, which is the day with the maximum (minimum) index is selected. With this method 63 positive and 56 negative events are identified during the 32 winters.

### 3.2.2 The NAO patterns

The composites of the total wind and meridional wind anomalies of the positive and negative phase events at 300hPa are shown in Fig. 3.2. The most pronounced differences are found over the North Atlantic. During the positive NAO phase the North Atlantic jet stream, indicated by the total wind speed (Fig. 3.2a), is shifted northward and tilted southwest-northeast towards Northern Europe and is clearly separated from the subtropical Asian jet. Over the same region the negative phase (Fig. 3.2b) is accompanied by a shorter Atlantic jet, more zonally oriented, situated at a more southern latitude in the subtropics and more closely connected to the Asian jet.

The meridional wind anomalies associated with both phases of the NAO (Fig. 3.2c and 3.2d) display a rather similar pattern with opposite sign and a spatial correlation in the extratropics of -0.76. They consist of a midlatitude wavetrain with wavenumber 4–5, where the dominant part begins at the North American west coast and ends at the Arabian peninsula. The strongest anomaly is centered at the North Mid-East Atlantic and is positive (negative) for positive (negative) NAO. The geopotential height anomalies at 500hPa, showing the well known dipole NAO pattern are denoted by black contours. The patterns of the two NAO phases do not exactly mirror each other, suggesting that there should be differences in the dynamics that generate these phases (see also Cassou et al (2004), Peterson et al (2002), Greatbatch and Jung (2006)).

## 3.3 Sources of NAO Forcing

### 3.3.1 Tropics: Rossby Wave Source

As stated in the Introduction, anomalous divergence can force a Rossby wave-train from the tropics to the extratropics. The anomalous divergence can be created by tropical anomalous SSTs and diabatic heating.

The Rossby wave source in an equivalent barotropic atmosphere assuming negligible vertical advection and twisting terms may be approximated as:

$$S = -\nabla \cdot (\zeta + f)V_{\chi}, \quad (3.1)$$

where  $\zeta$  is the relative vorticity,  $f$  the Coriolis parameter and  $V_{\chi}$  the divergent component of the horizontal wind.



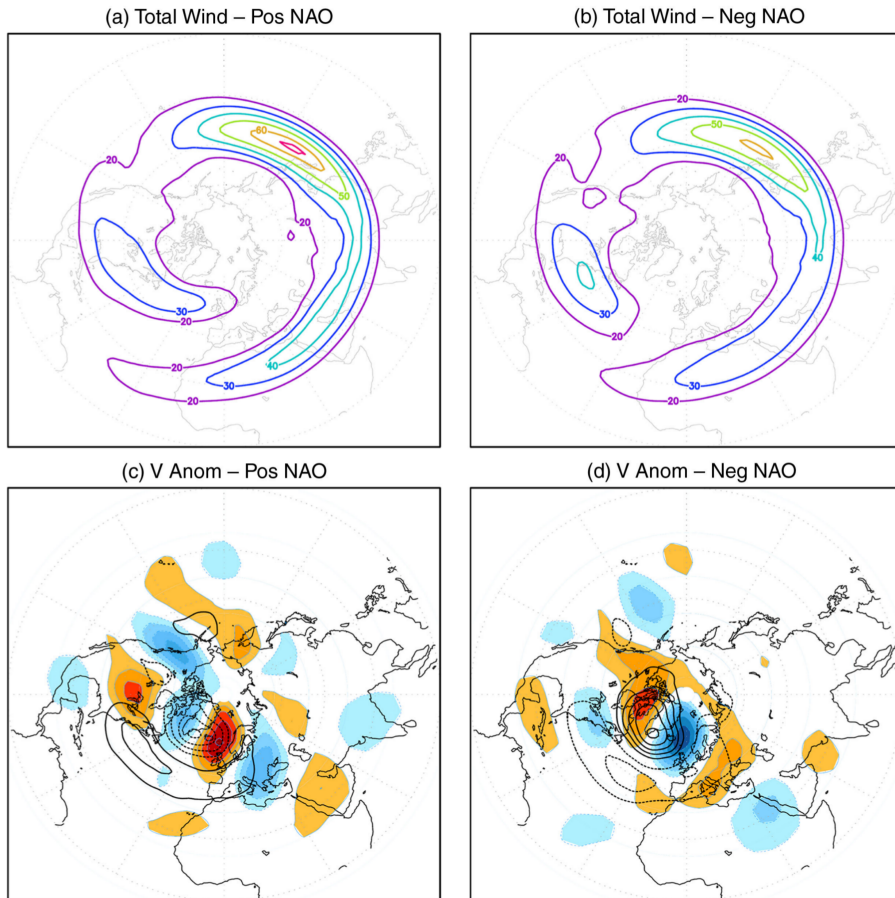


**Figure 3.2:** Panel (a) is the composite of total wind speed for positive NAO events and (b) for negative events. The contour interval is  $10\text{m s}^{-1}$ . Composites of the meridional wind anomalies are shown in (c) for positive and in (d) for negative NAO events. The contour interval is  $1\text{m s}^{-1}$  and negative values are indicated by blue colors. Over the meridional wind anomalies the geopotential height anomalies at 500hPa are plotted. The contour interval is  $35\text{m}$  and the negative values are indicated with dashed contours.

In Fig. 3.1 the Rossby wave source anomalies for positive and negative NAO events are depicted. Distinct anomalies of regional scale are shown that are well structured, especially at higher latitudes. The pattern is similar and of opposite sign for the two phases. The areas of high

significance are -0.67 correlated. The significance is computed with a Student's t-test. The magnitude of the anomalies is rather uniformly spread indicating that the tropical NAO forcing is not strongly constrained to specific longitudinal regions, except for the East Atlantic and East Pacific/Caribbean where the anomalies are somewhat larger. This is further examined in section 3.5.3.

### 3.3.2 Extratropics: Eddy Activity Forcing

The NAO in the extratropics is mainly forced by eddy activity. The highest eddy activity is found along the extratropical storm tracks. Shifts in the storm tracks are essential for the establishment and maintenance of the stationary wave patterns that create teleconnections such as the NAO. It should be noted that the state of the NAO can influence back the eddy activity, but here we focus on the one-way relationship.

The contribution of the eddy activity to the time mean flow can be computed straight forwardly by applying Reynolds decomposition to the momentum equations (Kok and Opsteegh, 1985):

$$F_{Ex} = -\left(\frac{1}{\alpha \cos \phi} \frac{\partial \overline{u'^2}}{\partial \lambda} + \frac{1}{\alpha} \frac{\partial \overline{u'v'}}{\partial \phi}\right), \quad (3.2)$$

and

$$F_{Ey} = -\left(\frac{1}{\alpha \cos \phi} \frac{\partial \overline{u'v'}}{\partial \lambda} + \frac{1}{\alpha} \frac{\partial \overline{v'^2}}{\partial \phi}\right), \quad (3.3)$$

where we have neglected the curvature and the vertical advection terms. The overbars denote the time means and the primes denote the anomalies. By applying the rotation operator on (3.2) and (3.3) they can be transformed into a vorticity forcing for a barotropic atmosphere:

$$F_{EV} = \frac{1}{\alpha} \frac{\partial F_{Ex}}{\partial \phi} - \frac{1}{\alpha \cos \phi} \frac{\partial F_{Ey}}{\partial \lambda}, \quad (3.4)$$

We have evaluated (3.4) using 6-hourly ERA-Interim data for positive and negative NAO events at 500hPa, which is an appropriate level for addressing baroclinic eddy activity. The anomalies are computed with respect to a 30-day running mean. The differences in the eddy forcing of the barotropic atmosphere between positive and negative NAO composite events are displayed in Fig. 3.3. Coherent differences are shown between the two phases. The largest among them are found over the Atlantic, the East Pacific/American continent and the Antarctic. Further discussion of this figure follows in section 3.5.1.

### 3.4 Model and Experimental Set-Up

The teleconnections associated with the NAO that are initiated in the tropics by the RWS are thought to be governed by equivalent barotropic dynamics. The extratropical transient eddy activity and wave breaking that influence the generation and maintenance of NAO is a baroclinic process acting on a regional scale with a timescale of 2 – 5 days. In this chapter we are however interested in the timescales of 10 – 60 days. For these spatial and time scales the impact of the eddies can be assumed to be equivalent barotropic. Therefore we use a barotropic model as a diagnostic tool to quantify the influence of tropical and extratropical sources of the NAO. A benefit from working with the barotropic model is that it provides a transparent framework for interpreting the results. Watanabe (2004) also used a barotropic model to examine the zonally oriented wave trains associated with the NAO that are concurrent with RWS anomalies.

The barotropic vorticity equation (BVE) describes the evolution of the flow of a barotropic fluid on a rotating sphere:

$$\frac{d\zeta}{dt} = \frac{\partial\zeta}{\partial t} + J(\psi, \zeta + f) + \lambda\zeta + \mu\nabla^4\zeta = F, \quad (3.5)$$

where  $\psi$  is the streamfunction,  $\zeta$  is the relative vorticity,  $f$  the Coriolis parameter,  $\lambda$  the Ekman pumping linear coefficient and  $\mu$  the super viscosity. The BVE is solved on the sphere by a spectral model with a triangular truncation of T21. The forcing  $F$  is determined as such that the background flow remains stationary ( $\frac{\partial\zeta}{\partial t} = 0$ ). The coefficients  $\lambda$  and  $\mu$  are set to 9 and 3 days respectively to keep the flow stable.

The BVE is applied to the streamfunction of NAO composites of positive and negative events and also to the mean state of all 32 winters using 10 – 60 day running means of ERA-Interim wind data at 300hPa.

The forcing that keeps the time mean winter (DJF) flow stationary is denoted as  $F_0$ . The forcings that keep the positive and negative NAO composite fields stationary are denoted as  $F_{NAO+}$  and  $F_{NAO-}$  respectively. These NAO forcings can be decomposed into a mean and an anomalous forcing:

$$F_{NAO+}^+ = F_0 + F_{NAO+}'^+, \quad (3.6)$$

and

$$F_{NAO-}^- = F_0 + F_{NAO-}'^-, \quad (3.7)$$

By restricting the anomalous NAO forcings ( $F_{NAO}^{+'}$  and  $F_{NAO}^{-'}$ ) to the tropics ( $0^\circ - 30^\circ\text{N}$ ) or the extratropics ( $30^\circ - 90^\circ\text{N}$ ) and running the BVE to equilibrium the impact of the tropical and extratropical part of the NAO forcings can be evaluated. This approach is, however, only valid if the response to the anomalous forcing is to first order linear. The response to the tropical and extra-tropical forcing can then be linearly added. We have tested the linearity by comparing the total response with the summation of the tropical and the extratropical response. The differences between these responses are indeed small, as will be discussed in section 3.5.2.

To assess the tropical and extratropical contribution to the teleconnections for each phase the weighted Kinetic Wave Energy Anomaly is computed using the meridional wind:

$$\frac{1}{N}\Sigma(V_{eq} - V_0)^2, \quad (3.8)$$

where  $V_{eq}$  is the meridional wind after the model has reached the equilibrium state and  $V_0$  the meridional wind of the composite of all 32 winters.  $\Sigma$  indicates the summation over all grid points (N).

## 3.5 Tropical and Extratropical Influence on NAO Patterns

### 3.5.1 Model-derived barotropic vorticity forcing

The anomalous vorticity forcing for the two NAO phases ( $F_{NAO}^{+'}$  and  $F_{NAO}^{-'}$ , see equations 3.6 and 3.7) are computed in the barotropic model for the tropics and the extratropics. They are displayed in Fig. 3.4. In order to verify that the BVE can be used to evaluate the dynamics of the NAO, the patterns of the model vorticity should bear resemblance to the observational forcings. However, the RWS and eddy forcing are approximations of the actual NAO forcing of the barotropic flow at one level. The forcing of the NAO in the tropics by the generation of Rossby waves that propagate to the extratropics occurs mainly in the upper troposphere. In the extratropics these Rossby waves lose their baroclinic structure and become predominantly equivalent barotropic. Similarly the amplitude of the eddy forcing varies strongly with height. Due to these approximations a direct agreement in amplitudes should not be anticipated and we will mainly concentrate our analysis on pattern comparison.

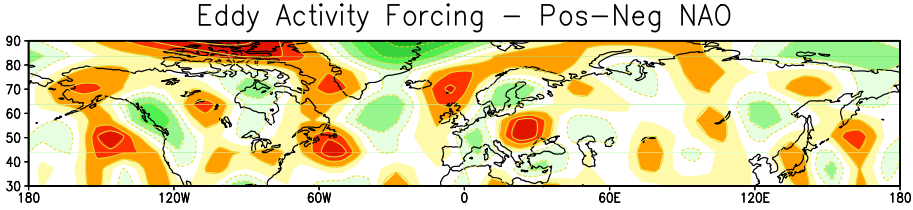


**Figure 3.3:** Anomalies of eddy activity forcing composites of positive minus negative NAO events. The data are derived from zonal and meridional wind anomalies from ERA-Interim of DJF 1979 – 2010 years. The contour interval is  $6 \cdot 10^{-12} s^{-2}$  and the green color shades indicate negative values.

For both phases of the NAO there is reasonable agreement between the anomalous model tropical vorticity forcing (Fig. 3.4a and 3.4b) and the observed RWS (Fig. 3.1) in sign and location of the pattern.

Similarly to the tropical forcing, the extratropical model vorticity forcing (Fig. 3.4c and 3.4d) has opposite sign for the two NAO phases. The anomalies in Fig. 3.4e are compared to the anomalous observational eddy activity forcing in Fig. 3.3. Although the discrepancies are somewhat larger, there are still some similarities, especially over the Atlantic and E. Pacific-American continent where the largest values are found. There, both patterns show a similar southwest-northeast chain of anomalies.

The above results indicate that the BVE, despite its approximations, can be used to evaluate the dynamics of the NAO. In addition it is confirmed that the major forcing of the NAO in the extratropics is caused by eddy forcing, whereas in the tropics it is dominated by the RWS. The ability of the BVE to present the dominant forcing in the tropics as well as the extratropics motivated us to use the BVE to analyse the impact of the tropical RWS forcing and to compare it with the extratropical eddy forcing. This is further discussed in the following paragraphs.

### 3.5.2 Assessing the tropical and extratropical impact

To investigate the impact of the tropical and extratropical forcing on generating NAO events the mean state of the atmosphere is forced in the barotropic model with the  $F'_{NAO}$  confined to  $0^\circ - 30^\circ N$  or  $30^\circ - 90^\circ N$  respectively, for both positive and negative NAO events. The model is run to equilibrium. The meridional velocity anomalies from the simulations

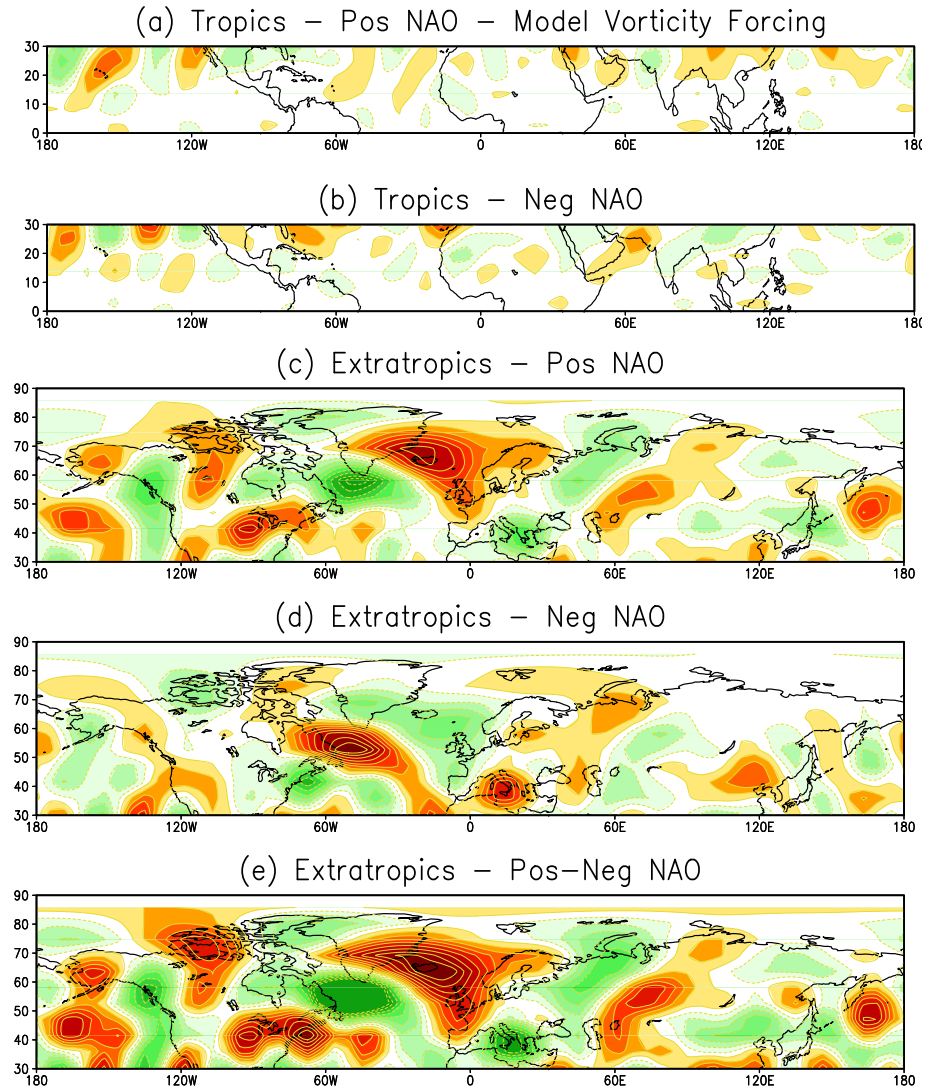


**Figure 3.4:** Composites of anomalous vorticity forcing computed in the model by solving the BVE for (a) the tropics ( $0^\circ - 30^\circ N$ ) for positive NAO events, (b) for negative NAO events and for (c) the extratropics ( $30^\circ - 90^\circ N$ ) for positive events and (d) for negative events. At (e) are the differences between positive and negative extratropical forcing. The contour interval is  $4 \cdot 10^{-10} s^{-2}$ . Negative values are indicated in green colors.

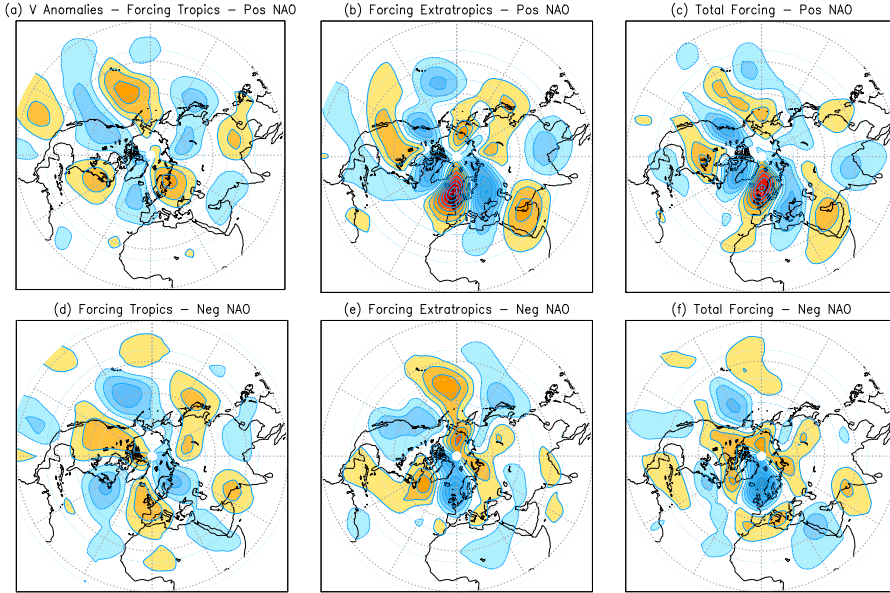


**Figure 3.5:** Meridional wind anomalies simulated by the barotropic model when the mean circulation at 300hPa is forced with the anomalous  $F'_{NAO}$  and run to equilibrium. First the forcing is restricted to the tropical band ( $0^\circ - 30^\circ N$ , left panels), where in panel (a) the positive NAO forcing ( $F'_{NAO+}$ ) is used and in (d) the negative NAO forcing is used ( $F'_{NAO-}$ ). Second, the forcing is applied only in the extratropics ( $30^\circ - 90^\circ N$ , middle panels), similarly in (b) the positive NAO forcing ( $F'_{NAO+}$ ) is used and in (e) the negative NAO forcing is used ( $F'_{NAO-}$ ). Finally to show the overall effect of using the anomalous NAO forcing, the entire hemisphere is forced, in (c) with  $F'_{NAO+}$  and in (f) with  $F'_{NAO-}$ . The contour intervals are  $1\text{m s}^{-1}$  and negative values are indicated in blue colors.

are shown in Fig. 3.5. For each NAO phase, firstly, only the response to tropical forcing is shown, then only the response to extratropical forcing and finally the response to tropical and extratropical forcing together.

A surprising result is that the responses to tropical and extratropical forcing have a similar structure but are of opposite sign. The tropical forcing thus reduces the response of the extratropical forcing. To further analyze this we have performed a lead-lag analysis between daily RWS and the NAO index, which is shown in Fig. 3.6. It reveals that the RWS is negatively correlated with the NAO and that it lags the NAO index by two days. This time scale is related to the time necessary for the NAO

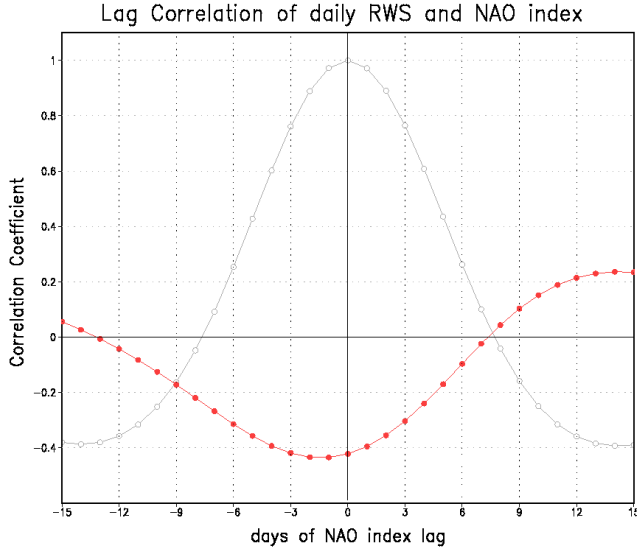


**Figure 3.6:** Red line: A lead-lag correlation of the daily RWS index and the NAO index for DJF. The RWS index is defined as the projection of the daily RWS associated with the NAO on the total RWS composite. Grey line: An auto-correlation of the NAO index. The horizontal axis denotes the lag in days of the NAO index. The vertical axis is the correlation coefficient between lagged NAO index and RWS index, or the auto-correlation coefficient of the NAO index.

to affect the tropical circulation. For large positive and negative lags the correlation becomes approximately zero. In addition the auto-correlation of the NAO, also shown in Fig. 3.6, reveals that RWS-NAO correlation has a similar damping time scale as that of the NAO. Also, the RWS-NAO becomes approximately zero when the NAO auto-correlation vanishes. We therefore conclude that the damping of the NAO by the tropical forcing is due to a negative feedback of the tropical circulation in response to the NAO that is generated in the extratropics. Earlier studies have established the connection between the NAO and the circumglobal wave guide. Watanabe (2004) has found events where anomalous convergence is established at the entrance of the Asian jet that lag the peak of the NAO by two days. This signal is associated with the decay of the NAO and subsequently propagates further downstream thereby affecting the convection on a global scale. Another hypothesis is that the trade winds associated with the Azores high can affect subtropical SSTs and through



the wind-evaporation-SST feedback the ITCZ (Chang et al (1997)). We speculate that these mechanisms might provide the negative feedback that we encountered.

To quantify the damping of the tropical forcing with respect to the extratropical forcing of the NAO, the kinetic wave energy anomaly (KWE, equation 3.8) is computed over the Atlantic region between  $30^{\circ}N$  and  $90^{\circ}N$ . The KWE resulting from tropical forcing simulations alone is compared only to that resulting from the extratropical forcing only: for the positive NAO phase the tropics comprise the 14% of the KWE sum and the extratropics the rest 86%. Compared to the positive phase, the negative phase shows enhanced tropical contribution (35%) with respect to the extratropics (65%). The above percentages are positive numbers, since the wave energy by definition is positive. Therefore it indicates only the amplitude of the influence. It should be noted that the tropical and extratropical KWE cannot be added linearly as they are quadratic quantities. The sign of the influence depends on the sign of the meridional wind anomalies, compared to the total response as seen in Fig. 3.5. Since the tropical forcing response is mainly of opposite sign to the extratropical forcing we conclude that by this percentage the tropics are damping the dominating extratropical response and reducing the amplitude of the total NAO pattern.

The non-equal contribution of the two phases is a sign of non-linearity of the NAO. This is due to the different amplitudes of the extratropical forcing during the positive and negative NAO, as is seen in table 3.1. The amplitudes are computed as the zonal average of the absolute vorticity forcing  $F'_{NAO}$ . The extratropical forcing of the positive phase is about 14% stronger than that of the negative phase, explaining why the extratropics in the positive phase play a more dominant role compared to the negative. The tropical forcing is of similar amplitude for the selected NAO events.

Peterson et al (2002), in order to assess the non-local influence on the low frequency behavior of the NAO, forced a primitive AGCM with a derived adiabatic forcing only in the tropics and the extratropics respectively. In their figures 3a and 3b the SLP differences between two periods over the Northern Hemisphere are shown when only the tropics or extratropics are forced. The patterns bear significant resemblance to our barotropic model results, indicating that indeed the dynamics can be captured by the BVE. From these figures we can also observe that forcing in the tropics results in a pattern of opposite sign to forcing in the extratropics. They also correlated the NAO index when forcing in only the

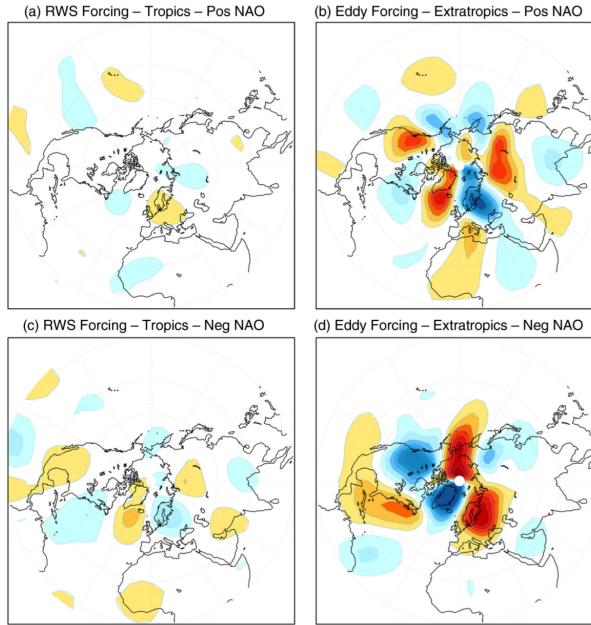


**Figure 3.7:** Similar to Fig. 3.5 but instead of the model vorticity forcing, the observational forcing is applied. At (a) is the response to the observed tropical RWS forcing for positive NAO events and (c) for negative NAO events. In (b) the forcing is the extratropical observed eddy activity for positive NAO and in (d) for negative NAO. The contour intervals are  $1\text{ms}^{-1}$  and negative values are indicated in blue colors.

tropics or extratropics with the observed index and found a correlation of 0.39 for the tropical forcing and 0.55 for the extratropical forcing.

The similarities between the observed meridional wind anomalies as seen in Fig. 3.2c and 3.2d with those reconstructed in the model by the summation of the tropical and extratropical patterns in Fig. 3.5c and 3.5f confirm that the model non-linearities do not play an important role in the simulation. Some discrepancies, mostly seen on the negative phase, can be due to numerical model approximations or non-linearities.

To further validate the results, the simulations are repeated, but instead of the model computed barotropic vorticity forcing we used the observed RWS (eq. 3.1) as the tropical forcing and the eddy activity (eq. 3.4) as the extratropical forcing. The results are shown in Fig. 3.7. Com-

	<i>Contribution</i>		<i>Vort. Forcing (<math>10^{-11} s^{-2}</math>)</i>	
	Tropical	Extratropical	Tropical	Extratropical
Pos NAO	14%	86%	1.22	3.4
Neg NAO	35%	65%	1.22	2.99

**Table 3.1:** At the left hand side the ratios of the contribution of the tropics and the extratropics for the positive and negative NAO phases are shown, quantified by the kinetic energy anomaly (eq. 3.8). At the right hand side is the zonal average of the absolute vorticity forcing  $F'_{NAO}$ , showing that the negative NAO tropical model vorticity forcing is about 14% higher in ratio between tropical-extratropical forcing than the positive phase.

parison of Fig. 3.5 with Fig 3.7 (3.7a and 3.7c with 3.5a and 3.5d, and 3.7b and 3.7d with 3.5b and 3.5e respectively) reveals that they bear significant spatial similarities. The amplitude of the response for the observed RWS is somewhat reduced compared to the model response, whereas for the eddy forcing it is somewhat enhanced, but still comparable. This agreement indicates that there is a direct connection between tropical observed RWS and the model barotropic vorticity forcing and also between the extratropical observed eddy activity and the barotropic model forcing.

### 3.5.3 Tropical forcing: Zonal dependency

To assess whether there are preferred tropical regions that project stronger on the NAO, the model is forced at constrained longitudinal regions with the observed anomalous RWS. The selected forcing regions are those where the RWS shows maximum amplitude and significance (see Fig. 3.1). They are the East Atlantic, East Pacific/Caribbean, Middle Pacific and East Indian Ocean. The width of the tropical ( $0^\circ - 30^\circ N$ ) forcing window is  $40^\circ$ . Comparison of the response to local forcing in Fig. 3.8 with the hemispheric-wide tropical forcing in Fig. 3.5a and 3.5d shows that depending on the region of the forcing the excited patterns show differences, but overall the main structure for each case bears some resemblance to the pattern of the hemispheric-wide forcing.

As discussed in section 3.5.2, the sign of the response to the hemispheric-wide tropical forcing is opposite to the response of the total forcing, indicating that the hemispheric-wide tropical forcing tends to reduce the impact of the extratropical forcing. However, when the forcing is on a regional scale the sign of the response depends on the sign of the local

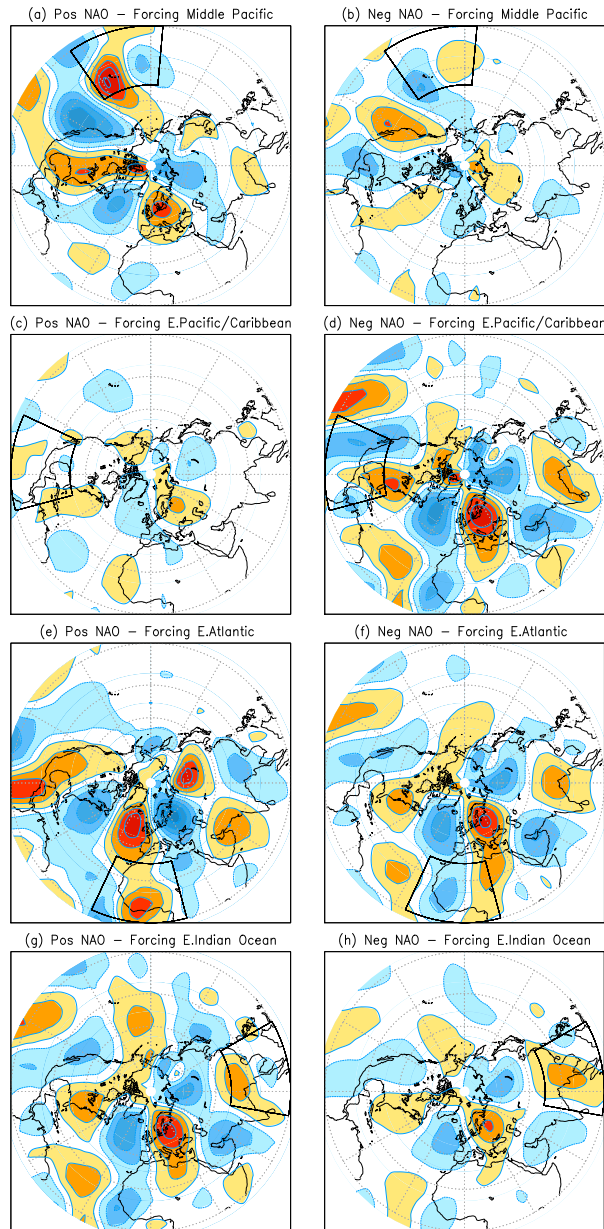


**Figure 3.8:** Meridional wind anomalies simulated by the barotropic model when forced with the observed RWS anomalies in the tropics ( $0^\circ - 30^\circ N$ ) in constrained regions of  $40^\circ$  longitude. Left column for the positive NAO phase and right column for the negative phase. The forced regions are indicated by a black box. The contour intervals are  $0.5 \text{ m s}^{-1}$  and negative values are indicated in blue colors.

	<i>Kinetic Wave Energy (<math>m^2/s^2</math>)</i>			
	Mid. Pacific	E. Pacific/Caribbean	E. Atlantic	E. Indian Ocean
Pos NAO	0.46	0.08	0.63	0.49
Neg NAO	0.16	0.63	0.42	0.19

**Table 3.2:** The kinetic wave energy anomaly as a response to forcing on the selected tropical regions for the positive and negative NAO phases.

forcing. An example for the positive NAO is the response to the local forcing over the East Pacific/Caribbean and over Eastern Atlantic (Fig. 3.8c and Fig. 3.8e). The response to these forcings is opposite, in agreement with the opposite sign of these forcings. The RWS forcing is negative over the East Pacific/Caribbean and positive over Eastern Atlantic (Fig. 3.1). The sign of response of the later agrees with that of the total NAO. We therefore conclude that areas that enhance the strength of the total NAO are those of negative RWS.

The amplitude of response, apart from the location of the source, depends linearly on the amplitude of the source itself. This is illustrated in Fig. 3.8c and 3.8d, where the forcing for the positive phase over the E.Pacific/Caribbean is rather weak, and in agreement with the response, contrarily to the negative phase where the forcing is rather strong. Cassou (2008) also notices that the two phases of the NAO respond to forcing on different locations in the tropics. Combination of both divergent and convergent vorticity forcing can interfere destructively and result in a response of smaller amplitude, as seen in Fig. 3.8h, compared to Fig. 3.8g. The absolute responses to the forcing of the selected tropical areas in terms of kinetic wave energy are listed in table 3.2.

There are non-linearities with respect to the sign and location of the forcing. The same areas forced with the opposite phase do not give exact mirroring patterns. Similar results concerning non-linearities with respect to the sign of the tropical forcing on the extratropical circulation have been noted by Kushnir and Lau (1992), Robinson et al (2003) and Li et al (2007).

## 3.6 Summary and Conclusions

In this chapter we investigated the contribution of tropical and extratropical forcing on the formation of the different phases of the NAO pattern.

While many previous studies on this subject focused on interannual and longer term variability (Thompson et al (2003), Hurrell et al (2004), Li et al (2007)), we focus on the relatively short 10–60 day time scale. That is, we are interested in the actual NAO events, rather than the stationary wave response to remote and local forcing. This is motivated by the time scale of the development of an NAO event which is thought to be associated with triggering and propagation of Rossby waves from the tropics to the extratropics and with eddy activity in the midlatitude jet (Feldstein (2003), Franzke et al (2003)). Analysis of the NAO forcing in the tropics for timescales shorter than 10 days indicated that the tropics are rather insignificant for the NAO. Because a main focus was the tropical forcing of the NAO those frequencies are excluded. We checked that the NAO characteristics for the 10–60 timescale were not very different from those of the 1–10 day timescale.

We use a barotropic model to diagnose the contribution of local and remote forcing to the formation of NAO events. The barotropic model allows us to study the contribution of estimates of the observed vorticity forcing in the atmosphere directly. The model also allows us to compute the anomalous forcing associated with the NAO inversely. This approach is more direct than prescribing anomalous SST conditions or idealized diabatic heating patterns in a general circulation model.

We made composites of the NAO to characterize the atmospheric flow and computed the vorticity forcing terms using atmospheric reanalysis data filtered between 10–60 days. The positive phase of the NAO is associated with a northward shift and southwest-northeast tilt of the midlatitude jet and the negative NAO with a zonally oriented jet. The meridional velocity anomalies at 300 hPa show a clear wave train. The vorticity forcing shows distinct patterns of opposite sign for both NAO phases. It is encouraging that the inversely determined forcing bears resemblance with estimates of the vorticity forcing from reanalysis data. This indicates that the barotropic model can be used to diagnose the impact of local and remote forcing. Note that exact comparison is not possible. For instance choices had to be made as to which levels to consider when computing forcing from reanalysis data.

By applying vorticity forcing in the barotropic model associated with both phases of the NAO for the extratropics and tropics respectively and comparing the results with a simulation with the total forcing we could quantify the impact of different regions. 14% of the meridional velocity variance at 300 hPa in the positive NAO phase could be generated

by tropical forcing only. This number increases to 35% for the negative NAO phase, consistent with a relatively larger tropical vorticity forcing compared to the extratropical forcing. The patterns resemble those of Peterson et al (2002) who focused on the stationary wave response. An important result is that the average tropical forcing appears to reduce the amplitude of the existing meridional wind anomaly pattern that is associated with the NAO. This is confirmed by a lead-lag correlation analysis showing that the NAO precedes the tropical forcing by two days. A physical mechanism for such a response is yet unclear. Analysis of forcing from distinct regions in the tropics shows that both strengthening and damping can be found. When evaluating the impact of extratropical forcing some care must be taken because of the non-linear interactions between the NAO and the eddy momentum fluxes.

These results indicate a pronounced impact of tropical forcing on the NAO. The impact of tropical variability on the NAO has been evaluated in many studies before, but focused mostly on seasonal or longer time scales associated with changes in low frequency behavior of the NAO. Here we focus on actual NAO events and on time scales relevant for the atmospheric dynamics to set up the teleconnections. The results may imply that events such as the Madden-Julian Oscillation can contribute to the forcing of the NAO. Some studies have pointed in this direction as well (e.g. Cassou (2008)). This chapter shows that there is a damping feedback of the tropical circulation to the NAO patterns that is generated in the extratropics.

#### *Acknowledgments.*

The authors thank Frank Selten and Will de Ruijter for the motivation and the helpful discussions. This work is part of the INATEX research program, which is financed by the Netherlands Organization for Scientific Research (NWO). We also thank the two anonymous reviewers that provided valuable suggestions and remarks that improved the outcome of this work.





---

# CHAPTER 4

---

## An evaluation of the EC-Earth climatology in the Indian Ocean

### **Abstract**

Changes in the Indian Ocean basin potentially affect climate variations worldwide through atmospheric and oceanic pathways. Aspects of these connections are studied with the global coupled climate model EC-Earth in the next chapter. In this chapter we evaluate the ability of EC-Earth to reproduce the observed climatology in the Indian Ocean basin. We examine the latter 40 years of a 250 year coupled simulation under constant year 2000 forcing conditions. The 40 year mean model data is compared with observations to assess the quality of the simulated seasonal cycle and the Indian monsoon structure. The general spatial distribution of the wind, precipitation and sea-surface temperature is simulated realistically throughout the year, although considerable biases remain. The largest discrepancies are found in the depth of the thermocline with a reversal of the east-west gradient at the equator.

## 4.1 Introduction

Numerical climate models are mathematical representations of the physical processes of the climate system. Over the years the models have improved in level of complexity and resolution and are now able to simulate in considerable detail the physics of the atmosphere and oceans, as well as of the cryosphere, the land surface and vegetation and of the green house gases. The weather predictions nowadays are more reliable than before, the seasonal forecasts more skillful and the long-range climate projections suffer less from climate drift. Nature and societies depend a great deal on the weather phenomena and are vulnerable to climate changes. Therefore the improvement of the climate models is crucial for both the everyday life and the long-range adaptation and mitigation planning.

The state-of-the-art Earth-system model EC-Earth was built by a consortium of scientists from 10 European countries with the final objective to achieve seamless predictions from scales of days to centuries, building the gap between weather and climate. The fully coupled Atmosphere-Ocean-Land-Sea Ice and Atmospheric Chemistry EC-Earth model is based on the Integrated Forecast System of the European Center of Medium-Range Weather Forecast (ECMWF) and it is now used for seasonal to decadal climate predictions and climate projections. It consists of a state-of-the-art atmospheric general circulation model coupled to an ocean general circulation model, a sea-ice model, a land surface model and an atmospheric chemistry model. The atmospheric component has a spectral resolution of T159 (about  $1.125 \times 1.125$  degree) and the ocean resolution is  $1 \times 1$  degree with a refined resolution near the equator.

The general performance of EC-Earth V2.2 has been evaluated (Hazeleger et al (2012)) and it was concluded that the large scale characteristics of the ocean, the atmosphere and the cryosphere, as well as the basic patterns of interannual climate variability are well represented, but considerable biases remain. Important patterns of variability, such as ENSO, are very well simulated. On the other hand, the oceans in general are too cold in part due to a too strong radiative cooling effect by clouds (Lacagnina and Selten (2013)). The hydrological cycle is found to be somewhat enhanced. Generally, it is found that the magnitude of the climatological errors of EC-Earth is comparable to other coupled models of similar complexity and resolution.

Among others, a realistic simulation of the SST distribution in the tropical oceans is important, as this influences not only the weather sys-

tems locally, but also affects the global weather through teleconnection patterns. In recent years the interest on the tropical Indian Ocean (IO) is growing as the evidence that its variability substantially influences remote regions increases (Schott et al (2009)). It has been found that variations in the temperature of the IO force changes in the atmosphere locally that lead to changes elsewhere on the globe through the excitation of Rossby waves (Hoerling et al (2004)). The IO has a strong impact on African and Australian rainfall (e.g. Reason (2002), Feng and Meyers (2003)), and it can influence the state of the NAO (Lu et al (2004)). Under particular conditions IO variability can even trigger an ENSO (Saji and Yamagata (2003b)). Furthermore, the IO basin has seen a steady increase in sea surface temperature since the 1950s (Du and Xie (2008)). Therefore, the tropical IO variability is important and its role in the climate system needs to be analyzed further (Yang et al (2009), Xie et al (2002b), Luffman et al (2009)).

The aim of this chapter is to evaluate the IO climatology in EC-Earth in more detail. It serves as a motivation to use coupled EC-Earth simulations in dedicated sensitivity experiments in the next chapter to investigate the response of the coupled system to a shallow thermocline event in the South-Western IO, the Seychelles Dome region.

For the evaluation multiple observational and reanalysis data sets are used and compared with 40 years of a control run from EC-Earth in terms of monthly means for winter and summer, as well as the seasonal cycle of the monsoon precipitation.

This chapter is organized as follows. In section 4.2 the reanalysis and observational data used for the evaluation are presented. In section 4.3 the performance of EC-Earth in boreal winter is assessed and in section 4.4 the performance in boreal summer. An evaluation of the monsoon cycle, the variability of the IO SSTs and the structure of the IO oceanic thermocline follows in section 4.5. Finally, section 4.6 concludes this chapter with a summary of the evaluation.

## 4.2 Data

The latter 40 years of a 250 year coupled control-run simulation under constant year 2000 forcing conditions of the coupled EC-Earth model are compared and validated in terms of monthly means with the following observational and reanalysis datasets.

The ECMWF 40 year reanalysis (ERA-40, Uppala et al (2005)) dataset for the period 01/1961 to 12/2000 are used. The ERA-40 dataset is the result of a three dimensional variational data-assimilation technique, using the T159L60 version of the Integrated Forecasting System to produce an analysis of the atmospheric state every six hours, using all available operational weather observations including satellite products.

Another dataset used is the Tropical Rainfall Measure Mission (TRMM, Kummerow et al (2000)). The TRMM data are provided by space-borne rain radar and microwave radiometric data and processed to deliver a precipitation product on a global  $0.25^{\circ} \times 0.25^{\circ}$  grid for the years 1998-2008.

The CPC Merged Analysis of Precipitation (CMAP - Xie-Arkin) data are also used. They provide monthly analysis of global precipitation in which observations from rain gauges are merged with precipitation estimates from satellite-based algorithms. The resolution is  $2.5^{\circ}$  (Xie and Arkin (1997)) and the period that is used for this study are monthly means for 1979-1999.

Also included in this validation chapter are the NCEP/NCAR Reanalysis data (Kalnay et al (1996)), for the period 01/1962-12/2001. NCEP/NCAR is using an analysis/forecast system to perform data assimilation using past weather observational data from 1948 to the present, and the analysis has a horizontal resolution of T62 (about 210 km). The reason for including another reanalysis dataset is to get an impression of the observational and analysis uncertainty.

Finally, for the evaluation of the ocean model the Simple Oceanographic Data Assimilation (SODA, Carton et al (2000a), Carton et al (2000b)) reanalysis data are used, for the period 01/1961-12/1990. The SODA data are created by a data-assimilation system using temperature and salinity observations and the analysis has a spatial resolution of  $0.5^{\circ} \times 0.5^{\circ}$  at 40 depth levels.

For the comparison, eight variables are selected (surface wind vectors, windstress, total precipitation, sea surface temperature, mean sea level pressure, vertical pressure velocity at 500hPa, divergence at 850 and 200hPa and the depth of the 20 degree isotherm in the ocean). The monthly climatological means of EC-Earth are calculated from 6-hourly data, and the months of January and July are compared to the observations.

## 4.3 Boreal Winter Evaluation

### 4.3.1 Surface wind and windstress

In Fig. 4.1 the surface wind stress and the wind at 10m height from EC-Earth are compared with the ERA-40 reanalysis data for the month of January. The large-scale structure is well simulated. The north-easterly winter monsoon winds along the shore of Somalia meet the south-easterly trade winds just south of the equator and feed the prevailing climatological westerly winds between the equator and  $10^{\circ}\text{S}$ . The Intertropical Convergence Zone (ITCZ, indicated by the purple colors) is located around  $5 - 10^{\circ}\text{S}$  and feeds the rising branch of the Hadley circulation (Okajima et al (2003)). Some discrepancies are present in the amplitude of wind stress, that is about 10% stronger in EC-Earth over the entire basin. The largest differences are found along the Somali jet area and the southeastern IO, in the trade winds region.

There are numerous ways to estimate the position of the ITCZ (Guijun and Chidong (2001), Zangvil and Yanai (1980), Hayashi (1982), Charney (1971)). Here we define it as the latitude where the meridional winds take values close to zero. The ITCZ location is plotted in a purple color in the wind vector plots in Fig. 4.1 and it is seen that both reanalysis and EC-Earth are in good agreement. The ITCZ follows closely the north-south migration of maximum incoming solar radiation, therefore during boreal winter it is positioned just south of the equator, between  $5^{\circ}\text{S}$  and  $10^{\circ}\text{S}$ .

### 4.3.2 Precipitation and SSTs

During winter the cold and dry north-westerly monsoonal winds blow off the Asian continent and cool the Northern IO, especially the Northern Arabian Sea, by strong latent and sensible heat fluxes (not shown), leading to minimum SST values in the North-West IO (Fig. 4.2). Overall in the IO basin SSTs appear 1 – 2 degrees colder in the model than in observations, possibly related to the stronger winds and the in general colder tropical SST's due to a too strong cloud radiative cooling (Lacagnina and Selten (2013)). In the Southern Oceans, EC-Earth suffers from a warm bias that is common to many climate models (Fig. 9.14 Stocker et al (2013)). Warmer SST's are found off the coast of Australia where the lack of stratocumulus clouds (Lacagnina and Selten (2013)) leads to a surplus of solar radiation warming the ocean surface. Overall, the precipitation structure, largely reflecting the position of the ITCZ in January, is

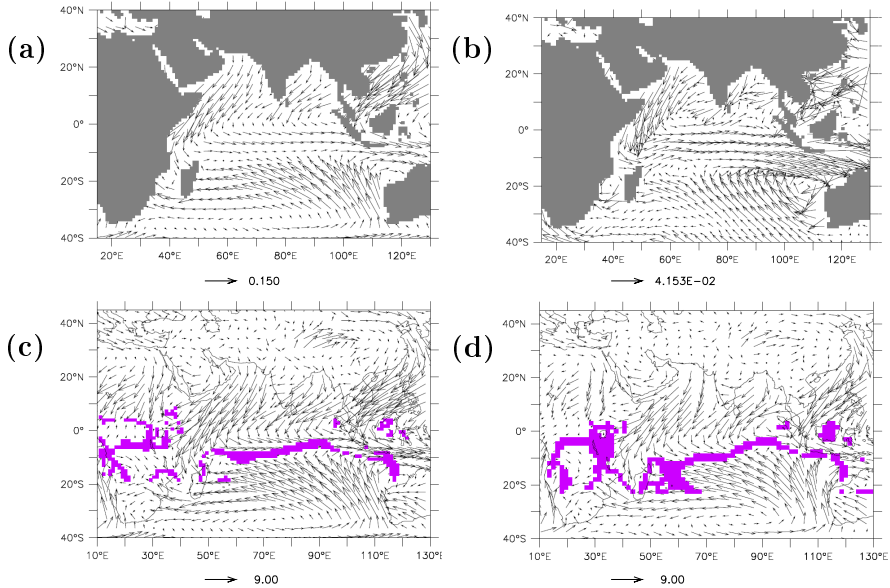


**Figure 4.1:** (a) January mean windstress of EC-Earth ( $Nm^{-2}$ ) averaged over 40 years of simulation. (b) The differences in the wind stress between EC-Earth and ERA-40 reanalysis data for the same month (EC-Earth - ERA40). (c) The mean wind vectors at 10m for January in EC-Earth and (d) in ERA-40. The purple scattered dots in (c) and (d) show the latitude where the absolute meridional wind is less than  $0.3ms^{-1}$ , as an indication for the position of the ITCZ. The units for the wind are  $ms^{-1}$ .

well reproduced (Fig. 4.3). The major deficiency is stronger precipitation in the west, in line with the SST biases and weaker in the east. Over the Indonesian region, precipitation is stronger over ocean, but weaker over land. Over Africa the ITCZ seems displaced too far to the south.

Precipitation is a highly complex process in the atmosphere. Biases in this simulated field often indicate deficiencies in the representation of the various physical processes involved, such as cloud microphysics, cumulus convection, planetary boundary layer processes and large scale circulation processes (Dai (2006)). Also precipitation is hard to observe due to its variable character at short spatial and temporal scales. To have an indication of the observational error, we employed three different datasets (ERA-40, TRMM and CMAP). Model errors with respect to ERA-40 and CMAP agree to a large extent, both in patterns and in magnitude, whereas the EC-Earth precipitation seems to be in closer agreement with

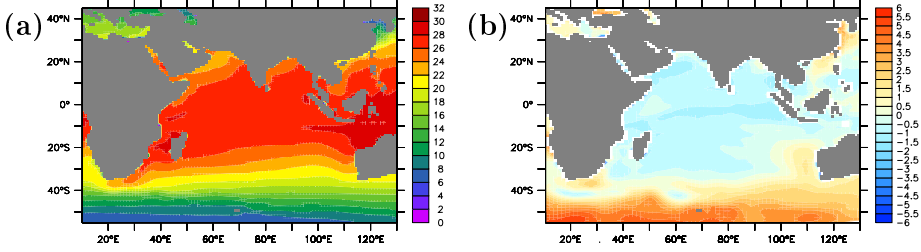


**Figure 4.2:** The January mean SSTs in  $^{\circ}\text{C}$  from EC-Earth in (a), and in (b) the differences between the model and ERA-40 reanalysis.

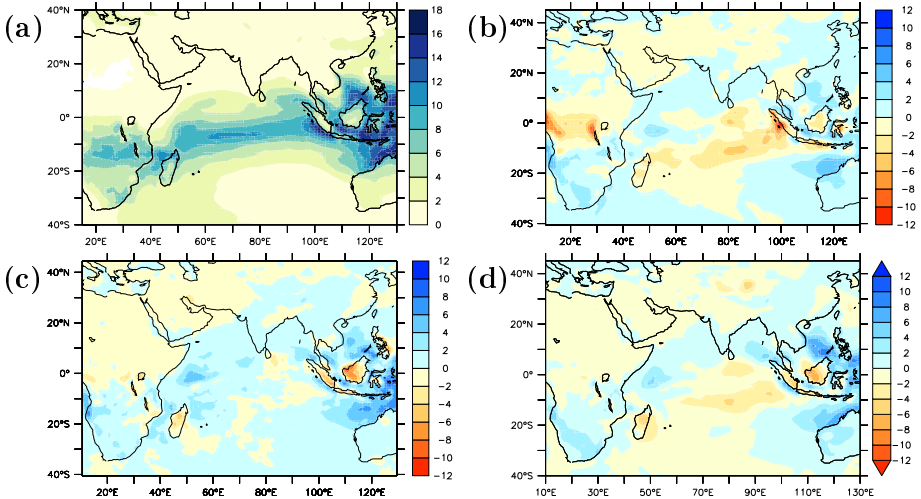


**Figure 4.3:** The mean total precipitation for January in  $\text{mmday}^{-1}$ . In (a) the actual precipitation field from EC-Earth. The differences in (b) between EC-Earth and ERA-40 reanalysis, in (c) between EC-Earth and TRMM observations and in (d) between EC-Earth and CMAP data.

the TRMM data. Note that the TRMM data we used comprises only 10 years so differences are to some extent due to decadal variability. With respect to all datasets, EC-Earth simulates too much precipitation in the western equatorial region and too less in the eastern part of the basin and over the tropical landmasses. The precipitation is overestimated off the coast of Australia where the SSTs are too high, as well as over Southern Africa and the Pacific warm pool.

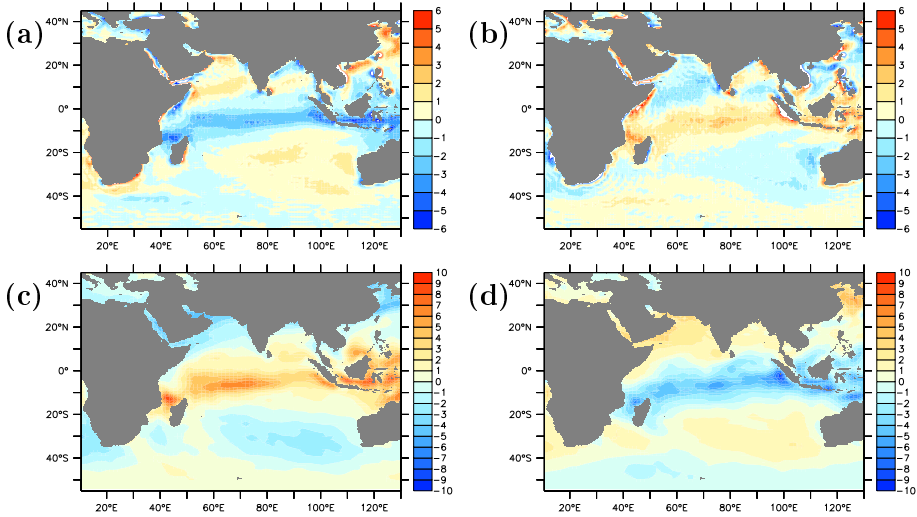


**Figure 4.4:** The mean divergence at 850hPa for January for EC-Earth in (a). The differences between the model and ERA-40 in (b). Similar, in (c) and (d) for the 200hPa level. The units are in  $10^{-6} s^{-1}$ .

### 4.3.3 Atmospheric circulation

An assessment of the large scale convergence and divergence of air masses by analyzing the divergence field at 850 and 200hPa (Fig.4.4) reveals that, as expected, largest low-level convergence and upper level-divergence is found in the region of the ITCZ. In general both the low-level convergence as well as the upper-level divergence is underestimated. At first sight, one would expect reduced vertical motions on the basis of these differences, but this is not the case when we assess the pressure velocity errors at 500hPa as these depend on the integral of the divergence error from the surface to the 500hPa level.

The pressure velocity in the mid-troposphere at 500hPa (Fig. 4.5a) indicates rising motions in the region of the ITCZ where we found low-level convergence and upper-level divergence. Although EC-Earth simulates weaker low-level convergence and upper-level divergence in the ITCZ region, the pressure velocity errors have a more complicated structure, both with respect to the ERA-40 and NCEP/NCAR reanalysis data, with reduced rising motions over the equatorial landmasses and in the eastern part of the basin, and stronger rising motions in the west and central equatorial region and the Pacific warm pool. These errors in the pres-



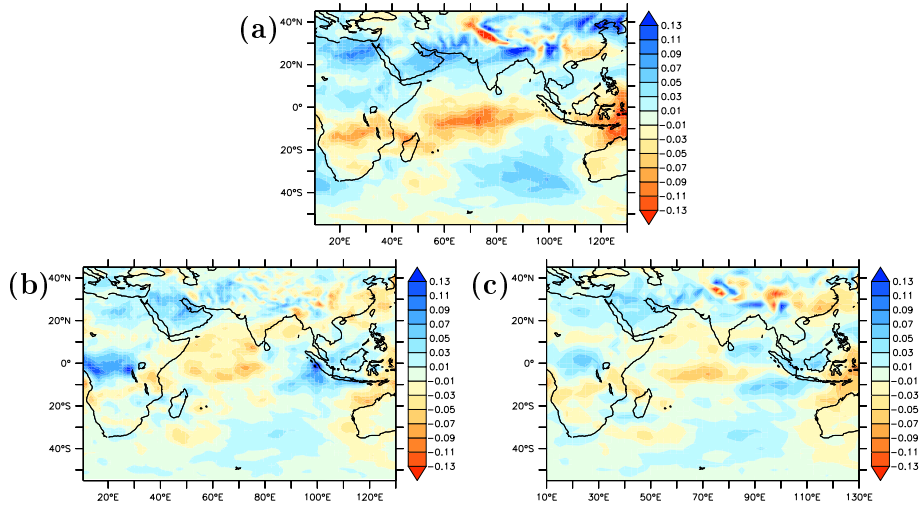


**Figure 4.5:** January mean 500hPa vertical pressure velocity for EC-Earth in (a). The differences between the model and ERA-40 in (b) and between the model and NCEP-NCAR reanalysis in (c). Units are in  $\text{Pa s}^{-1}$  and positive values represent subsidence.

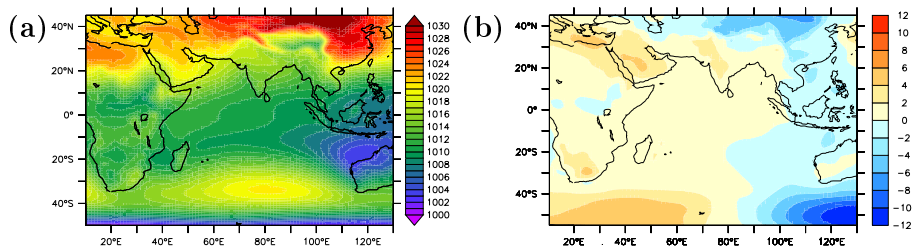


**Figure 4.6:** The mean sea level pressure in January for EC-Earth in (a), and in (b) the differences from ERA-40. The units are in  $\text{hPa}$ .

sure velocity in the mid-troposphere are consistent with the errors in the simulated rainfall as discussed above.

The spatial structure of the Mean Sea Level Pressure (MSLP) distribution for January is well simulated (Fig. 4.6). The major difference is found in the South-East IO where there is a low pressure error. This error is consistent with the higher SSTs (Fig. 4.2), the increased precipitation (Fig. 4.3) and the stronger south-easterly winds (Fig. 4.1) in the region.

### 4.3.4 Depth of the 20 degrees

To conclude the model comparison for January, the depth of 20 degrees isotherm (D20) is analyzed and is plotted in Fig. 4.7. D20 is a good approximation of the depth of the ocean thermocline as it is a typical mid-thermocline isotherm in the tropical ocean (Bollasina and Nigam (2008), Schott et al (2009)). The region with strongest downwelling and hence the area with the deepest thermocline is located along the band of  $15^{\circ}S-25^{\circ}S$ , starting off Eastern Madagascar to the North-Western Australia and is associated with the South Equatorial Current (Masumoto and Meyers (1998)). A secondary maximum in January is located in the Arabian Sea, where the winter monsoonal winds cause strong Ekman downwelling. The minimum depth is found throughout the year in the South-Western IO over the Seychelles region. Because of the shallow thermocline the region is also referred to as the Seychelles Dome. The shallow thermocline is attributed to a negative windstress curl and to the arrival of oceanic Rossby waves from the South-Eastern IO (Yokoi et al (2008), Tozuka et al (2010), Hermes and Reason (2008)).

The spatial structure of the thermocline depth is quite well simulated by the model. The Seychelles dome is clearly visible as an area of shallow thermocline depth north-east of Madagascar. The model simulated thermocline is too deep in most parts of the IO. In some areas, such as in the Arabian sea and off the west coast of Australia it is more than 50 m too deep. At the equator, off the coast of Indonesia, the thermocline is up to 50 meter too deep, causing a reversal of the equatorial tilt of the thermocline (Fig. 4.7c). The simulation errors in D20 are due not only to biases in SSTs and wind stress, but also due to the errors in ocean currents and vertical mixing processes. Especially these latter processes are hard to model in a relatively coarse resolution ocean model.

## 4.4 Boreal Summer Evaluation

In summer, the temperature gradient between continent and ocean reverses sign due to the increase in solar radiation in the northern hemisphere and the differences in the specific heat capacity between land and sea. The land-sea pressure gradient follows this change and forces the winds to reverse direction and form the summer monsoon flow. The SSTs warm up in the northern hemisphere, following the sun and the ITCZ migrates northward and reaches maximum values, enhanced by the moist

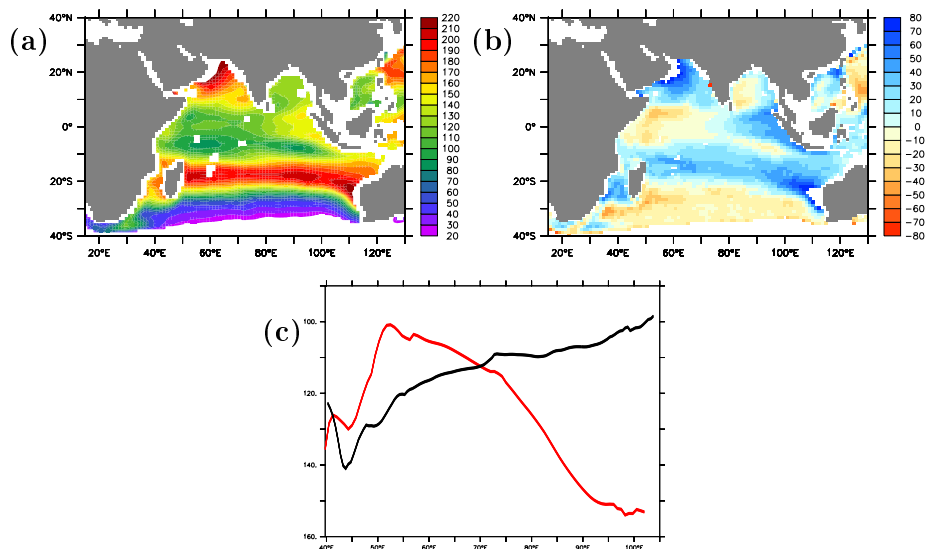


**Figure 4.7:** The January mean depth of the 20 degrees isotherm from EC-Earth in (a), and in (b) the difference with respect to the SODA reanalysis. The units are in meters. In (c) is the depth of the 20 degrees isotherm averaged between  $5^{\circ}S - 5^{\circ}N$ . The red line represents the EC-Earth data and the black line the SODA reanalysis.

ocean air being lifted while propagating northwards into the land (Schott and McCreary (2001), Schott et al (2009)).

#### 4.4.1 Surface wind and windstress

In July, the south-easterly trade winds of the southern hemisphere have crossed the equator and feed the strong winds in the west of the basin, also referred to as the Somali jet. Strong onshore winds occur as well over the Bay of Bengal. The ITCZ has moved over land as part of the Indian monsoon.

The mean July wind field over the Indian Ocean is quite realistically simulated (Fig. 4.8). In contrast to the January mean winds (Fig. 4.1) the strength of the wind is generally underestimated. The onshore winds over the Arabian Sea, Bay of Bengal and South China Sea are all weaker as well as the south-easterly trade winds in the south-eastern part of the basin. The wind bias is smallest just south of the equator including the region of the Seychelles Dome.

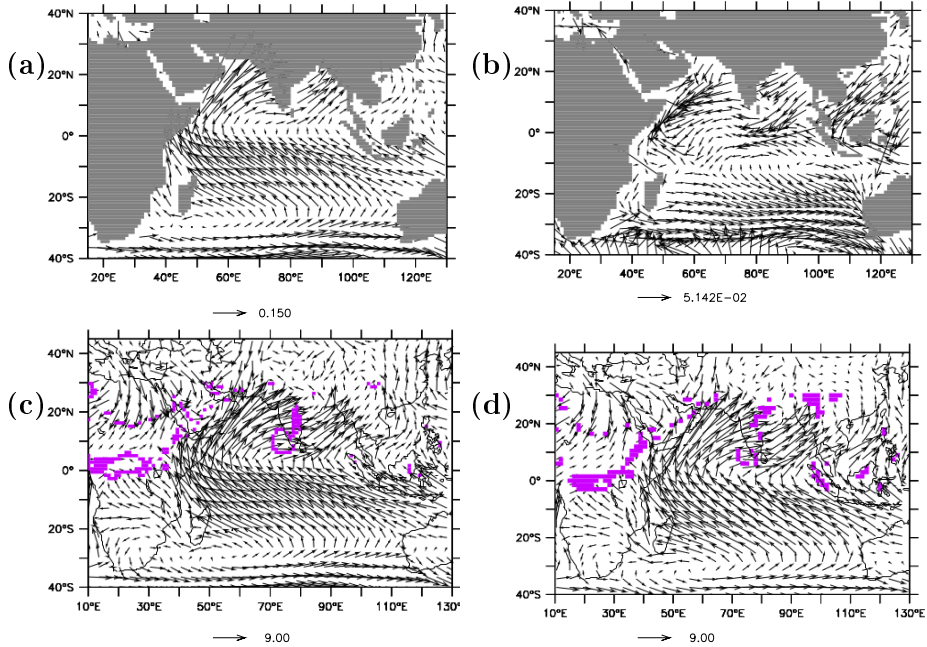


**Figure 4.8:** (a) The July mean windstress for EC-Earth ( $Nm^{-2}$ ) over the Indian Ocean for 40 years of simulations. (b) The differences between EC-Earth and the 40 years of ERA-40 reanalysis data for the same month. (c) The mean wind vectors at 10m for July for EC-Earth and in (d) for ERA-40. The purple scattered dots in (c) and (d) show the latitude were the absolute meridional wind is less than  $0.3ms^{-1}$ , as an indication for the position of the ITCZ. The units for the wind are  $ms^{-1}$

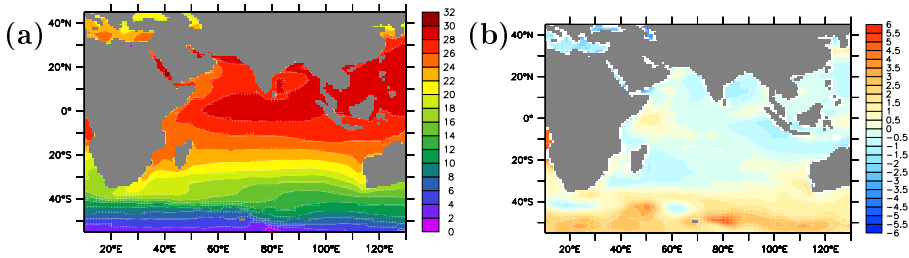


**Figure 4.9:** The July mean SSTs in  $^{\circ}C$  from EC-Earth in (a), and in (b) the differences between the model and ERA-40 reanalysis.

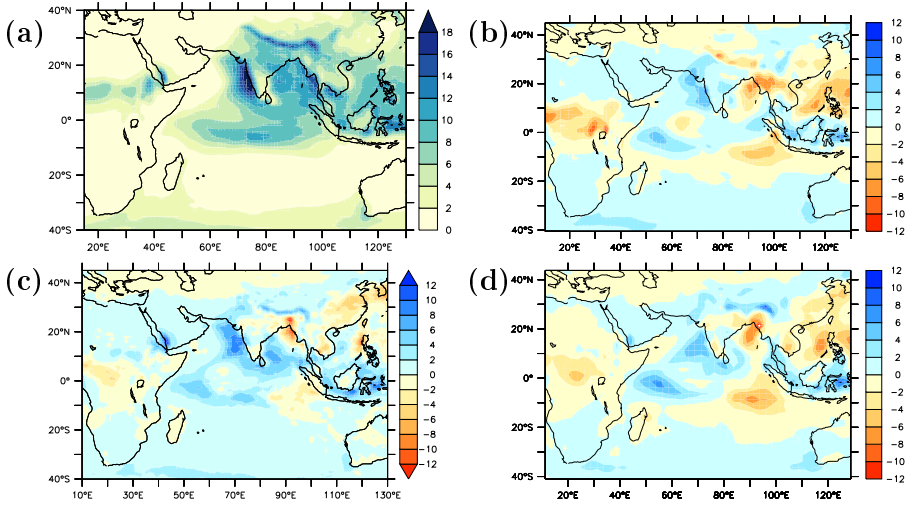


**Figure 4.10:** The mean total precipitation for July in  $\text{mmday}^{-1}$ . In (a) the actual precipitation field from EC-Earth. The differences in (b) between EC-Earth and ERA-40 reanalysis, in (c) between EC-Earth and TRMM observations and in (d) between EC-Earth and CMAP data.

#### 4.4.2 Precipitation and SSTs

Due to the northward shift of the ITCZ in summer, the strong convective regions are found in the belt between the Eastern Arabian Sea and South China Sea. These are also the regions with the highest SSTs (in addition to the equatorial region). The Asian summer monsoon is organized into several well-defined convection centers, all anchored by mountain ranges (Xie et al (2006)). Against the seasonal tendencies, a strong cooling in the western Arabian Sea occurs, that is due to Ekman upwelling near Somali and Omani coasts and due to latent heat loss caused by the strong southwesterly wind, named the Findlater jet (Schott et al (2009)). The colder SSTs weaken convective precipitation over these areas.

The SST cold bias is also present in July (Fig. 4.9) but is less severe as in January. The warm biases in the Southern Ocean and off the coast of Australia that we found in January are also present in July. At the equator, there is a warm bias in the west and a cold bias in the east. These errors are reflected in the precipitation bias with more precipitation over the warmer and less over the colder SSTs, as compared to all three precipitation datasets used (Fig. 4.10). As in January, precipitation over

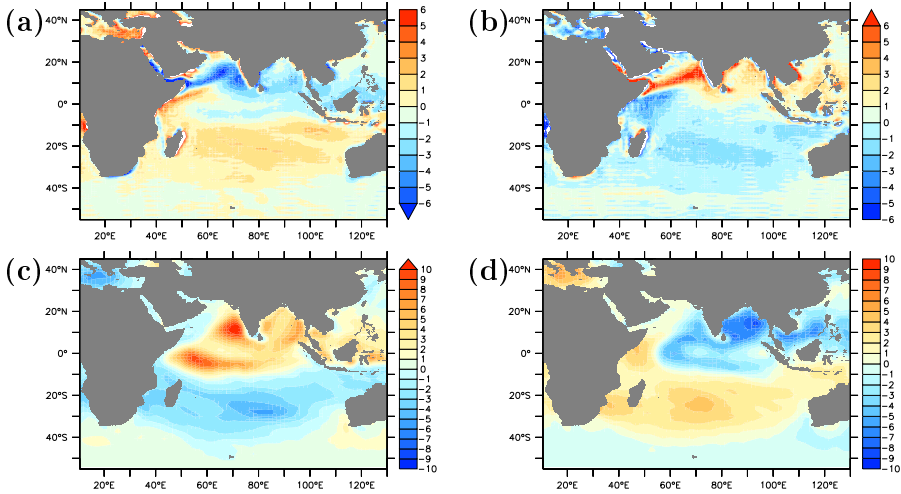


**Figure 4.11:** The mean divergence at 850hPa for July from EC-Earth in (a) and the differences between the model and ERA-40 in (b). Similar in (c) and (d) for the level of 200hPa. The units are in  $10^{-6} s^{-1}$ .

equatorial land masses is underestimated. In general, too much precipitation is simulated over the Southern Ocean in the region of the warm bias. Excessive rainfall is also found over the equatorial warm pool region and west of the Indian coast. Less rain is simulated over the Indian continent, the Bay of Bengal and South-East Asia, where the onshore monsoonal winds are weaker than observed.

#### 4.4.3 Atmospheric circulation

Regions of strong low-level convergence and upper-level divergence are simulated east and west of the Indian sub-continent and in the equatorial region (Fig. 4.11). These are the regions with strong vertical motions (Fig. 4.12). EC-Earth generally underestimates the strength of the low-level convergence and upper-level divergence in July as well. Vertical motions are stronger, however, off the west coast of India, the western equatorial region and the Pacific warm pool which correspond to regions with excessive rainfall. Over the Bay of Bengal and the equatorial land masses, vertical motions are weaker as is the rainfall.

A dominant feature in the MSLP in July is the thermal low over the continents bordering the Indian Ocean to the north (Fig. 4.13). The

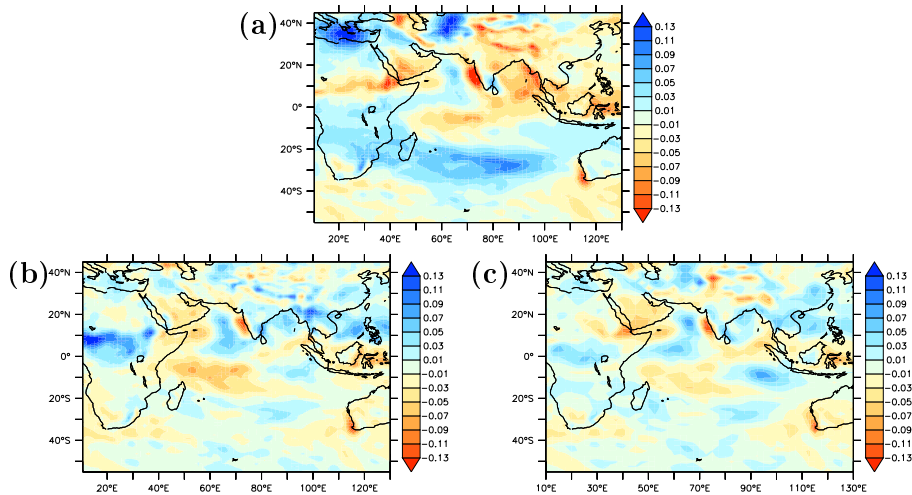


**Figure 4.12:** The July mean 500hPa Omega for EC-Earth in (a). The differences between the model and ERA-40 reanalysis in (b), and in (c) the differences between the model and NCEP/NCAR reanalysis. The units are in  $Pa s^{-1}$  and the positive values represent subsidence.

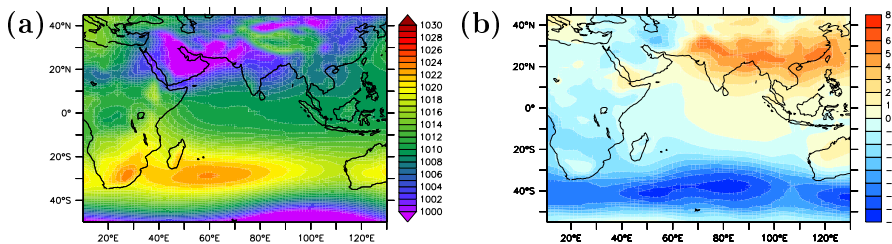


**Figure 4.13:** The mean sea level pressure in July for EC-Earth in (a) and the differences between model and ERA-40 in (b). The units are in  $hPa$ .

thermal low in EC-Earth is weaker, consistent with the weaker monsoonal flow. The warm Southern Ocean SST bias is consistent with a poleward shift of the subtropical high, visible as the high pressure bias over the Southern Ocean.

#### 4.4.4 Depth of the 20 degrees isotherm

Both the pattern of the thermocline depth as well as the error with respect to the SODA reanalysis in July (Fig. 4.14) is very similar to January

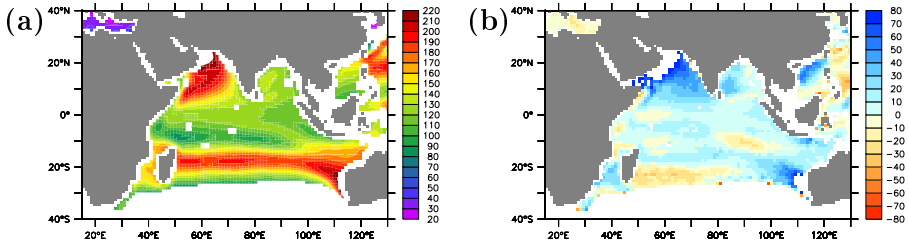


**Figure 4.14:** The July mean 20 degrees isotherm layer for EC-Earth in (a), and in (b) the anomalies between EC-Earth and SODA reanalysis. The units are in meters.

(Fig. 4.7) except that the depth errors are generally smaller. The shallow thermocline in the region of the Seychelles Dome is also clearly present in July and it is on average about 10 meters too deep.

## 4.5 Monsoon seasonal cycle, SST variability and Indian Ocean thermocline

To evaluate the seasonal evolution of the Indian monsoon, we analyzed the precipitation averaged over the longitudes  $70^{\circ}\text{E}$  and  $100^{\circ}\text{E}$  at each latitude from  $20^{\circ}\text{S}$  to  $40^{\circ}\text{N}$ , both for EC-Earth and TRMM data (Fig. 4.15). The seasonal meridional migration of the ITCZ is very similar, the onset of the monsoon starts a little earlier and is less abrupt and the total amount of precipitation at the peak of the monsoon season is underestimated.

To get an impression of the ability of EC-Earth to simulate interannual variations, we analyzed the standard deviation of SST separately for January and July (Fig.4.16) both for the 40 year EC-Earth simulation as well as for the SODA reanalysis. Largest interannual variations are found in both months in the Agulhas region south of Africa in the SODA reanalysis. EC-Earth, due to its coarse resolution, is not able to reproduce the large variations due to turbulent ocean eddies (Bjastoch et al (2009)). In general the variations are smaller in EC-Earth, but it does capture part of the large-scale distribution of the SST variations in the basin, with smallest variations in the north-east and largest variations in the central Southern Indian Ocean. The larger variations in the northern Arabian Sea in July are present, but smaller, and these are suggested to



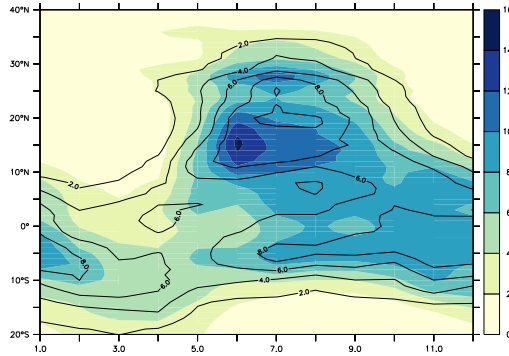


**Figure 4.15:** The seasonal cycle of the total precipitation zonally averaged over the Indian continent and surrounding ocean (between 70°E and 100°E). In shades are the TRMM observations and in contours the EC-Earth data. The zonal axis represents months from January to December and the units are in  $mmday^{-1}$ .

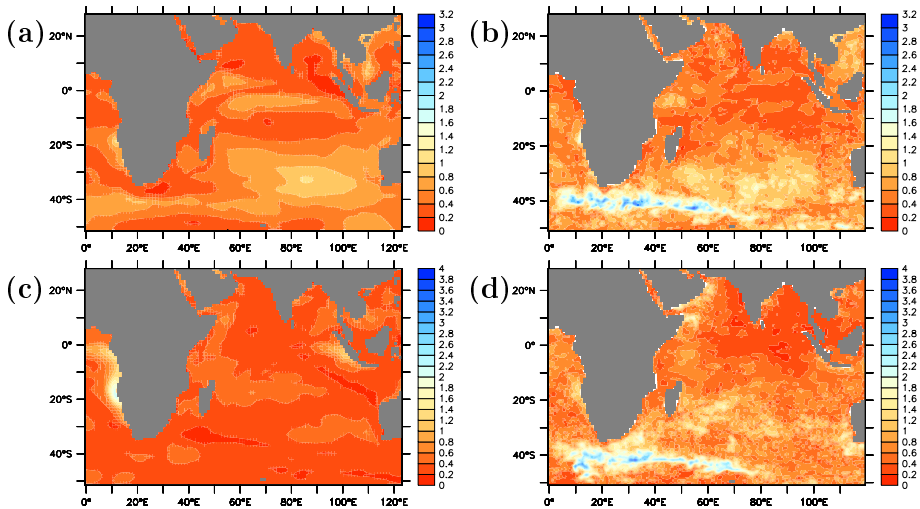


**Figure 4.16:** The 40-year annual mean standard deviation of SSTs for January, in (a) for EC-Earth and in (b) for SODA reanalysis. Same for July, in (c) for EC-Earth and in (d) for SODA reanalysis. The units are in  $^{\circ}C$ .

be related to variations in Ekman pumping (Behera et al (1999)).

To verify that also for EC-Earth the 20 degree isotherm lies within the thermocline, we analyzed the thermal structure averaged over the basin (Fig. 4.17). Indeed the 20 degree isotherm is close to the depth

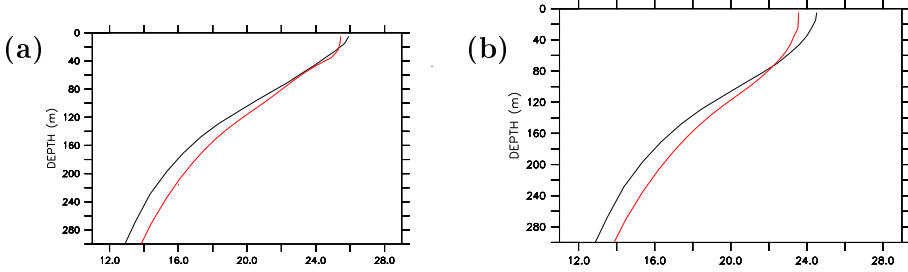


**Figure 4.17:** Thermocline structure in IO in monthly means. The red line represents the EC-Earth data and the black line the SODA reanalysis. The monthly means in (a) for January and in (b) for July. The zonal axis is temperature in  $^{\circ}\text{C}$ .

of maximum gradient in temperature, both for EC-Earth as well as for SODA. EC-Earth is cooler at surface and warmer at depth and has a more diffuse thermocline with a less steep gradient in temperature with depth. The thermocline is deeper in both months by about 10 meters. The seasonal cycle in the depth of the mixed layer is well simulated, with a deeper mixed layer in July and April and shallower in January and October (April and October are not shown). At depths deeper than 600 meters the model simulates again colder values than observed (not shown). The areas along the equator, Arabian Sea and Java area were examined more detailed (not shown). Larger biases appeared in the Arabian Sea due to a lack of sufficient upwelling of deeper, cold water. Near Java the bias is not as large as in Arabian Sea. The equatorial region is the most accurately simulated.

## 4.6 Summary and Conclusions

The quality of the EC-Earth simulation in the region of the Indian Ocean is assessed by evaluating the climatology of the final 40 years of a 250 year coupled control simulation under constant year 2000 forcing conditions. The monthly mean fields of the 10m wind, wind stress, precipitation, SST, MSLP, divergence at 850hPa and 200hPa, pressure velocity at 500hPa and the 20 degrees isotherm are examined and compared with observational dataset (ERA-40, TRMM, CMAP, NCEP/NCAR and SODA).

A general conclusion is that the main structure of these spatial fields is realistically simulated throughout the year, although considerable re-

gional biases are present. Most importantly for the sensitivity experiments conducted in the next chapter is that EC-Earth simulates a shallow thermocline in the region of the Seychelles dome throughout the year, that is somewhat deeper than in observations though.

SSTs are 1 to 2 degrees colder than observed over almost the entire basin, except in the Southern Ocean where EC-Earth has a warm bias. The warmer SSTs off the Australian coast are likely caused by an underestimation of the stratocumulus cloud cover over the cold ocean surface, an often observed bias in coupled climate models. In July, the warm SSTs at the equator extend further to the west compared to the observations. This bias is connected to the westward extension of the tropical rain belt and the westward displaced turning of the equatorial winds toward the Indian continent that is part of the Indian monsoon system. In January and July, precipitation is stronger in the western equatorial region and weaker in east.

With respect to the monsoon precipitation, the seasonal march is well captured, but the onset of the monsoon is smoother and starts earlier in the season and the total regional precipitation amount is underestimated. With respect to the regional distribution of monsoonal precipitation, EC-Earth simulates excessive rainfall west of the Indian subcontinent and too little to the east. The reversal of the flow over the Arabian Sea is well simulated, although in January the simulated flow is stronger, in July it is weaker.

To conclude, EC-Earth simulates reasonably the coupled atmosphere-ocean evolution in the Indian Ocean throughout the year and will be used in the next chapter to study the response of the coupled system to a shallow thermocline event in the Seychelles Dome region.



---

## CHAPTER 5

---

# The Ocean-Atmosphere response to wind-induced Thermocline changes in the tropical South Western Indian Ocean

Iris Manola, Frank Selten, Will De Ruijter and Wilco Hazeleger  
*submitted to Climate Dynamics*

### **Abstract**

In the Indian Ocean basin the SSTs are most sensitive to changes in the oceanic depth of the thermocline in the region of the Seychelles Dome. Observational studies have suggested that the strong SST variations in this region influence the atmospheric evolution around the basin, while its impact could extend far into the Pacific and the extra-tropics. Here we study the adjustments of the coupled atmosphere-ocean system to a winter shallow doming event using dedicated ensemble simulations with the state-of-the-art EC-Earth climate model. The doming creates an equatorial Kelvin wave and a pair of westward moving Rossby waves, leading to a warming of the SST 1 – 2 months later in the Western equatorial Indian Ocean. Atmospheric convection is strengthened and the Walker circulation responds with reduced convection over Indonesia and cooling of the SST in that region. The Pacific warm pool convection shifts eastward and an oceanic Kelvin wave is triggered at thermocline depth. The wave leads to an SST warming in the East equatorial Pacific 5 – 6 months after the initiation of the Seychelles Dome event. The atmosphere responds to this warming with weak anomalous atmospheric convection. The changes

in the upper tropospheric divergence in this sequence of events create large-scale Rossby waves that propagate away from the tropics along the atmospheric waveguides. We suggest to repeat these types of experiments with other models as the results might be model-dependent. We also suggest to create the doming event in June so that the East-Pacific warming occurs in November when the atmosphere is most sensitive to SST anomalies and El Niño could possibly be triggered by the doming event under suitable conditions.

## 5.1 Introduction

Oceanic regions with a shallow thermocline play a key role in the air-sea interaction. A shallow thermocline and a shallow mixed layer are sensitive to changes in the local wind stress, enhancing or suppressing the upwelling of cold waters from below leading to strong SST anomalies (Duvel et al (2004)). It provides a window for interaction between ocean and atmosphere as the tropical atmosphere is sensitive to SST changes and thermocline disturbances are easily created by windstress anomalies. Effects of this interaction can be remotely felt as atmospheric and oceanic waves move away from the region. A shallow thermocline region is found in the Western Indian Ocean (IO), along a narrow region just south of the equator, referred to as the Seychelles Dome (SD, Yokoi et al (2008)). The SD is characterized by a shallow thermocline that experiences large seasonal to interannual variability and strong seasonal upwelling. Generally, the Indian Ocean (IO) is known to exhibit a large impact on climate variability (Hoerling et al (2004), Schott et al (2009), Luffman et al (2009), Yang et al (2009)). More specifically, a lot of attention has been devoted recently to the SD region, as it is the region where the SSTs are most sensitive to changes of the thermocline and that in turn can influence the climate system around the Indian Ocean and possibly beyond.

Previous studies have documented the impact of the SD region on precipitation over Eastern Africa (Goddard and Graham (1999)) and Asia (Vecchi and Harrison (2004)). The SD region has been mentioned as a possible predictor for the Indian Monsoon season (Izumo et al (2008)), as it influences the timing of its initiation (Annamalai et al (2005a)). In addition SD variability affects IO cyclogenesis for several reasons. First, the SST variations in the SD region are large and impact the atmospheric stability and second, the SD thermocline is most shallow between December and June which coincides with the South-Western Indian Ocean cyclone season (Xie et al (2002a), Hermes and Reason (2008)). Finally, changes in the SD area may also impact the Madden Julian Oscillation (MJO) (Vialard et al (2008), Vialard et al (2009), Schott et al (2009)).

The shallow thermocline is maintained by both local and remote forcings (Yokoi et al (2008), Hermes and Reason (2008), Tozuka et al (2010), Lloyd and Vecchi (2010), Jayakumar et al (2011), Trenary and Han (2012)). Locally the upwelling is attributed to Ekman pumping due to the cyclonic wind stress curl in the convergence region of the south-easterly trade winds and the north-westerly monsoonal winds (Murtugudde and Busalacchi

(1999), Hermes and Reason (2008), Trenary and Han (2012)). Remotely, the doming region is influenced by the arrival of upwelling or downwelling Rossby waves that emanate from the Eastern IO and owe their existence to thermocline anomalies over the Eastern IO or are forced by wind stress curl in the open Pacific ocean (Rao and Behera (2005)). It is suggested that the remote Rossby wave forcing mostly attributes to the doming between January and July, while for the remainder local wind stress forcing is dominant (Trenary and Han (2012)). The Indonesian Throughflow (ITF) can also play a role in the forcing of the SD (Zhou et al (2008)). It is noted that a shallower Dome should be expected in case of an ITF shut down (Yokoi et al (2008)).

The SD variations co-vary with both the Indian Ocean Dipole (IOD) and the El Niño - Southern Oscillation (ENSO) (Jochum and Murtugudde (2005), Annamalai et al (2005b), Annamalai et al (2007)). The relation with the IOD explains why shallow SD events are more pronounced in boreal winter. A shallow doming is enhanced by a negative IOD event, as the latter is associated with cold SST anomalies over the Western IO and wind stress anomalies that lead to Ekman upwelling and shallowing of the thermocline over the region. The positive SST anomalies over the Eastern IO basin during the negative IOD event and the associated wind stress anomalies lead to local Ekman downwelling that excites a westward propagating Rossby wave. The wave arrives in the SD region about 4 – 6 months later and further raises the thermocline. A similar mechanism enhances the doming during La Niña conditions. Observational studies indicate that the SD is stronger linked to the IOD than to ENSO. The IOD leads the peak of the doming by 2 – 4 months, whereas La Niña leads the doming by 1 – 3 months. (Tozuka et al (2010), Trenary and Han (2012)).

The doming region is easily identified as a region with minimum depth of the 20 degrees isotherm (D20, Fig. 5.1a). D20 is an appropriate level to study the distribution of the ocean thermocline in the tropics. Within the IO basin the region where the thermocline is shallowest due to strongest mean upwelling is the SD area (marked by the black rectangle). This is also the region of strongest coupling between thermocline depth variations and SST as witnessed by the high correlation between monthly anomalies of D20 and local SSTs (Fig. 5.1b, see also Xie et al (2002a) and Annamalai et al (2005a)). This strong thermocline-SST connection, in combination with the SD region being close to the equator, where the atmosphere is sensitive to SST changes, indicates that the SD region is potentially a key



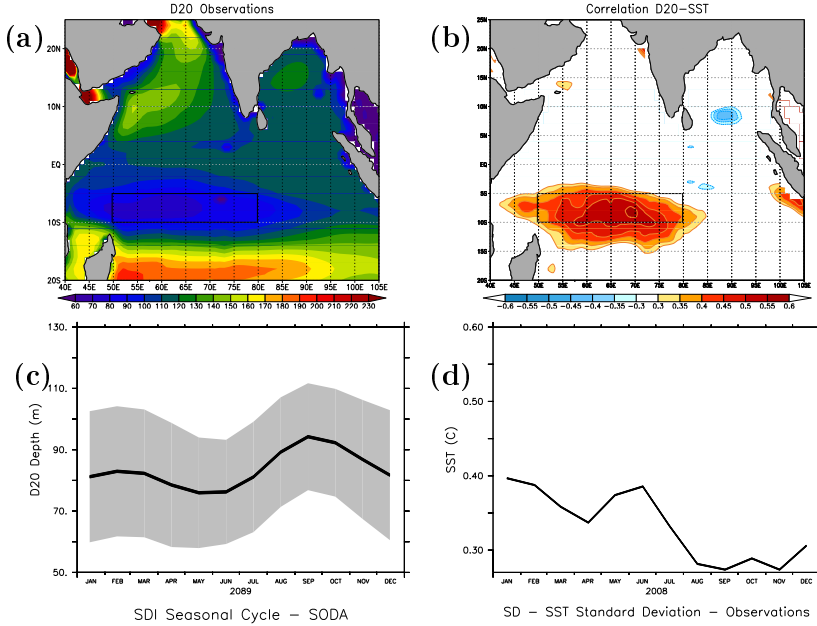


**Figure 5.1:** Observations of the depth of the  $20^{\circ}\text{C}$  isotherm (D20) from SODA reanalysis and of the SSTs from HadISST for the years 1979 – 2008. (a) The averaged depth of the  $20^{\circ}\text{C}$  isotherm. The depth is measured in meters. (b) The point to point correlations of the depth of monthly D20 anomalies with SST anomalies during the same years. The data are detrended. The black rectangular box indicates the Seychelles Dome region. (c) The seasonal cycle of the SDI index for the 47 years of the SODA reanalysis. The gray shaded area represents one standard deviation of the interannual variations. The SDI index is the D20 anomaly averaged over the SD region expressed in meters. (d) The standard deviation of interannual monthly mean SST anomalies for each month of the year. The units are in  $^{\circ}\text{C}$ .

region for ocean-atmosphere interaction in the IO and variations in the tropical circulation.

In order to determine the season in which shallow events with strong impacts on the coupled system occur most likely, we assessed the mean seasonal cycle of the depth of the SD thermocline, as well as the mean seasonal cycle of interannual SST variability. We define the Seychelles Dome Index (SDI) as the depth of the 20 degrees isotherm averaged over the area  $50^{\circ}\text{E} - 80^{\circ}\text{E}$  and  $5^{\circ}\text{S} - 10^{\circ}\text{S}$  and its seasonal cycle is plotted in Fig. 5.1c. The biennial character of the SDI is apparent, as has been

noted previously by Hermes and Reason (2008), Yokoi et al (2008) and Tozuka et al (2010), with a first minimum in January, a second in June and maxima in spring and autumn. It should be noted that the exact boundaries of the SD region slightly vary in the different studies, without significant influence in the seasonal cycle. The standard deviation of the SDI is quite large year-round (indicated by the shaded area), with a maximum in January. The seasonal cycle of the interannual variations in the area averaged monthly SST anomalies over the Dome region (Fig. 5.1d) also has a biennial character that is linked to the doming, with largest variations taking place in January and a secondary maximum in June.

The literature studies so far concentrate predominantly on the variability of the SD and on the phenomena determining this variability. There has been some effort to investigate how variations in the SD region feed back on the atmosphere and ocean (Xie et al (2002a), Annamalai et al (2005a), Lloyd and Vecchi (2010), Swapna et al (2013)) but a complete study about the effects of a shallow SD thermocline event on the coupled system locally and remotely is still lacking.

Here we investigate the local and remote response of the coupled ocean-atmosphere system to shallow SD events that are created by prescribed wind stress anomalies over the South-Western IO with the use of ensemble simulations with the state-of-the-art coupled model EC-Earth (Hazeleger et al (2012)). We will investigate January events as climatologically the thermocline is shallow and both the SDI and the SSTs have maximum interannual variability in that month.

The content of the present chapter is organized as follows. We start with a description of the coupled model in section 5.2. The seasonality of the Seychelles Dome region is analyzed in a 40 year control simulation with EC-Earth and compared with observations. Next, in section 5.3 the experiment is described. From the control run extreme shallow doming events are selected to define the wind stress forcing for the ensemble experiment. In section 5.4 the response of the coupled system to a shallow SD doming event in January is described and discussed. The final section discusses the main results of this study.

## 5.2 Data and Model

For the D20 analysis in Fig. 5.1 we used reanalysis data from the Simple Ocean Data Assimilation (SODA) version 2.1.6 for the years 1979 – 2008

(Carton and Giese (2008)). For the same years we use SSTs from observations from the Hadley Center Sea Ice and Sea Surface Temperature data set (HadISST) (Rayner et al (2002)).

The model used in this study is the fully coupled EC-Earth global climate model. EC-Earth is based on the Integrated Forecast System (IFS) of the European Center of Medium Range Weather Forecast (ECMWF). It consists of the IFS atmospheric general circulation model coupled to the ocean general circulation model NEMO, a sea-ice model and a land model. The atmospheric component has a spectral resolution of T159, corresponding approximately to 1.125x1.125 degree horizontal resolution and the ocean resolution is 1x1 degree with a refined resolution near the equator.

In order to evaluate the IO variability simulated by EC-Earth we run a 40 year control simulation and compared the results with the observations. The model was equilibrated under constant 1850 external forcings. Next it was integrated from 1850 to 2000 under historical forcings and subsequently for another 88 years under constant year 2000 forcings. In this study we analyse the last 40 years of this simulation. Similar graphs as in Fig. 5.1 are presented for EC-Earth in Fig. 5.2. Overall the depth of the thermocline as indicated by D20 in EC-Earth is about 10-20m deeper compared to the SODA reanalysis, but the general structure is rather well simulated. In the SD region the thermocline is shallowest and the upwelling is strongest, in both model and reanalysis data. The model and the observations agree that the correlations between D20 and SST variations are maximum over the SD area. In addition, in the model the thermocline perturbations over the Western equatorial IO affect the SSTs more strongly as compared to the observations. We did not analyze the origin of this discrepancy, but possible reasons are differences in simulated wind stress anomalies, in the ocean response to wind stress anomalies and in the vertical mixing. The SDI in the model is about 10 meters too deep compared to the reanalysis, but overall the simulation has the major characteristics. In both model and reanalysis the Dome region is shallowest and most variable in winter and deepest in autumn. In the reanalysis a more pronounced biennial cycle is observed. To lay out this discrepancy, the data are separated in years where the behavior of the SDI is annual-like and in years where is biennial-like. Both cases were found in both model and reanalysis. In particular, in the model the 38% of the years show a biennial character, that increases to 74% for the reanalysis. These composites of the annual and biennial SDI cycles for the model are

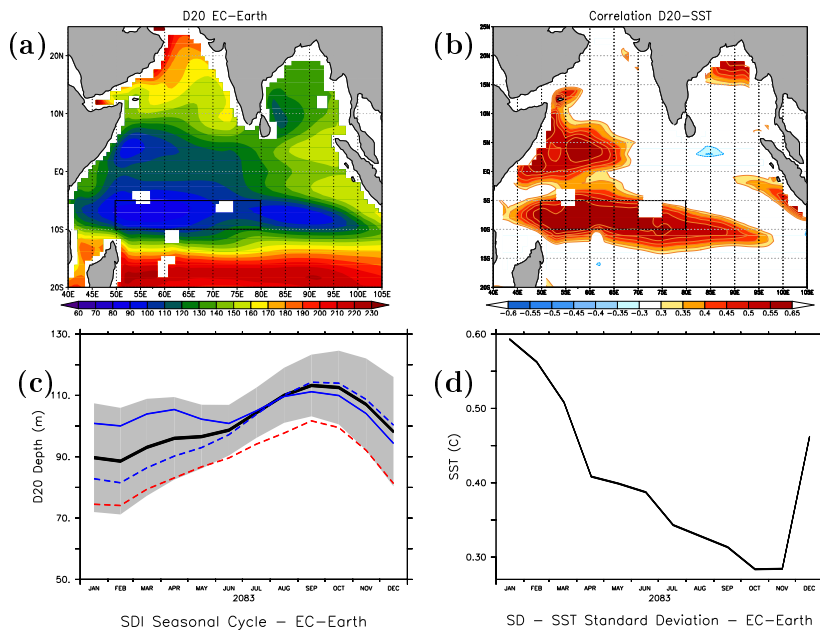


**Figure 5.2:** Same as in Fig. 5.1, but for EC-Earth data from the 40 years control run. (a) The depth of the  $20^{\circ}\text{C}$  isotherm averaged over the 40 simulation years. The depth is measured in meters. (b) The point to point correlations of monthly D20 depth anomalies with SST anomalies in the 40 simulation years. The data are detrended. The black rectangular box indicates the Seychelles Dome region. (c) The black line represents the seasonal cycle of the SDI index. The gray shaded area is one standard deviation of the interannual variations. The SDI index is the D20 anomaly averaged over the SD region expressed in meters. The red dashed line represents the averaged SDI seasonal cycle of the composite of the 5 most shallow SD years. The blue dashed line is the composite of the years with an annual-like seasonal cycle (25 years) and the solid blue line is the composite of years with an biennial-like seasonal cycle (15 years). (d) The standard deviation of interannual monthly mean SST anomalies for each month of the year. The units are in  $^{\circ}\text{C}$ .

plotted in Fig. 5.2c. Both decadal variations of the Dome region and observational uncertainties contribute to the discrepancies in the seasonal cycle of the SDI, but these contributions are hard to quantify. Similar remarks also apply to the SST variations.

## 5.3 Experimental Set-Up

### 5.3.1 The method

To study the effect of a shallow doming two ensembles of 26-months long simulations are conducted. The initial conditions are obtained from the control run. Both ensembles are initialized at the 1st of November from a year in the control simulation with a neutral SD thermocline and neutral ENSO conditions in the Pacific in the following January. For the ENSO evaluation we use the Nino 3.4 index (the averaged SST anomaly over  $170^{\circ}W - 120^{\circ}W$  and  $5^{\circ}S - 5^{\circ}N$ ). The 40 ensemble members in the unforced run differ only in stochastic perturbations to the temperature field during the first day of the simulation.

In a second ensemble the wind stress that the ocean receives from the atmosphere is replaced by a prescribed windstress forcing over the SD region in the first two months that raises the thermocline in order to force a shallow Seychelles doming event in January. In all other aspects the conditions in the forced ensemble are the same as in the unforced ensemble. Statistical significant differences between the ensemble mean fields of both ensembles can be attributed to the action of the prescribed windstress in the SD region and analysing these differences as a function of time allows us to study the response of the coupled system to a shallow Seychelles doming event in January.

### 5.3.2 Initial conditions and forcing

The imposed forcing is the composite wind stress of the November and December months preceding the 5 January months with the shallowest SD thermocline in the 40 year control run. The seasonal cycle of the SDI composite for these shallowest SD years is depicted in Fig. 5.2c by the red dashed line. The composite of the extremes follows the climatological seasonal cycle of the SDI but is about one standard deviation shallower than the mean. The composite anomalous windstress curl for December (one month before the shallow Januaries) for the entire basin is shown in Fig. 5.3a. The area where the windstress is prescribed in the forced ensemble is marked by the inner rectangle. A linear transition region between the actual and the prescribed wind stress extends  $2.5^{\circ}$  on each side and is marked in the figure by the outer rectangle.

The anomalous cyclonic curl over the SD region causes an Ekman upwelling that raises the thermocline locally in our experiment. North of

the SD region an anticyclonic curl is present. This is a reflection of the general anti-correlation between windstress curl anomalies in December in the SD region and regions to the north (Fig. 5.3b). A similar anti-correlation is found in reanalysis data, as seen in Fig. 5.3c, where 33 Decembers from MERRA (NASA’s Modern Era Retrospective-analysis for Research and Applications, Rienecker et al (2011)) for the years 1979–2011 are used. Thus, when the thermocline in the SD region is raised by the windstress curl anomaly, to the north of the region the thermocline is depressed by the windstress curl anomaly. In the current experiment, part of the anticyclonic curl is included in the forcing as it is a part of the transition region between the prescribed and the actual wind stress. This will result in a forced downwelling of the thermocline locally north of the Seychelles dome region, an aspect that will be further discussed in the next section.

The amplitude of the prescribed wind stress anomaly in the forced ensemble was enhanced in order to simulate a strong rising of the Seychelles Dome, motivated by the fact that remote forcing by ocean dynamics, that contribute to the thermocline anomalies in the SD region in nature and in the control integration, are not taken into account. The composite for November is similar (not shown).

## 5.4 Simulation Results

A graphic representation of the outcome from all runs of both ensembles is shown in Fig. 5.4. Here the evolution of the SDI for the 26 simulation months is plotted for each member of both ensembles (thin lines) and for the ensemble mean (thick line). The shallowing of the thermocline is clearly present in the forced ensemble during the first few months and the thermocline relaxes back to climatology in the months that follow. The description and interpretation of the temporal adjustment of the coupled system is discussed below for the forced phase (first two months) and the unforced phase of the simulation separately. We start with the forced phase.

### 5.4.1 Forced phase - first two months

This section describes the oceanic and atmospheric response to the imposed anomalous wind stress during November and December. During these two months the anomalous wind stress is applied over the SD region

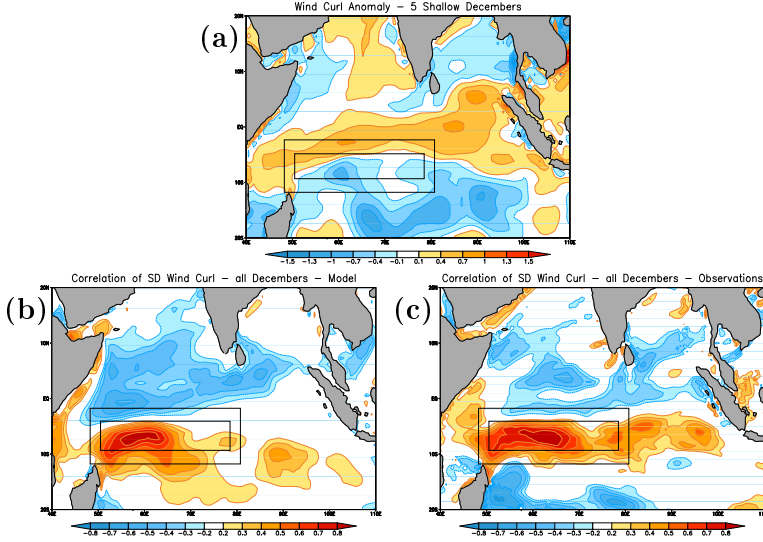


**Figure 5.3:** (a) Composite of the anomalous wind stress curl for the month of December preceding the 5 January months in the control integration with shallowest SDI. The region where we prescribe this windstress anomaly in the forced ensemble is outlined by the inner black rectangle, between  $50^{\circ}E - 80^{\circ}E$ ,  $5^{\circ}S - 10^{\circ}S$ . The transition region between the prescribed and actual windstress field in the forced ensemble is indicated by the outer rectangle. Units are  $10^{-7}Nm^{-3}$ . (b) Correlation coefficients between local anomalous wind stress curl anomalies and the area-averaged anomalous wind stress curl over the SD region in the 40 year control run for the month of December. (c) Same as in (b) for 33 Decembers from MERRA reanalysis data.

and the response is still limited to the IO basin. We start with the changes in the vertical ocean velocities due to Ekman upwelling and downwelling and continue with the SST and thermocline anomalies and their oceanic consequences. Finally we show how the atmosphere is influenced through changes in the SST.

Climatologically in boreal winter, oceanic upwelling takes place at the latitudes of the Dome and around the equator. The upwelling is part of two wind-driven cells, with two downwelling regions just north of the SD and north of the equator. The changes in the cells in response to the prescribed wind stress are depicted in Fig. 5.5b, where the change in the vertical velocity  $W$  is plotted averaged over the longitudes of the Dome ( $55^{\circ}E - 65^{\circ}E$ ). The strong cyclonic curl over the Dome (Fig. 5.5a)

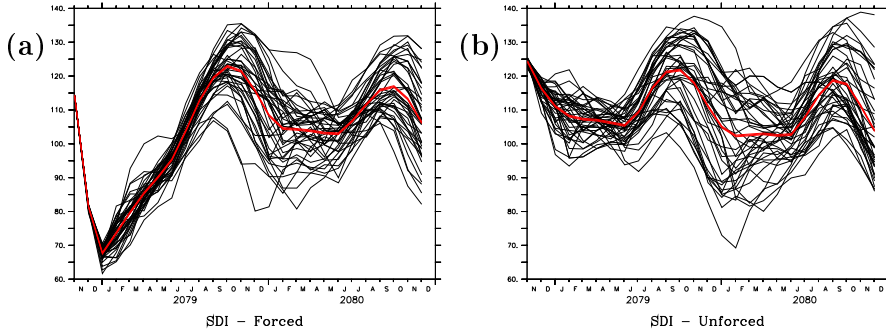


**Figure 5.4:** The evolution of the SDI for the 26 simulation months for each member of (a) the forced ensemble and (b) the unforced ensemble. Thick red lines indicate the respective ensemble means. The only difference between both ensembles is the application of a prescribed windstress over the SD region in the forced ensemble during the first two months of the simulation. Units are meters of depth.

drives an intense local Ekman upwelling that enhances the climatological regional upwelling. Just to north, around  $3 - 4^{\circ}S$ , the prescribed anticyclonic windstress curl drives the opposite Ekman motion, a downwelling, also enhancing the regional climatology. The southern wind-driven cell is strengthened and the northern cell responds with a moderate enhanced upwelling over the equator and a stronger downwelling around  $3 - 4^{\circ}N$ .

Due to the upwelling, colder water is brought from below into the mixed layer, cooling the upper ocean and eventually the SSTs as well. The downwelling results in the opposite temperature adjustments (Fig. 5.5d).

The depression of the thermocline at  $3 - 4^{\circ}S$  and  $3 - 4^{\circ}N$  sets off in November as a pair of westward propagating downwelling Rossby waves and in addition an eastward propagating downwelling Kelvin wave along the equator is triggered (Fig. 5.5c). The Rossby waves dissipate while traveling and when they reach the African coast they warm the SSTs. This can already be seen in the December SSTs. The speed of propagation of the Rossby waves is  $0.5ms^{-1}$ , somewhat slower than the theoretical speed for the first baroclinic Rossby mode between  $4^{\circ} - 2^{\circ}$  latitude of  $0.7ms^{-1}$  (Yamagata et al (2004)). The equatorial Kelvin wave takes less than a month to reach the Eastern IO boundary and deepens the thermocline there without affecting the SSTs much.



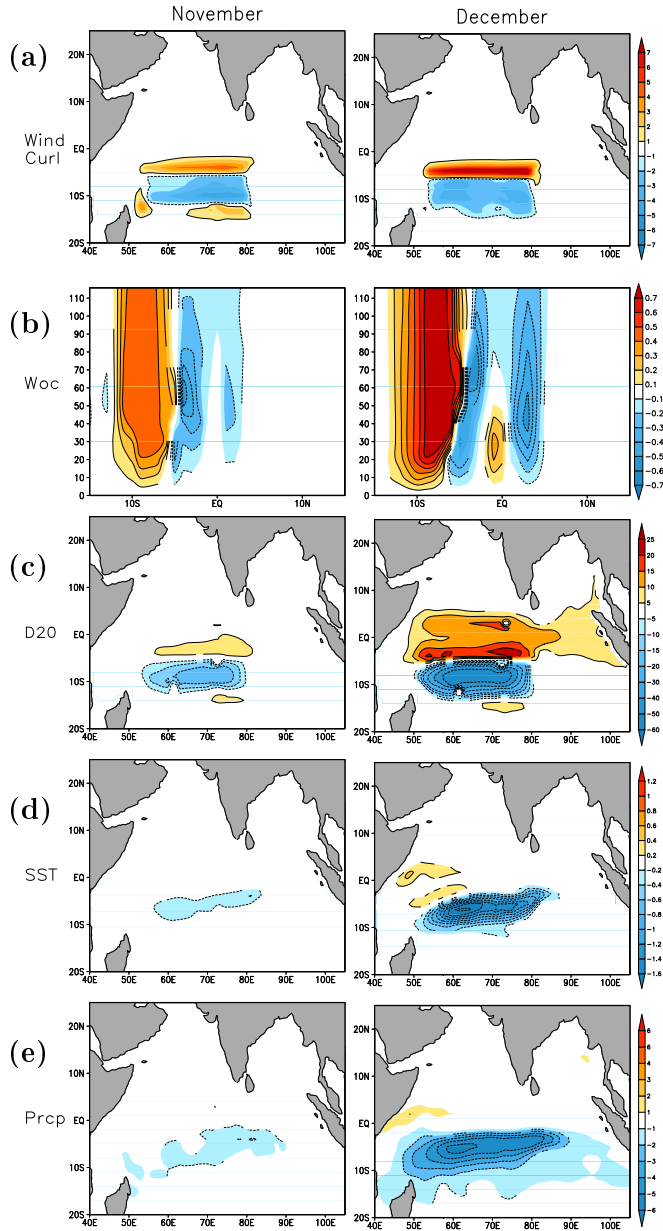


**Figure 5.5:** Differences between the two ensemble means for November and December, the months with the prescribed windstress over the SD region for (a) curl of the wind stress in  $10^{-7} Nm^{-3}$ , (b) vertical ocean velocities averaged between the longitudes  $55^{\circ}E - 65^{\circ}E$  in  $ms^{-1}$ , (c) D20 in meters, (d) SSTs in  $^{\circ}C$ , and (e) precipitation in  $mmday^{-1}$ . In all plots the contours represent areas exceeding the 98% level of significance, computed by a Student's t-test.

The precipitation (Fig. 5.5e) responds locally to the SST changes. The cooling over the Dome reduces the convection leading to a reduction in the total precipitation of significant amplitude in December, while over the warming region at the equator the first signs are visible of enhanced convection with increased precipitation in December.

This concludes the description of the forced phase of the simulation. We will continue to describe the further adjustments of the atmosphere-ocean system to the prescribed wind stress anomaly from January onwards during the unforced phase of the simulation.

### 5.4.2 Unforced phase of the simulation

We will separately discuss the adjustments along the equator, in the tropical IO south of the equator and the atmospheric response away from the equator.

#### Equatorial adjustments

We describe the equatorial ocean and atmosphere response that initiates from the Western IO basin and gradually extends to the East Pacific. We start from the SST and thermocline anomalies in the Western equatorial IO. Then continue with the subsequent changes over the Eastern equatorial IO, that are followed by adjustments in the warm pool region. The equatorial adjustments reach the East Pacific 5 – 6 months after the initiation of the SD event and beyond this time-scale the anomalies weaken as the system relaxes back to climatology.

In January the thermocline (Fig. 5.6) and SST (Fig. 5.7) adjustments reach their maximum amplitudes along the equator near the coast of Africa. The thermocline deepens up to 30m when the Rossby waves reach the coast and cause a warming of the SSTs. The atmosphere dampens this warming, as the convection is strengthened in response to the warmer SSTs (see vertical pressure velocity changes in Fig. 5.8) with increased precipitation (Fig. 5.9) and cloudiness (not shown) leading to a reduction in solar radiation reaching the surface and a net cooling of the ocean by the surface heat fluxes (Fig. 5.10). The maximum warming of the SSTs is about 1°C, which corresponds to 1.5 times the standard deviation of January anomalies in the control simulation for this region.

When the Kelvin wave reaches Indonesia the thermocline deepens up to 15m (Fig. 5.6). The SSTs do not respond significantly to this signal,

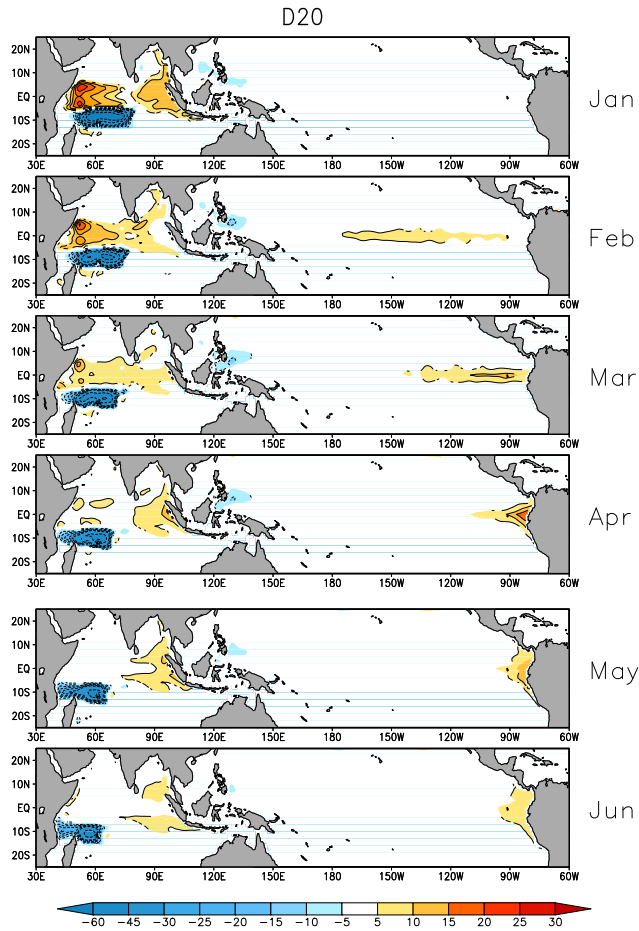


**Figure 5.6:** Differences between the forced and the unforced ensemble for the depth of the  $20^{\circ}\text{C}$  isotherm for the months January to June. The units are in meters. The contours represent the areas exceeding the 98% level of significance.

since the the sensitivity of the SSTs to thermocline changes over the Eastern IO is not strong, as is apparent in the correlation plot in Fig. 5.1 and the magnitude of the thermocline change is not very large. Additionally any warming from below is locally damped by the surface fluxes in December (not shown) and January (Fig. 5.10) that tend to cool the SSTs over the region. The negative net surface heat fluxes over the Eastern IO and Indonesia are attributed to intensified winds in the area that lead to

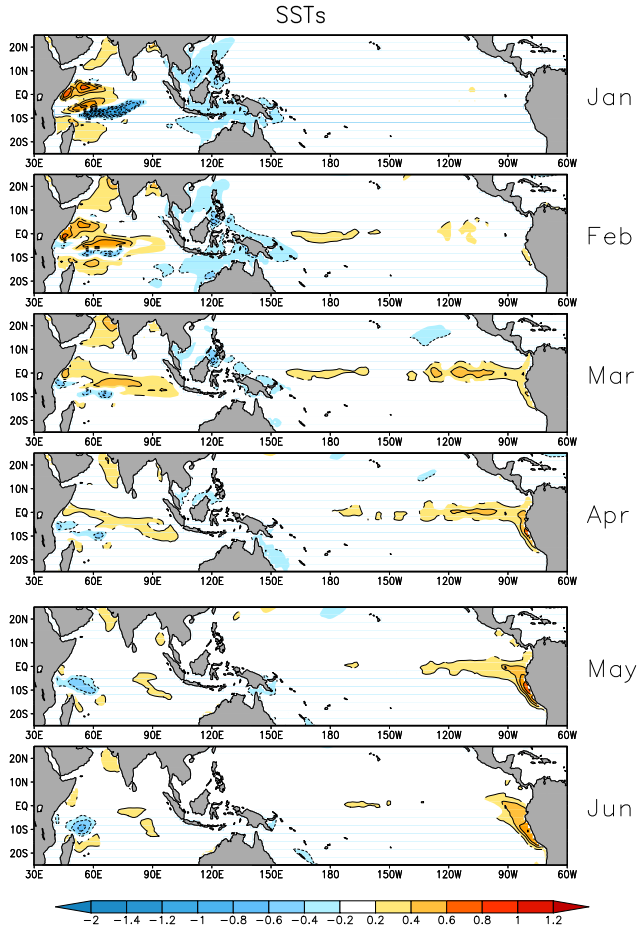


**Figure 5.7:** Differences between the forced and the unforced ensemble for the SSTs for the months January to June. The units are  $^{\circ}\text{C}$  and the contours represent areas exceeding the 98% level of significance.

enhanced cooling by the turbulent heat fluxes.

The enhanced warming over the Western equatorial IO and cooling over the Eastern equatorial IO slows down the IO Walker circulation, as evidenced by the vertical velocity (Fig. 5.8) and surface windstress changes (Fig. 5.11) with anomalous easterlies at the equator. In February, when the Walker circulation adjustments are most pronounced, the anomalous easterlies peak and cover the entire basin.

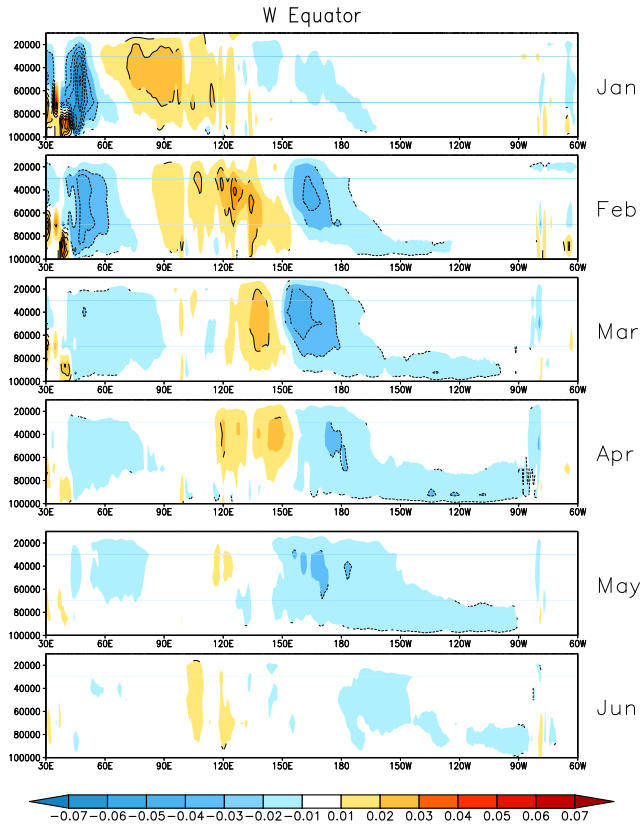


**Figure 5.8:** Differences between the forced and the unforced ensemble for the vertical pressure velocity  $W$  along the equator for the months January to June. The units are  $\text{Pa s}^{-1}$  and the contours represent the areas exceeding the 98% level of significance.

Due to the surface wind divergence over Indonesia in January, anomalous westerlies blow over the Western Pacific that shift the convective area of the warm pool eastward, around  $170^\circ\text{E}$ , where the anomalous westerlies converge with the climatological easterlies. The shift is visible in the vertical velocity (Fig. 5.8) as well as in the precipitation change (Fig. 5.9).

In the ocean, the anomalous westerly wind stress over the Western Pacific sets off a downwelling equatorial Kelvin wave in January that moves eastward, shallowing the thermocline over the Western Pacific thereby

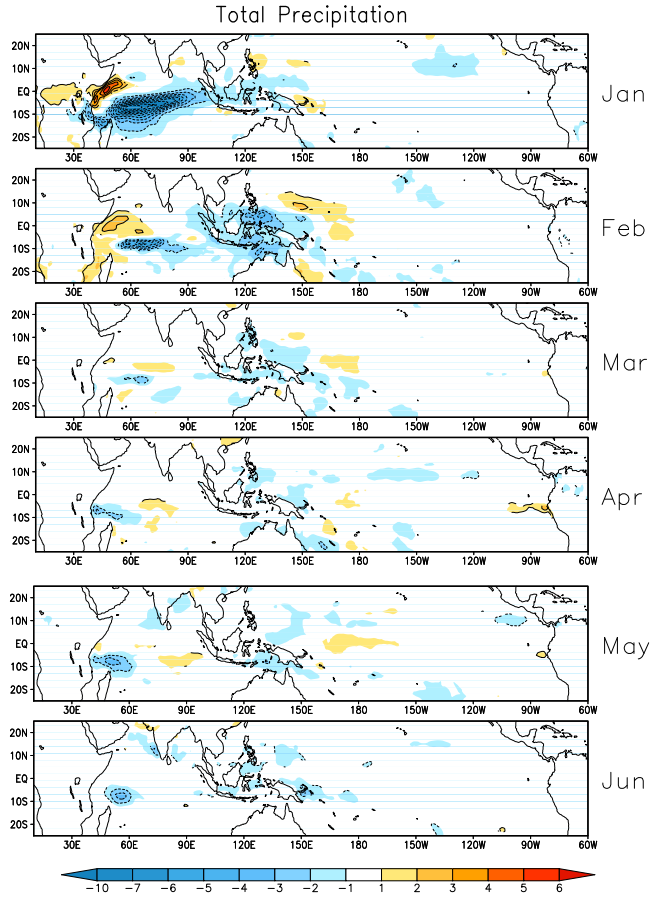


**Figure 5.9:** Differences between the forced and the unforced ensemble for precipitation for the months January to June. The units are  $\text{mm day}^{-1}$  and the contours represent areas exceeding the 98% level of significance.

enhancing the anomalous cooling and deepening the thermocline while passing over the Central and Eastern Pacific, inducing a surface warming. The wave reaches the eastern boundary in March and spreads the warming along the coast. The warming is maximum  $0.7^{\circ}\text{C}$  along the equator and reaches  $1^{\circ}\text{C}$  along the coast. The coastal warming is about half standard deviation of the local monthly climatology, and remains significant along the coast until July. The temporal evolution of the traveling wave and the induced SST anomalies is visible in the plots of the D20 (Fig. 5.6)

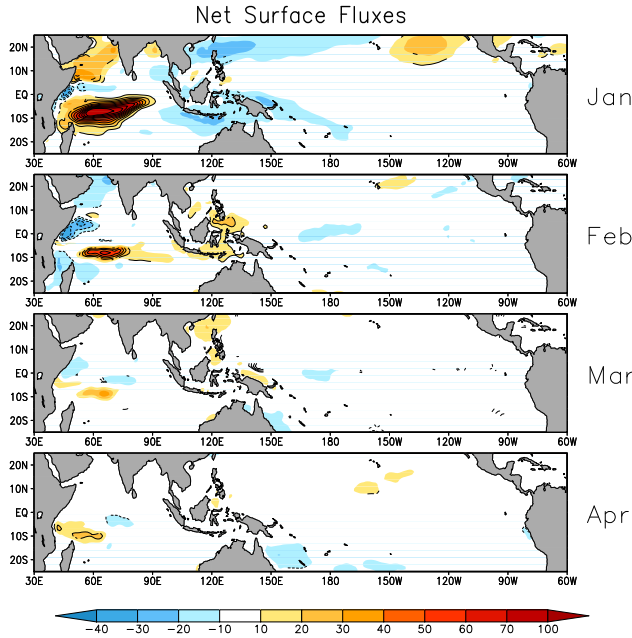


**Figure 5.10:** Differences between the forced and the unforced ensemble for the net surface heat flux for the months January to April. The net surface heat fluxes are computed as the sum of the net solar and long-wave radiation and the sensible and latent heat flux. The units are  $Wm^{-2}$  and the contours represent areas exceeding the 98% level of significance.

and the SST adjustments (Fig. 5.7).

The atmosphere weakly responds to the warming of the SSTs with some enhanced convection and precipitation, but as seen in the vertical velocity changes (Fig. 5.8), the convection adjustment is only shallow and the precipitation increase is barely  $1mmday^{-1}$  (Fig. 5.9). The induced east-west pressure gradient is not strong enough to drive strong anomalous westerlies and trigger a Bjerknes feedback that could amplify the warming and create an ENSO-like response. In the subsequent months the atmosphere and ocean relax back to climatology.

This concludes the equatorial adjustments and we continue with the adjustments in the Southern IO.

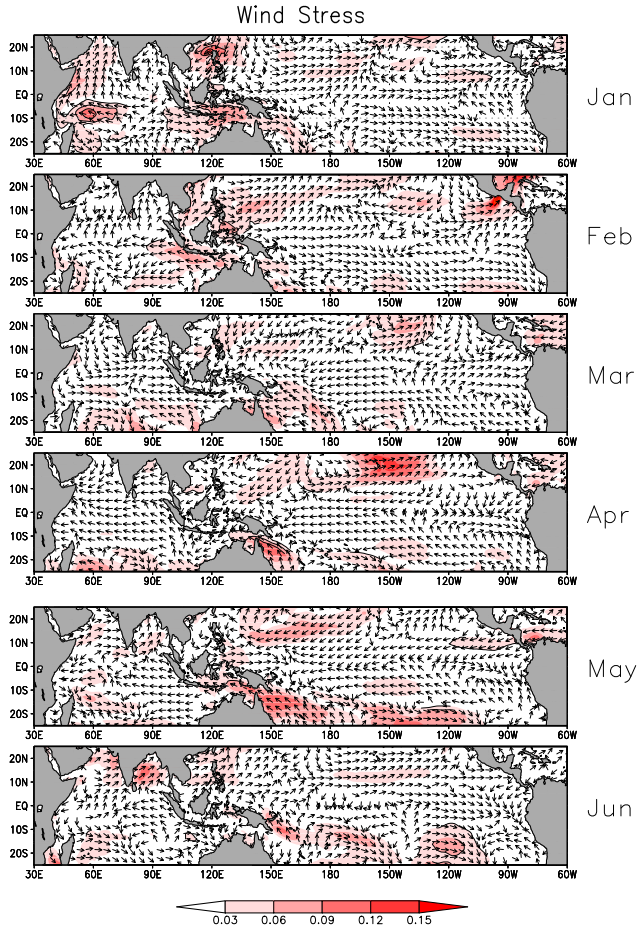


**Figure 5.11:** Differences between the forced and the unforced ensemble for the wind stress for the months January to June. The vectors show the wind direction and the amplitude of the wind stress is shaded in red colors. The units are in  $Nm^{-2}$  and the contours represent areas exceeding the 98% level of significance for the zonal wind stress difference.

### Adjustments in the Southern IO

We start this section with a description of the SDI evolution and the response and feedback of the overlying atmosphere. Then the oceanic propagation of the signal is presented and the section is concluded with a discussion of the changes in the Intertropical Convergence Zone (ITCZ).



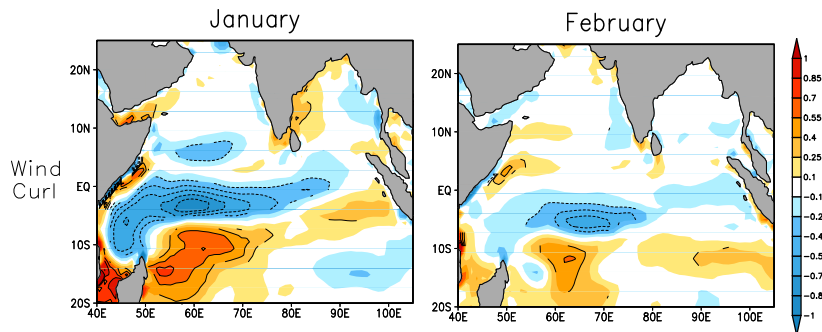


**Figure 5.12:** Differences between the forced and unforced ensemble for the wind stress curl for the months of January and February. The contours represent the areas exceeding the 98% level of significance. The units are in  $10^{-7} Nm^{-3}$ .

The temporal evolution of the adjustment of the thermocline depth in the SD region during the 26 months of simulation (Fig. 5.4) shows that after having reached a minimum depth in January of about 65 meter (an anomaly of about two standard deviations), the Seychelles dome returns to climatological values within six months. Beyond July, the Seychelles dome behaves as in the unforced ensemble.

The relatively quick return to climatology is due to an atmospheric feedback. The wind stress curl adjustment in January and to a lesser degree in February (Fig. 5.12) has opposite sign with respect to the forced wind stress curl anomaly (Fig. 5.5a) leading to Ekman downwelling in the SD region and upwelling to the north, damping the forced anomalies.

The wind stress curl changes are part of the atmospheric adjustments to the cold SSTs in the SD region. The SSTs over the Dome follow the SDI anomalies and reach maximum cooling of about  $2^{\circ}C$  in January, corresponding to two times the standard deviation locally for this month (Fig. 5.7).

The cold SSTs suppress convection in the region as evidenced by the pressure velocity changes averaged between  $5 - 10^{\circ}S$  (Fig. 5.13) and a reduction of the total precipitation (Fig. 5.9). The anomalous subsidence not only damps the cold SST anomaly by its associated wind stress curl and forced downwelling, it also adiabatically warms the air over the Dome and damps the forced cooling through the net surface heat fluxes (Fig. 5.10) that warm the ocean surface in the Dome region and to the north.

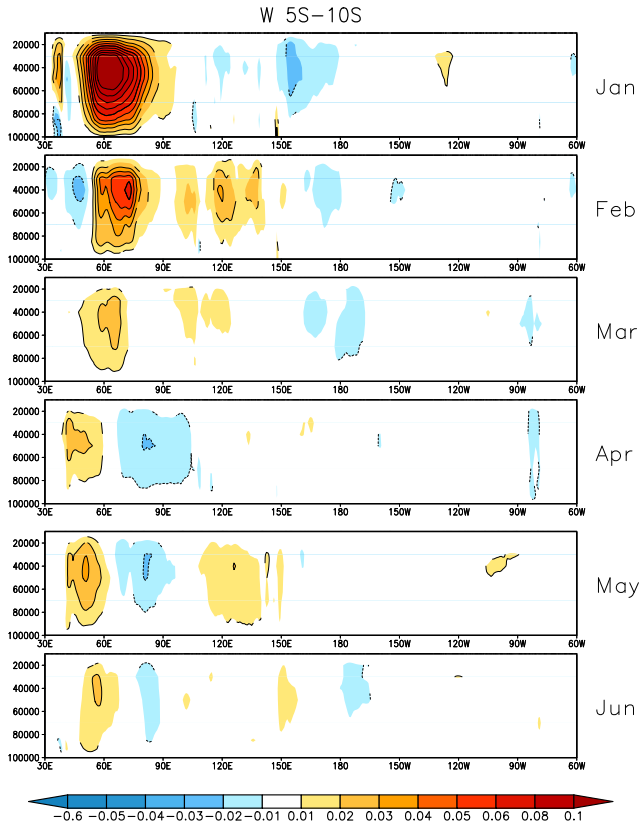


**Figure 5.13:** Differences between the forced and the unforced ensemble for the pressure velocity  $W$ , averaged over the latitudes  $5^{\circ}S - 10^{\circ}S$  for the months of January to June. The units are in  $Pa s^{-1}$ . The contours represent the areas exceeding the 98% level of significance.

Part of this warming is due to solar radiation as the reduced convection leads to reduced cloud cover in the region (not shown). The surface heat flux adjustments thus feed back negatively on the SD cooling and positively on the warming north of the SD region. By February the cold SST anomaly in the SD region is reduced by more than 50% while the warm region to the north has retained its amplitude.

The warming to the north of the SD region spreads eastward in February and March (Fig. 5.7) and atmospheric convection is weakly enhanced between  $70^{\circ}E-90^{\circ}E$  during April and May with negative pressure velocities

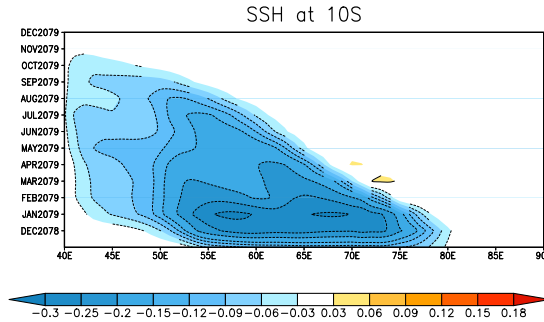


**Figure 5.14:** A Hovmöller diagram of the sea surface height differences between the forced and the unforced ensemble during the first year at  $10^{\circ}\text{S}$ . The units are in meters.

anomalies (Fig. 5.13), increased precipitation (Fig. 5.9) and cooling of the SSTs by the net surface heat fluxes (Fig. 5.10). These adjustments relax back to climatology in mid-summer.

The upward shift of the thermocline over the SD initiates an upwelling baroclinic Rossby wave that propagates westwards and dissipates. It reaches the African coast on average 8 months later, as seen in the Hovmöller diagram of the sea surface height (Fig. 5.14). The Rossby wave propagation is also clearly visible in the lat-lon plots of the SST and D20 adjustments (Fig. 5.7 and Fig. 5.6 respectively), where the center of the cold anomaly slowly moves to the west. The phase speed of the wave at  $10^{\circ}\text{S}$  is about  $0.14\text{m.s}^{-1}$ , slower than the theoretical speed of the first baroclinic mode of a free Rossby wave at this latitude for the Indian Ocean (Chelton et al (1998), Yamagata et al (2004)). The slower propagation speed has been attributed to the coupling between the ocean and the atmosphere (White (2000)) as the Rossby wave interacts with the surface winds, but could also be due to a different stratification in EC-Earth. Similar propagation speeds for this region were found by Xie et al (2002a), using in-situ measurements and model-assimilated data sets, by Tozuka et al (2010) using model simulations and others.

The combination of the cold SST anomalies over the SD region and the warm SST anomalies around the equator drive a northward shift of the ITCZ of about  $4^{\circ}$  in the Central-Western IO that is apparent until March (Fig. 5.9). In January the Northward shifts extends over Central Africa, causing a significant increase in the rainfall between  $5^{\circ}\text{S}$  and  $5^{\circ}\text{N}$

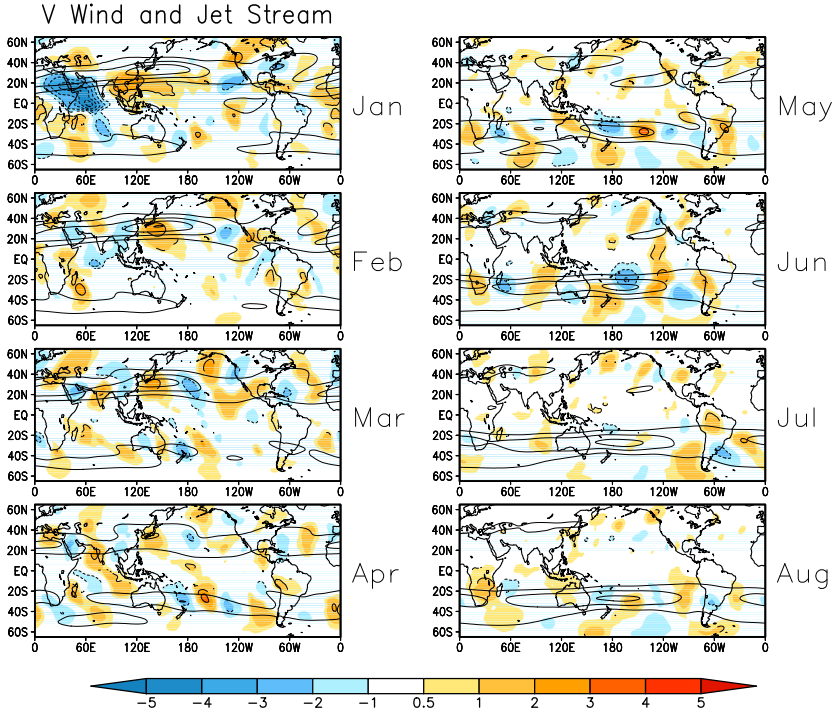


**Figure 5.15:** In colors the anomalies between the forced and the unforced ensemble for the meridional wind  $V$  are plotted and in contours is the total wind from the forced ensemble from January to August. The units are  $ms^{-1}$  and the contours around the shades represent the areas exceeding the 95% level of significance for the  $V$  anomalies. The first contour in the total wind is  $20ms^{-1}$  and the contour interval is  $15ms^{-1}$ .

and a decrease between  $12^{\circ}S$  and  $5^{\circ}S$ .

**Remote adjustments through atmospheric Rossby waves**

Changes in tropical convection potentially affects extratropical weather patterns through excitation of large-scale, atmospheric Rossby waves (Hoskins and Karoly (1981), Branstator (1983), Hoskins and Ambrizzi (1993), Trenberth et al (1998), Haarsma and Hazeleger (2007)). The anomalous upper level winds accompanying the change in convection constitute a Rossby wave source (Sardeshmukh et al (1987)) and Rossby wave energy disperses away from the tropics, sometimes trapped by the atmospheric jets that

can act as a Rossby wave guide (Branstator (2002)). The strength of the waveguide response depends on the position of the Rossby wave source with respect to the jet and the width and strength of the jet itself (Manola et al (2013)), such that in the winter season, the waveguide response is generally strongest.

The waveguide response is most easily visualized by upper level meridional wind anomalies. Fig. 5.15 shows the meridional wind anomalies at 200 hPa on top of total wind contours to indicate the position of the jet stream. In January a strong response is observed over the north-western and north-eastern IO, where a significant Rossby wave source is present due to the strong convection anomalies. A wave-like response continues along the winter jet stream and crosses the Northern American continent. In February and March the strong response over the IO mitigates, as the convection anomalies reduce, but a stationary Rossby wave pattern is persistent along the northern hemisphere jet stream. In April the jets are going through the seasonal transition and are weak in both hemispheres, therefore the wave anomalies are less significant. The following two months the southern hemisphere jet gains strength and picks up the signal from the cold anomaly over the SD that is still significant, and a Rossby wave response is present in the southern hemisphere. In July the Rossby wave source is very weak as the convection adjustments have virtually relaxed back to climatology.

## 5.5 Summary and Discussion

In this chapter we used the coupled atmosphere-ocean EC-Earth model to study the response of the climate system to a shallow Seychelles Dome event in January. We found that the influence of the shallow event extends from the Indian Ocean into the East Pacific by a chain of events during the subsequent 6-8 months.

The forced upwelling in the SD region leads to a cold SST anomaly. In the subsequent months this anomaly propagates westwards in the form of a Rossby wave. The atmospheric convection is suppressed above the cold anomaly and the associated surface wind curl anomaly damps the upwelling Rossby wave. An equatorial adjustment north of the SD region manifests as a pair of downwelling westward moving Rossby waves and an eastward downwelling equatorial Kelvin wave. The Rossby waves warm the SSTs in the equatorial Western IO two months after the ini-

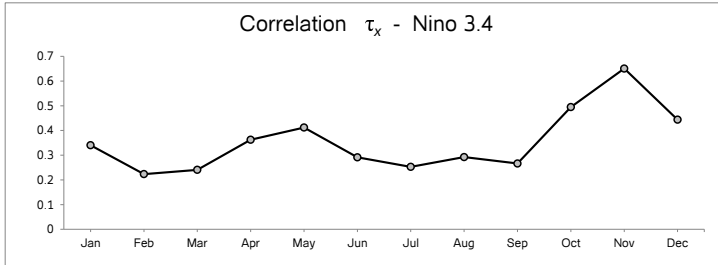


**Figure 5.16:** The correlation between the Nino 3.4 index and zonal wind stress averaged over the same area from the 40 years of control run. The Nino 3.4 index is the averaged SST anomaly over  $170^{\circ}W - 120^{\circ}W$  and  $5^{\circ}S - 5^{\circ}N$ .

tiation of the Doming event and induce enhanced atmospheric convection. A Walker-type response follows with suppressed convection over the Indonesia-Warm Pool region. Here the SSTs cool through enhanced turbulent heat fluxes, resulting from stronger surface winds. The atmospheric convection is enhanced east of the warm pool region and a westerly wind anomaly sets off a downwelling Kelvin wave at the edge of the Pacific Warm Pool. The Kelvin wave arrives near the coast of Peru around 4 months after the initiation of the shallow SD event, resulting in a  $0.5^{\circ}C$  warming of the equatorial SSTs. A small weakening of the subsidence in the overlying atmosphere is simulated, but no indication of an unstable atmosphere-ocean interaction is found and the equatorial response is damped. This season is not favorable for unstable air-sea interactions. This is shown in Fig. 5.16, where the Nino 3.4 index is correlated with the zonal wind stress, indicating that the most favorable month for a strong air-sea coupling is November. We therefore suggest to repeat these type of experiments for different timings of the Doming events in the seasonal cycle. A Doming event starting in June could possibly trigger an ENSO in the Pacific, if conditions are favorable. A similar equatorial response to an IOD, for a different season though, is introduced in Izumo et al (2010). They suggest that an IOD event may act as a precursor of an El Niño or a La Niña event: the east-west temperature anomalies during the IOD event modify the Walker circulation. The zonal wind anomalies over the Pacific Ocean during the termination of the IOD in the autumn force a Kelvin wave that propagates towards the eastern Pacific. The wave modulates the thermocline depth and the SSTs and through a Bjerknes feedback it

can lead to the development of an El Niño or a La Niña event.

The combination of warm and cold SST anomalies over the equator and the SD drive a northward shift in the ITCZ that in January extends over the Central-East Africa influencing the precipitation. A shift of the ITCZ can also influence the onset of the monsoon period if it takes place in the right season. Annamalai et al (2005a) found that a warming in the South-West IO in spring causes a delay in the northward propagation of the ITCZ and the associated deep moist layer, provoking a delay of 6-7 days on the onset of the monsoon in June. Therefore it is possible that cold SD events, similar to those studied in this chapter, taking place in April and May would force a premature initiation of the summer Indian monsoon.

In response to the atmospheric convection change in the equatorial IO, atmospheric Rossby waves are emanated and are visible in the winter hemisphere waveguides. As these responses depend on the atmospheric state, these would be different for different timings of Seychelles doming event in the seasonal cycle as well.

EC-Earth has a stronger coupling between the thermocline and the SSTs in the Western equatorial IO, as compared to observations. This probably makes the documented remote response to the SD event stronger than in nature. We therefore recommend to repeat these type of experiments with other models to assess the model dependency of these results and extend the observational analysis.

*Acknowledgments.* The authors would like to thank Richard Bintanja and Camiel Severijns for their important contribution to the model set up. This work is part of the research programme INATEX, which is financed by the Netherlands Organisation for Scientific Research (NWO).





---

# CHAPTER 6

---

## Conclusions and discussion

The objective of this dissertation is to increase our understanding on teleconnections that originate from tropical perturbations. A better understanding of the dynamics of the atmospheric teleconnections and their interactions with the ocean can contribute to the development of skillful weather and seasonal forecasts and to a better analysis of the future climate change signals.

The extratropical teleconnections are connected to the tropics mainly through excitation and propagation of atmospheric Rossby waves. The tropical teleconnections often involve atmospheric and oceanic Rossby and Kelvin waves, as well as a strong interactions between the ocean and the atmosphere. Here we concentrate on teleconnections that relate to the Indian Ocean (IO), either directly by studying phenomena that emanate from the IO basin, or indirectly, by investigating the origins of the NAO pattern in Atlantic, as it is found that the warming of the IO projects on the positive phase of the NAO.

To meet our goal, model simulations were performed, motivated by observational and reanalysis data. The complexity of the model simulations escalate while going through this dissertation. We start with an idealized experiment using a simple barotropic model, then we perform a more realistic experiment with the same model using actual atmospheric flows and we conclude this thesis using a state-of-the-art fully coupled climate model.

## 6.1 Summary of work

The major atmospheric jet streams can act as waveguides for Rossby waves as they can trap the energy from a vorticity source and transfer the information around the globe, alternating the weather patterns and creating teleconnections. This ability of the jet stream is called “waveguidability”. In **chapter 2** we study how different aspects of the jet, such as the strength, the width and the location of the jet can constrain specific features of the trapped, zonal waves such as their wavenumber and amplitudes. A systematic analysis to assess the ability of the jet stream to guide Rossby waves is performed using a barotropic model. Idealized zonal jets with a Gaussian meridional profile are forced by idealized subtropical Rossby wave sources to find that stronger and narrower jets lead to stronger zonal waves and that the stronger the jet, the smaller the wave number becomes. A maximum response in the waveguide is found when the circumglobal stationary wave number is integer, through constructive interference between the source and the response.

A confirmation of the above findings from observations was proved to be not an easy task. That is due to the complexity of the atmospheric dynamics, a lot of noise is added on the initial signal. In reality there is no completely steady source of Rossby wave energy, while when the Rossby waves grow to large amplitudes they can break and interact strongly with the flow. The observed jets are not exactly zonal and continuous and baroclinicities in the jet may play a role in the generation and maintenance of zonal waves. Nonetheless the basic conclusions concerning the waveguidability of the jet stream are still considered to be valid.

In the following study, in **chapter 3**, we compare the structure of the Northern Hemisphere winter jet streams during positive and negative phases of the NAO. Differences are found in the strength, width and zonal asymmetries of these jet structures, while a clear wave pattern is shown in the meridional velocity field. The scope of this work is to quantify the extend of the tropical and extratropical contribution to the formation of the wave pattern for both NAO phases separately on time scales between 10-60 days using a barotropic model. The forcing of the patterns from reanalysis data is assumed to be the Rossby Wave Source for the tropics and the eddy activity for the extratropics. The model forcing is inversely determined, derived from the barotropic vorticity equation separately for the tropics and extratropics using winds. The model forcing patterns bear resemblance with the estimates from the reanalysis data, verifying that

the barotropic model can be used to diagnose the impact of local and remote forcing. The forcing for the tropics and extratropics was imposed separately in the model. The amplitude of tropical contribution to the total kinetic wave energy of the positive NAO is 14% and is enhanced to 35% for the negative NAO, that is a sign of non-linearity of the NAO. An important result is that the tropical forcing in both phases appears to reduce the amplitude of meridional wind anomaly pattern that is associated with the NAO as a result of a negative feedback generated in the extratropics.

The next research question of this thesis concerns a region in the Southwest IO that is characterized by a shallow thermocline and experiences large variability and strong seasonal upwelling, the Seychelles Dome (SD). Variations in the SD region are known to influence the atmospheric evolution around the basin, including the Indian monsoon and East African rainfall, and it has been hypothesized that its influence could extend far into the Pacific ocean and into the extra-tropics. This assumption is tested using the fully-coupled Earth system model EC-Earth. Before that, it was necessary to evaluate the IO climatology in EC-Earth to assess the reliability of the model outcome. For that the latter 40 years of a 250 year coupled simulation over IO were examined and compared with observations in **chapter 4**. The analysis shows realistically captured the development of winter and summer monsoon. Bias appear in all fields, some of them are pervasive, being common to most simulations, most likely driven by the SST biases, calculated about 1 degree too cold. The model show overall excessive precipitation over the Western IO basin and a deficit over the Eastern basin. The onset and offset of the monsoonal periods are reasonably well presented. The most challenging field to capture was the depth of the thermocline, where a stronger linkage to the ocean currents and the vertical mixing processes is shown. Overall, the spatial distribution of the wind, precipitation and sea-surface temperature is simulated quite realistically throughout the year and EC-Earth is proved a reliable tool to study events in the IO.

In **chapter 5** the adjustments of the coupled atmosphere-ocean system to a shallow doming event using the EC-Earth climate model are investigated in detail. The adjustments are followed in time by studying the ensemble mean difference between an ensemble of simulations with and without a shallow doming event, created by the application of a wind-stress curl anomaly in the Seychelles Dome region during November and December. The anomalous doming creates an equatorial eastward mov-

ing Kelvin wave and a pair of westward moving Rossby waves, leading to warming of the SSTs 1 – 2 months later in the western equatorial region. Atmospheric convection is triggered and a Walker type response results with reduced convection over the Indonesian warm pool and cooling of the SSTs in that region due to stronger surface winds. The Pacific warm pool convection shifts eastward and the accompanying westerly surface wind anomaly triggers an oceanic Kelvin wave. This wave crosses the equatorial Pacific and leads to SST warming in April near the coast of Peru, 5 – 6 months after the initiation of the SD event. Here the SST anomaly triggers weak anomalous atmospheric convection but is dissipated in the following month. In response to the changes in atmospheric convection, large-scale Rossby waves are triggered in the atmospheric waveguide, moving away from the equator into the extra-tropics but the amplitudes are relatively weak.

## 6.2 Outlook

In this work we attempt to cast some light on atmospheric dynamics associated with the propagation of Rossby waves along the jet stream, the formation of NAO patterns from tropical and extratropical sources and the impact of a shallow thermocline event of the Seychelles Dome on the coupled ocean-atmosphere system. The complexity of such systems is that, that a vast field of information is still to be unraveled. At the same time, the outcome of this work inspires new research questions and motivates new experiments.

In chapter 3 it is shown that the tropics reduce the amplitude of the NAO pattern for the selected events. The mechanism of the tropical damping is yet unclear and is left for future consideration, as well as the sensitivity of the quantities of the tropical and extratropical impact to the particular selection of NAO events has to be determined. The fact that the tropics can play an important role in the formation of the NAO patterns, in combination with the time scale of 10 – 60 days, that is relevant with the time that the atmospheric dynamics need to set up teleconnections, can motivate future research on particular tropical events such as the Madden-Julian Oscillation in the Indian and Pacific Oceans to quantify the impact of such events on the formation of NAO patterns.

In chapter 5 we discussed the influence of a shallow thermocline event over the Seychelles Dome in January on the climate system, to find mul-

multiple implications that can motivate future research. The most prominent among them was the warm SST response in the Eastern Pacific around March, 6 – 8 months after the SD event. This time of the year is not favorable for an unstable air-sea interaction and soon the SST anomaly is damped. It appears that the most favorable season is around November. This implies that an SD event starting around June could cause a larger response in the East Pacific, and if the conditions are favorable even trigger an ENSO. The depth of the SD has a biennial cycle and in June we find the second minimum (after January), therefore a shallow event around this time could happen. This assumption is left for future research.

Another interesting response is the shift of the ITCZ associated with the shallow SD anomaly. If the timing is right, a shift in the ITCZ can have an impact on the initiation of the summer monsoon. An SD event taking place in middle-late spring, through its effect on the ITCZ, could either accelerate (in case of a shallow SD anomaly) or delay (in case of a deep SD anomaly) the onset of the monsoon and have an impact on the precipitation in India and the surrounding regions.

The strong impact of such a shallow SD event on the SSTs, the convection and the precipitation can possibly influence significantly other events, such as the South-Western Indian Ocean cyclone evolution, that peaks between December and June, or the initiation and propagation of a Madden-Julian Oscillation event. To investigate further the issues mentioned above we would suggest to study events from observations and if evidence is found to perform model experiments in a similar way to that of chapter 5, in the appropriate season for the specific event and with time scales of days, in case of the monsoon or the tracking of cyclones, or weeks in case of events such as the Madden-Julian Oscillation.



# Bibliography

- Annamalai H, Liu P, Xie SP (2005a) Southwest Indian Ocean SST variability: Its local effect and remote influence on Asian monsoons. *J Clim* 18:4150–4167
- Annamalai H, Xie SP, McCreary JP, Murtugudde R (2005b) Impact of Indian Ocean sea surface temperature on developing El Niño. *J Clim* 18:302–319
- Annamalai H, Okajima H, Watanabe M (2007) Possible impact of the Indian Ocean SST on the Northern Hemisphere circulation during El Niño. *J Clim* 20:3164–3189
- Barnston AG, Livezey RE (1987) Classification, Seasonality and Persistence of Low-Frequency Atmospheric Circulation Patterns. *Mon Wea Rev* 115:1083–1126
- Behera S, Krishnan S, Yamagata T (1999) Atmosphere conditions in the tropical Indian Ocean during 1994. *Geophys Res Lett* 26:3001–3004
- Behera SK, Luo JJ, Masson S, Rao SA, Sakuma H, Yamagata T (2006) A CGCM study on the interaction between IOD and ENSO. *J Clim* 19(9):1688–1705
- Benedict J, Lee S, Feldstein S (2004) Synoptic view of the North Atlantic Oscillation. *J Atmos Sci* 61:121–144
- Biastoch A, Boning CW, Scharzkopf FU, Lutjeharms JRE (2009) Increase in Agulhas leakage due to poleward shift of Southern Hemisphere westerlies. *Nature* 462(7272):495–498
- Bollasina M, Nigam S (2008) Indian Ocean SST, evaporation, and precipitation during the South Asian summer monsoon in IPCC-AR4 coupled simulations. *Clim Dyn* 33(7-8):1017–1032
- Branstator G (2002) Circumglobal teleconnections, the jet stream waveguide, and the North Atlantic Oscillation. *J Clim* 15:1893–1910

- Brandefelt J, Körnich H (2008) Northern Hemisphere Stationary Waves in Future Climate Projections. *J Clim* 21:6341–6353
- Branstator GW (1983) Horizontal energy propagation in a barotropic atmosphere with meridional and zonal structure. *J Atmos Sci* 40:1689–1708
- Branstator GW, Selten FM (2009) Modes of variability and climate change. *J Clim* 22:2639–2658
- Cai W, van Rensch P, Cowan T, Hendon HH (2011) Teleconnection pathways of ENSO and the IOD and the mechanisms for impacts on Australian rainfall. *J Clim* 24:3910–3923
- Carton JA, Giese BS (2008) A Reanalysis of Ocean Climate Using Simple Ocean Data Assimilation (SODA). *Mon Wea Rev* 136:2999–3017
- Carton JA, Chepurin G, Cao X (2000a) A simple ocean data assimilation analysis of the global upper ocean 1950-1995 part II: Results. *J Phys Oceanogr* 30:311–326
- Carton JA, Chepurin G, Cao X, Giese B (2000b) A simple ocean data assimilation analysis of the global upper ocean 1950-1995 part I: Methodology. *J Phys Oceanogr* 30:294–309
- Cassou C (2008) Intraseasonal interaction between the Madden-Julian Oscillation and the North Atlantic Oscillation. *Nature* 455:523–527
- Cassou C, Terray L, Hurrell JW, Deser C (2004) North Atlantic winter climate regimes: Spatial asymmetry, stationarity with time, and oceanic forcing. *J Clim* 17:1055–1068.
- Cayan DR (1992a) Latent and sensible heat flux anomalies over the northern oceans: Driving the sea surface temperature. *J Phys Oceanogr* 22(8):859–881
- Cayan DR (1992b) Latent and sensible heat flux anomalies over the northern oceans: The connection to monthly atmospheric circulation. *J Clim* 5:354–369
- Chang P, Ji L, Li H (1997) A decadal climate variation in the tropical Atlantic Ocean from thermodynamic air-sea interaction. *Nature* 385:516–518
- Charney JG (1971) Tropical cyclogenesis and the formation of the intertropical convergence zone. *Math Probl of Geophys Fl Dyn* 13:355–368
- Chelton DB, Deszoeke RA, Schlax MG, Naggar KE, Siwertz N (1998) Geographical variability of the first baroclinic Rossby radius of deformation. *J Phys Oceanogr* 28(3):433–460



- Cook KH (2000) The South Indian convergence zone and interannual rainfall variability over southern Africa. *J Clim* 13:3789–3804
- Czaja A, Robertson AW, Huck T (2003) The role of Atlantic ocean-atmosphere coupling in affecting North Atlantic Oscillation variability. *Geophys Monograph Ser* 134:147–172
- Dai A (2006) Precipitation Characteristics in eighteen coupled climate models. *J Clim* 18:4605–4630
- Dee D, Coauthors (2011) The ERA-Interim reanalysis: Configuration and performance of the data assimilation system. *Quart J Roy Meteor Soc* 137:553–597
- Dickson RR, Lazier J, Meincke J, Rhines P, Swift J (1996) Long-term co-ordinated changes in the convective activity of the North Atlantic. *Prog Oceanogr* 38:241–295
- Ding Q, Wang B, Wallace JM, Branstator GW (2011) Tropical-extratropical teleconnections in boreal summer: observed interannual variability. *J Clim* 24:1878–1896
- Du Y, Xie SP (2008) Role of atmospheric adjustment in the tropical Indian Ocean warming during the 20th century in climate models. *Geophys Res Lett* 35(8)
- Duvel JP, Roca R, Vialard J (2004) Ocean mixed layer temperature variations induced by intraseasonal convective perturbations over the Indian Ocean. *J Atm Sci* 61(9):1004–1023
- Feldstein SB (2000) Teleconnections and ENSO: The timescale, power spectra, and climate noise properties. *J Clim* 13:4430–4440
- Feldstein SB (2003) The dynamics of NAO teleconnection pattern growth and decay. *Quart J Roy Meteor Soc* 129:901–924
- Feng M, Meyers G (2003) Interannual variability in the tropical Indian Ocean: a two-year time-scale of Indian Ocean Dipole. *Deep Sea Research Part II: Topical Studies in Oceanography*. 50(12):2263–2284
- Fischer AS, Terray P, Guilyardi E, Gualdi S, Delecluse P (2005) Two independent triggers for the Indian Ocean dipole/zonal mode in a coupled GCM. *J Clim* 18(7):3428–3449
- Franzke C, Lee S, Feldstein S (2003) Is the North Atlantic Oscillation a breaking wave? *J Atmos Sci* 61:145–160
- Goddard L, Graham NE (1999) The importance of the Indian Ocean for simulating precipitation anomalies over eastern and southern Africa. *J Geophys Res* 104:19,099–19,116

- Greatbatch RJ, Jung T (2006) Local versus tropical diabatic heating and the winter North Atlantic Oscillation. *J Clim* 20:2058–2075
- Greatbatch RJ, Gollan G, Jung T (2012) An analysis of trends in the boreal winter mean tropospheric circulation during the second half of the 20th century. *Geophys Res Lett* 39
- Guijun G, Chidong Z (2001) A Spectrum Analysis of Synoptic-Scale Disturbances in the ITCZ. *J Clim* 14:2527–2539
- Gupta AK, Sarkar S, De S, Clemens SC, Velu A (2010) Mid-Brunhes strengthening of the Indian Ocean Dipole caused increased equatorial East African and decreased Australasian rainfall 37(6)
- Haarsma RJ, Hazeleger W (2007) Extra-tropical atmospheric response to Equatorial Atlantic cold tongue anomalies. *J Clim* 20:2076–2091
- Harrison DE, Vecchi GA (2001) January 1999 Indian Ocean cooling event. *Geophys Res Lett* 28(19):3717–3720
- Hayashi Y (1982) Space-time spectral analysis and its applications to atmospheric waves. *J Meteor Soc Japan* 60:156–171
- Hazeleger W, Wang X, Severijns C, Stefanescu S, Bintanja R, A Sterl KW, et al (2012) EC-Earth V2. 2: description and validation of a new seamless earth system prediction model. *Clim Dyn* 39(11):2611–2629
- Hermes JC, Reason CJC (2008) Annual cycle of the south Indian Ocean (Seychelles-Chagos) thermocline ridge in a regional oceanmodel. *J Geophys Res* 113:C04,035
- Hoerling MP, Hurrell JW, Xu T, Bates GT, Phillips AS (2004) Twentieth century North Atlantic climate change. Part II: Understanding the effect of Indian Ocean warming. *Clim Dyn* 23:391–405
- Hoskins BJ, Ambrizzi T (1993) Rossby wave propagation on a realistic longitudinally varying flow. *J Atmos Sci* 50:1661–1671
- Hoskins BJ, Karoly DJ (1981) The steady linear responses of a spherical atmosphere to thermal and orographic forcing. *J Atmos Sci* 38:1179–1196
- Hoskins BJ, Simmons AJ, Andrews DC (1977) Energy dispersion in a barotropic atmosphere. *Quart J Roy Meteor Soc* 103:553–567
- Hurrell JW (1995) Decadal trends in the North Atlantic Oscillation regional temperatures and precipitation. *Science* 269:676–679
- Hurrell JW, Kushnir Y, Ottensen G, Visbeck M (2003) An Overview of the North Atlantic Oscillation. *Geophys Monograph Ser* 134:1–35

- Hurrell JW, Hoerling MP, Phillips AS, Xu T (2004) Twentieth century North Atlantic climate change. Part I. Assessing determinism. *Clim Dyn* 23:371–389
- Izumo T, de Boyer Montegut C, Luo JJ, Behera SK, Masson S, Yamagata T (2008) The role of the western Arabian Sea upwelling in Indian monsoon variability. *J Clim* 21:5603–5623
- Izumo T, Vialard J, Lengaigne M, de Boyer Montegut C, Behera S, Luo J, Cravatte S, Masson S, Yamagata T (2010) Influence of the state of the Indian Ocean Dipole on the following year's El Nino. *Nature Geosc* 3(3):168–172
- Jayakumar A, Vialard J, Lengaigne M, McCreary JP, Gnanaseelan C, Kumar BP (2011) Processes controlling the surface temperature signature of the Madden–Julian Oscillation in the thermocline ridge of the Indian Ocean. *Clim Dyn* 37(11-12):2217–2234
- Jochum M, Murtugudde R (2005) Internal variability of Indian Ocean SST. *J Clim* 18:3726–3738
- Kalnay E, Kanamitsu M, Kistler R, Collins W, Deaven D, Gandin L, Iredell M, et al (1996) The NCEP/NCAR 40-year reanalysis project. *Bull Amer Meteor Soc* 77:437–470
- Klein SA, Soden BJ, Lau NC (1999) Remote sea surface temperature variations during ENSO: Evidence for a tropical atmospheric bridge. *J Clim* 12(4):917–932
- Kummerow C, Simpson J, Thiele O, Barnes W, Chang ATC, Stocker E, Adler RF, et al (2000) The status of the Tropical Rainfall Measuring Mission (TRMM) after two years in orbit. *J Appl Meteorol* 39:1965–1982
- Kushnir Y, Lau NC (1992) The general circulation model response to a North Pacific SST anomaly: Dependent on timescale and pattern polarity. *J Clim* 5:271–283
- Kushnir Y, Wallace JM (1989) Low frequency variability in the Northern Hemisphere winter: Geographical distribution, structure and time dependence. *J Atmos Sci* 46:3122–3142
- Lacagnina C, Selten F (2013) Evaluation of clouds and radiative fluxes in the EC-Earth general circulation model. *Clim Dyn* pp 1–20
- Latif M, Dommenges D, Dima M, Gratzner A (1999) The role of Indian Ocean sea surface temperature in forcing east African rainfall anomalies during December–January 1997/98. *J Clim* 12:3497–3504

- Lau KM, Weng H (2002) Recurrent teleconnection patterns linking summertime precipitation variability over East Asia and North America. *J Met Soc Japan* 80:1309–1324
- Li S, Robinson WA, Hoerling MP, Weickmann KM (2007) Dynamics of the extratropical response to a tropical Atlantic SST anomaly. *J Clim* 20:560–574
- Lin H, Derome J, Greatbatch RJ, Peterson KA, Lu J (2002) Tropical links of the Arctic Oscillation. *Geophys Res Lett* 29
- Liu Z, Alexander M (2007) Atmospheric bridge, oceanic tunnel, and global climatic teleconnections. *Rev Geophys* 45(2)
- Lloyd ID, Vecchi GA (2010) Submonthly Indian Ocean cooling events and their interaction with large-scale conditions. *J Clim* 23:700–716
- Lu J, Greatbatch RJ, Peterson KA (2004) Trend in Northern Hemisphere winter atmospheric circulation during the last half of the twentieth Century. *J Clim* 17:3745–3760
- Luffman JJ, Taschetto AS, England MH (2009) Global and regional climate response to late 20th century warming over the Indian Ocean. *J Clim* 23:1660–1676
- Madden RA, Julian PR (1994) Observations of the 40-50-day Tropical Oscillation-A review. *Mon Wea Rev* 122(5):814–837
- Manola I, Selten F, de Vries H, Hazeleger W (2013) “Waveguidability” of idealized jets. *J Geophys Res Atm* 118(18):10–432
- Masumoto Y, Meyers G (1998) Forced Rossby waves in the southern tropical Indian Ocean. *J Geophys Res* 103:27,589–27,602
- Murtugudde R, Busalacchi AJ (1999) Interannual variability of the dynamics and thermodynamics of the tropical Indian Ocean. *J Clim* 12:2300–2326
- Nagura M, Konda M (2007) The seasonal development of an SST anomaly in the Indian Ocean and its relationship to ENSO. *J Clim* 20(1):38–52
- Nigam S, Shen HS (1993) Structure of oceanic and atmospheric low-frequency variability over the tropical Pacific and Indian Oceans. Part I: COADS observations. *J Clim* 6:657–676
- Okajima H, Xie SP, Numaguti A (2003) Interhemispheric coherence of tropical climate variability: effect of the climatological ITCZ. *J Meteor Soc Japan* 81:1371–1386

- Okumura Y, Xie SP, Numaguti A, Tanimoto Y (2001) Tropical Atlantic air-sea interaction and its influence on the NAO. *Geophys Res Lett* 28:1507–1510
- Peng S, Robinson WA, Li S, Hoerling MP (2005) Tropical Atlantic SST forcing of coupled North Atlantic seasonal responses. *J Clim* 18:480–496
- Peterson KA, Greatbatch RJ, Lu J, Lin H, Derome J (2002) Hindcasting the NAO using diabatic forcing of a simple AGCM. *Geophys Res Lett* 29:doi:10.1029/2001GL014,502
- Platzman GW (1968) The Rossby wave. *Quart J Roy Meteor Soc* 94:225–248
- Rao SA, Behera SK (2005) Subsurface influence on SST in the tropical Indian Ocean: Structure and interannual variability. *Dyn Atmos Oceans* 39:103–139
- Rayner NA, Parker DE, Horton EB, Folland CK, Alexander LV, Rowe DP, Kent EC, Kaplan A (2002) Global analyses of sea surface temperature, sea ice, and night marine air temperature since the late nineteenth century. *J Geophys Res* 108:D14
- Reason CJC (2002) Sensitivity of the southern African circulation to dipole sea-surface temperature patterns in the South Indian Ocean. *Int J Climatol* 20:377–393
- Rienecker MM, Suarez MJ, Gelaro R, Todling R, Bacmeister J, Liu E, Bosilovich MG, et al (2011) MERRA: NASA's Modern-Era Retrospective Analysis for Research and Applications. *J Clim* 24(14)
- Riviere G, Orlanski I (2007) Characteristics of the Atlantic storm track eddy activity and its relationship with the North Atlantic Oscillation. *J Atmos Sci* 64:241–266
- Robinson WA, Li S, Peng S (2003) Dynamical nonlinearity in the atmospheric response to Atlantic sea surface temperature anomalies. *Geophys Res Lett* 20, 2038
- Rogers J (1990) Patterns of low-frequency monthly sea level pressure variability (1899-1986) and associated wave cyclone frequencies. *J Clim* 3:1364–1379
- Rossby CG (1939) Relation between variations in the intensity of the zonal circulation of the atmosphere and the displacement of the semi-permanent centers of actions. *J Marine Res* 2:38–55
- Saji NH, Yamagata T (2003a) Possible impacts of Indian Ocean dipole mode events on global climate. *Clim Res* 25(2):151–169

- Saji NH, Yamagata T (2003b) Structure of SST and surface wind variability during Indian Ocean Dipole Mode years: COADS observations. *J Clim* 16:2735–2751
- Saji NH, Goswami BN, Vinayachandran PN, Yamagata T (1999) A dipole mode in the tropical Indian Ocean. *Nature* 401.6751:360–363
- Saji NH, Ambrizzi T, Ferraz SET (2005) Indian Ocean Dipole mode events and austral surface air temperature anomalies. *Dyn of Atm and Oc* 39(1):87–101
- Salby ML (1982) A Ubiquitous Wavenumber-5 Anomaly in the Southern Hemisphere During FGGE. *Mon Wea Rev* 110:1712–1720
- Sardeshmukh PD, Prashant D, Hoskins BJ (1987) The generation of global rotational flow by steady idealized tropical divergence. *J Atmos Sci* 45:1228–1251
- Schott FA, McCreary JP (2001) Physical oceanography of the Indian Ocean: from WOCE to CLIVA. *Progr Oceanogr* 51:1–123
- Schott FA, Xie SP, McCreary JP (2009) Indian Ocean circulation and climate variability. *Rev Geophys* 47:RG1002
- Schubert S, Wang H, Suarez M (2011) Warm season subseasonal variability and climate extremes in the Northern Hemisphere: The role of stationary Rossby waves. *J Clim* 24:4773–4792
- Selten FM (1995) An efficient description of the dynamics of barotropic flow. *J Atmos Sci* 52:915–936
- Selten FM, Branstator GW, Dijkstra HA, Kliphuis M (2004) Tropical origins for recent and future northern hemisphere climate change. *Geophys Res Lett* 31:L21,205
- Stocker TF, Qin D, Plattner GK, Tignor M, Allen SK, Boshing J, Nauels A, Xia Y, Box V, Midgley PM (2013) “Climate Change 2013: The Physical Science Basis.” Working Group I Contribution to the Fifth Assessment Report of the Intergovernmental Panel on Climate Change. (IPCC, 2013)
- Swapna P, Krishnan R, Wallace JM (2013) Indian Ocean and monsoon coupled interactions in a warming environment. *Clim Dyn* pp 1–16
- Thompson DWJ, Lee S, Baldwin M (2003) Atmospheric processes governing the Northern Hemisphere Annular Mode/North Atlantic Oscillation. *Geophys Monogr* 134:81–112
- Ting M (1996) Steady linear response to tropical heating in barotropic and baroclinic models. *Amer Meteor Soc* 53(12):1698–1709

- Tozuka T, Yokoi T, Yamagata T (2010) A modeling study of interannual variations of the Seychelles Dome. *J Geophys Res* 115:C04,005
- Trenary L, Han W (2012) Intraseasonal-to-interannual variability of South Indian Ocean sea level and thermocline: Remote versus local forcing. *J Phys Oceanogr* 42(4):602–627
- Trenberth KE, Branstator GW, Karoly D, Kumar A, Lau NC, Ropelewski C (1998) Progress during TOGA in understanding and modeling global teleconnections associated with tropical sea surface temperatures. *J Geophys Res* 103(C7):14,291–14,324
- Uppala SM, Kallberg PW, Simmons AJ, Andrae U, Bechtold V, Fiorino M, Gibson JK, et al (2005) The ERA-40 re-analysis. *Q J R Meteorol Soc* 131:2961–3012
- Vallis GK, Gerber EP, Kushner PJ, Cash BA (2004) A mechanism and simple dynamical model of the North Atlantic Oscillation and annular modes. *J Atmos Sci* 61:264–280
- Vecchi GA, Harrison DE (2004) Interannual Indian rainfall variability and Indian Ocean sea surface temperature anomalies. *Amer Geophys Union* 147:247–260
- Vialard J, Foltz G, McPhaden MJ, Duvel JP, de Boyer Montegut C (2008) Strong Indian Ocean sea surface temperature signals associated with the Madden-Julian Oscillation in late 2007 and early 2008. *Geophys Res Lett* 35(19)
- Vialard J, Duvel JP, McPhaden MJ, Bouruet-Aubertot P, Ward B, Key E, Bourras D, et al (2009) Cirene: Air-sea interactions in the Seychelles-Chagos thermocline ridge region. *Bull Amer Meteor Soc* 90(1)
- Wallace JM, Gutzler DS (1981) Teleconnections in the geopotential height field during the Northern Hemisphere winter. *Mon Wea Rev* 109:784–812
- Wang B, Ding Q, Fu X, Kang I, Jin K, Shukla J, Doblas-Reyes F (2005) Fundamental challenge in simulation and prediction of summer monsoon rainfall. *Geophys Res Lett* 32-15
- Wang SY, Hips FE, Gillies RR, Jiang X, Moller AL (2010) Circumglobal teleconnection and early summer rainfall in the US intermountain West. *Theor Appl Climatol* 102:245–252
- Watanabe M (2004) Asian jet waveguide and a downstream extension of the North Atlantic Oscillation. *J Clim* 17:4674–4691

- White WB (2000) Coupled Rossby Waves in the Indian Ocean on Inter-annual Timescales. *J Phys Oceanogr* 30:2972–2988
- Wu Z, Wang B, Li J, Jin FF (2009) An empirical seasonal prediction model of the East Asian summer monsoon using ENSO and NAO. *J Geophys Res Atm* 114(D18):1984–2012
- Xie SP, Arkin PA (1997) Global Precipitation: A 17-Year monthly analysis based on gauge observations, satellite estimates, and numerical model outputs. *Amer Meteor Soc* 78:2539–255
- Xie SP, Annamalai H, Schott FA, McCreary JP (2002a) Structure and mechanisms of south Indian Ocean climate variability. *J Clim* 15:867–878
- Xie SP, Annamalai H, Schott FA, McCreary JP (2002b) Structure and mechanisms of South Indian Ocean variability. *J Clim* 15:864–878
- Xie SP, Xu H, Saji NH, Wang Y, Liu WT (2006) Role of narrow mountains in large-scale organization of Asian monsoon convection. *J Clim* 19:3420–3429
- Yamagata T, Behera SK, Luo JJ, Masson S, Jury MR, Rao SA (2004) Coupled ocean-atmosphere variability in the tropical Indian Ocean. *Earth's Clim* pp 189–211
- Yang J, Liu Q, Liu Z, Wu L, Huang F (2009) Basin mode of Indian Ocean sea surface temperature and Northern Hemisphere circumglobal teleconnection. *Geophys Res Lett* 36:L19,705
- Yokoi T, Tozuka T, Yamagata T (2008) Seasonal variation of the Seychelles Dome. *J Clim* 21:3740–3754
- Yu JY, Mechoso CR, McWilliams JC, Arakawa A (2002) Impacts of Indian Ocean on ENSO cycles. *Geophys Res Lett* 29:1204
- Zangvil A, Yanai M (1980) Upper tropospheric waves in the tropics. Part I: Dynamical analysis in the wavenumber-frequency domain. *J Atmos Sci* 37:287–298
- Zappa G, Lucarini V, Navarra A (2011) Baroclinic stationary waves in aquaplanet models. *J Atm Sci* 68:1023–1040
- Zhang C (2005) Madden-Julian Oscillation. *Rev Geophys* 43(2)
- Zhou L, Murtugudde R, Jochum M (2008) Dynamics of the intraseasonal oscillations in the Indian Ocean South Equatorial Current. *J Phys Ocean* 38(1):121–132



# SUMMARY

The atmosphere is a sensitive and highly variable system and its state is crucial for the evolution and well being of all life on Earth. From the ever-recurring changes of the seasons to the most unpredicted extreme weather phenomena, the more we unravel the nature and mechanisms of the physical processes that govern this delicate but powerful system, the more we can benefit and advance towards better extended range forecasts and better understanding of the climate change signals.

The atmosphere often reacts vigorously to changes of its state and a local perturbation can influence the weather patterns sometimes even in the most remote regions. Some of those vast spanning patterns are recurring and persisting and are called teleconnections. The extratropical teleconnections can be understood in terms of large-scale waves in the velocity field of the atmosphere, such as the Rossby waves. The tropical teleconnections involve Rossby waves, as well as atmospheric and oceanic Kelvin waves and strong atmosphere-ocean interactions.

The objective of this dissertation is to better understand the interactions between the tropical forcing of Rossby waves and the tropical and extratropical response, with a focus on teleconnections that relate to the Indian Ocean, either directly or indirectly, as studies have shown that even the weather in Europe is influenced by variations in the Indian Ocean.

The propagation of Rossby waves is strongly influenced by the presence of a jet stream, that can act as a waveguide and enable a rapid transfer of wave energy around the hemisphere. Major jet streams are found in the upper troposphere of both hemispheres and they are characterized by fast and relatively narrow belts of westerly winds in the extra-tropics. The entrainment of a Rossby wave along the jet stream disturbs its zonal character, creating large meanders that are known as the major ridges and troughs of the midlatitudes, and influences strongly the weather as we know it, by steering air masses and weather systems. However, not all jets are able to trap and guide Rossby waves efficiently. Then, what are the characteristics of a jet stream that make it an efficient guide for Rossby waves?

The simplest model to address this question is a one-layer model that describes the dynamics of a barotropic atmosphere, i.e. an atmosphere in which the density of the air only depends on pressure and in which surfaces

of constant pressure are also surfaces of constant temperature. In this thesis we applied the barotropic vorticity equation to upper-tropospheric conditions and we systematically assessed the ability of idealized zonal jet streams to guide Rossby wave energy. The idealized jet streams had a Gaussian meridional profile and differed in width, speed and in meridional location. Rossby wave energy was generated by steady, idealized (sub-)tropical vorticity sources. These investigations led to the conclusion that a jet stream becomes a more efficient waveguide when it becomes faster and narrower. The response becomes maximum when the stationary zonal wave number is an integer and the wave propagates around the hemisphere. The zonal wave number becomes smaller when the jets are faster or when the jets are positioned closer to the poles. Finding strong evidence from observations to assert these findings proved not easy as the signal-to-noise ratio in the atmosphere is quite low. Nonetheless some observational support was found by analyzing observed wave-zonal flow relationships.

Among the most prominent extratropical teleconnections is the North Atlantic Oscillation (NAO). The NAO is a large north-south sea level pressure dipole over the North Atlantic that is related to changes in the position and strength of the jet stream and a displacement of the storm tracks. Depending on the state of the dipole the NAO is in a positive or negative phase with the positive phase corresponding to a stronger jet stream and more storms that propagate into central and Northern Europe and the negative phase corresponding to a weaker jet stream with storms deflected towards Southern Europe. During the positive phase the winters in Central and Northern Europe and Southeast USA are milder and wetter, while winters are drier and colder in Southern Europe, Northeast Canada and Greenland. Opposite weather conditions occur during the negative phase. The modification of the jet stream in each phase impacts the waveguiding properties and hence influences the formation and propagation characteristics of the Rossby waves. The NAO variability is primarily due to extratropical dynamics, such as breaking waves associated with extratropical weather systems, but is also influenced by Rossby waves generated at lower latitudes that propagate into the extratropics. In this thesis we assessed the influence of these signals on the NAO variations.

We set out to quantify the contribution of tropical and extratropical atmospheric forcing mechanisms to the formation of the NAO pattern. Although the NAO varies on a wide range of time scales, we focus on

10-60 days. At these time scales, mechanisms are at play in the atmosphere that can generate the characteristic dipole pattern. We focus on the tropical Rossby Wave Source (RWS) and extratropical eddy activity. Anomalous tropical and extratropical vorticity forcing associated with the NAO is derived from atmospheric reanalysis data and applied in an idealized barotropic model. Also, using winds from composites of the NAO, the vorticity forcing is derived inversely from the barotropic vorticity equation. Both types of forcing are imposed in the barotropic model in the tropics and extratropics, respectively. An important result is that the tropics dampen the NAO as a result of a negative feedback generated in the extratropics. The damping is strongest, about 30%, for the negative phase of the NAO. For the positive phase, the damping is about 50% smaller. The results show that the barotropic vorticity equation can represent the dynamics of both tropical and extratropical forcing related to the formation of the NAO patterns.

The scientific interest in the tropical Indian Ocean (IO) is growing as evidence accumulates of the importance of variations in the IO for the evolution of climate in the surrounding regions as well as for remote areas around the globe, as changes in the IO sea surface temperature (SST) influence the local convection and atmospheric circulation and impact tropical and extratropical teleconnection patterns. The IO atmosphere and ocean current systems are complex, undergo strong seasonal variations and a realistic modeling of these variations is challenging. A special feature is the thermocline ridge northeast of Madagascar, where the cold waters in the deeper ocean layers are close to the surface, a feature often referred to as the Seychelles Dome (SD). Variations in the thermocline depth in response to wind changes easily create SST changes that influence the atmosphere in turn leading to strong atmosphere-ocean interactions in this region. We set out to investigate the response of the coupled atmosphere-ocean system to a shallow SD event with the state-of-the-art fully coupled EC-Earth climate model. First the ability of the EC-Earth model to simulate the complex climatology of the IO was evaluated and then was applied to study the impact of SD variations on the rest of the climate system.

The climatology of a 40 year simulation of EC-Earth under year 2000 forcing conditions (solar, aerosol and greenhouse gases) was compared against observations. The spatial distribution of the wind, precipitation, sea-surface temperature and the thermal structure of the ocean is simulated rather realistically throughout the year. Biases are present, but the

important features are reproduced, including the Seychelles Dome with similarly strong correlations between thermocline depth variations and SST variations as observed, leading us to conclude that EC-Earth is a useful tool to study the detailed coupled ocean-atmosphere response to a shallow SD thermocline event.

We studied the response by conducting two ensemble experiments of 40 members each, a control and a perturbed ensemble. In the control ensemble, the coupled system was initialized in November from a neutral SD state and integrated for 26 months. The ensemble members lead to different evolutions by the introduction of random perturbations to the model state during the first day of integration. The perturbed ensemble differed only from the control ensemble in the application of a windstress anomaly over the SD region in order to raise the thermocline during the first two months. The differences between the two ensemble mean fields allowed us to study the response of the coupled system both locally and remotely. A strong local cooling of the SSTs drives subsidence and reduced precipitation. North of the SD, an equatorial downwelling adjustment region manifests as a pair of downwelling westward moving Rossby waves that warm up the Western-Equatorial IO and an eastward downwelling equatorial Kelvin wave. The combination of warm and cold SST anomalies over the equator and over the SD drive a northward shift in the Intertropical Convergence Zone (ITCZ) that in January extends over Central-East Africa influencing the precipitation there. The warming over the Western-Equatorial IO triggers atmospheric convection, resulting in a Walker-type response with reduced convection over the Indonesian warm pool and cooling of the SSTs in that region due to stronger surface winds. The Pacific warm pool convection shifts eastward and an oceanic Kelvin wave is triggered, that crosses equatorial Pacific and leads to SST warming in East equatorial Pacific in April. There the SST anomaly triggers weak anomalous atmospheric convection that is dissipated in the following month, as during this season the air-sea coupling is relatively weak and does not support unstable air-sea interactions. In response to the change in atmospheric convection in the Equatorial IO, atmospheric Rossby waves are emanated and are visible in the winter hemisphere waveguides. As these responses depend on the atmospheric state, their characteristics would be different for different timings of Seychelles doming event in the seasonal cycle as well. We suggest to repeat these kind of experiments with different climate models to study the model dependency of these results and choose different timings of the doming in the seasonal cycle to investigate

the possibility of triggering ENSO through the remote response in the Pacific.



# SAMENVATTING

De atmosfeer is een gevoelig en heel variabel systeem. De toestand waarin de atmosfeer zich bevindt is cruciaal voor de evolutie en het welbevinden van al het leven op Aarde. Van de altijd terugkerende seizoensveranderingen tot de meest onvoorspelbare extreme weerfenomenen, hoe meer we de mechanismen achter de fysische processen van dit delicate maar ook formidabele systeem ontrafelen, hoe meer vooruitgang we kunnen boeken met betere langetermijn weersverwachtingen en hoe beter we signalen die duiden op klimaatverandering kunnen begrijpen.

De atmosfeer is continu in reactie op veranderingen in haar toestand. Een locale verstoring kan de meest verafgelegen gebieden beïnvloeden en weerspatronen veranderen. Sommige van deze uitgestrekte patronen zijn terugkerend en persistent en worden aangeduid als teleconnecties. De extratropische teleconnecties kunnen worden opgevat als grootschalige golven in het snelheidsveld van de atmosfeer, zoals bijvoorbeeld de Rossby golven. De tropische teleconnecties omvatten zowel Rossby golven, als atmosferische en oceanische Kelvin golven en sterke atmosfeer-oceaan interacties.

Het doel van dit onderzoek is om meer begrip te krijgen van de interacties tussen Rossby golven opgewekt in de tropen en de tropische en extra-tropische respons op deze golven, waarbij de focus ligt op teleconnecties die gerelateerd zijn aan de Indische Oceaan, zowel direct als indirect, aangezien er uit wetenschappelijk onderzoek is gebleken dat het weer in Europa beïnvloed wordt door variaties in de Indische Oceaan.

De voortplanting van Rossby golven wordt sterk beïnvloed door de straalstroom, die als een golfgeleider kan fungeren voor Rossby golven en de energie van de golven snel rond de hemisfeer kan transporteren. De straalstroom is een relatief smalle oostwaartse luchtstroom die met hoge snelheid door de bovenste lagen van de troposfeer stroomt. Rossby golven in de straalstroom verstoren het zonale karakter, wat leidt tot grote meanders die bekend staan als de grote ruggen en troggen van de gematigde zone. Het locale weer wordt hierdoor sterk beïnvloed door de formatie van hoge en lage druk gebieden. Niet elke straalstroom is echter in staat om Rossby golven af te buigen en te geleiden. De vraag is nu, over welke karakteristieken moet een straalstroom beschikken om in staat te zijn een Rossby golf effectief te geleiden?

De meest eenvoudige manier om deze vraag te beantwoorden is om gebruik te maken van een enkellaags model onder de aanname van een equivalent barotrope atmosfeer, dat wil zeggen, een atmosfeer waarin de wind niet draait met de hoogte omdat isothermen en isobaren samenvallen zodat er geen temperatuursadvectie plaatsvindt. Met een dergelijk model dat de barotrope vorticieteits vergelijking oplost voor condities in de bovenste laag van de troposfeer hebben we op systematische wijze getest of een geïdealiseerde zonale straalstroom in staat is om Rossby golf energie in te vangen. De gesimuleerde straalstromen hadden een Gaussisch meridionaal profiel en verschilden in breedte, snelheid en in meridionale locatie. Rossby golf energie werd opgewekt door stationaire, geïdealiseerde (sub)-tropische vorticieteitsbronnen. We concluderen in dit proefschrift dat een straalstroom in het algemeen een efficiëntere “golfgeleider” is naarmate ze sneller en smaller is. De respons is maximaal als het zonaal stationaire golfgetal een geheel getal is en de golf de hele hemisfeer omloopt. Het zonale golfgetal wordt kleiner als de straalstroom sneller is, of als de straalstroom zich dichterbij de een van de polen bevindt. Het blijkt niet makkelijk om sterk bewijs uit observaties te vinden om onze bevindingen te bevestigen, daar de signaal-ruis verhouding in de atmosfeer tamelijk laag is. Desondanks gaan we ervan uit dat onze resultaten geldig zijn.

De Noord Atlantische Oscillatie (NAO) is een van de meest prominente extratropische teleconnecties. De NAO is een grote Noord-Zuid dipool in de luchtdruk op zeeniveau boven het Noord-Atlantisch gebied, die gerelateerd is aan veranderingen in de sterkte en de positie van de straalstroom en de bijbehorende stormbanen. In de positieve fase van de NAO met een sterker IJsland laag en Azoren hoog is de straalstroom sterker en noordwaarts verschoven met mildere en nattere winters in Noord-Europa, Scandinavië en Noordoost-Amerika en strengere, droge winters in Groenland, Zuid-Europa, Noord-Canada en het Midden-Oosten. In de negatieve fase zijn de veranderingen tegengesteld. De NAO variaties worden voornamelijk veroorzaakt door dynamische processen in de extra-tropen, zoals brekende golven die samengaan met extra-tropische weersystemen. Maar ook Rossby golven die opgewekt worden op lagere breedtes en zich voortplanting richting de extra-tropen kunnen aanleiding geven tot veranderingen in de NAO. In dit proefschrift hebben we de invloed van beide onderzocht.

Ons doel was de bijdrage aan de vorming van het NAO patroon te kwantificeren van beide forceringsmechanismes, de tropische en extra-tropische. Alhoewel de NAO varieert op alle tijdschalen focussen we op



variaties op 10-60 dagen. Op deze tijdschaal spelen de belangrijkste fysische processen in de atmosfeer zich af die het karakteristieke dipool patroon kunnen genereren, namelijk de tropische Rossby Wave Source (RWS) en de extra-tropische golfactiviteit. Uit atmosferische her-analyse gegevens leidden we de anomale tropische en extra-tropische vorticitetsforcering af van een anomale NAO toestand en pasten deze toe in een geïdealiseerd barotroop model van de atmosfeer. Ook bepaalden we de vorticitetsforcering met behulp van de barotrope vorticitetsvergelijking af door gebruik te maken van de winden van de gemiddelde anomale NAO toestand en de forcering uit te rekenen die deze toestand stationair maakte. Beide type forceringen pasten we toe in het barotrope model in respectievelijk alleen de tropen en alleen de extra-tropen. Een belangrijk resultaat is dat de tropen de NAO dempen als gevolg van een negatieve terugkoppeling die in de extra-tropen gegenereerd wordt. Deze demping is het sterkst, ongeveer 30%, voor de negatieve fase van de NAO. Voor de positieve fase is de demping ongeveer 50% kleiner. De resultaten laten zien dat de barotrope vorticitetsvergelijking de dynamica van zowel de tropische als de extra-tropische forcering van de NAO goed kan representeren.

De wetenschappelijke interesse in de tropische Indische Oceaan (IO) is groeiende doordat bewijzen zich opstapelen dat de variaties in de IO niet alleen een belangrijke invloed uitoefenen op het klimaat in de directe omliggende regio's maar ook in verafgelegen gebieden elders op de wereld. Veranderingen in de IO zeewatertemperaturen (SST) beïnvloeden namelijk de lokale convectie en atmosferische circulatie, die vervolgens via atmosferische en oceanische teleconnecties tot veranderingen leiden elders in de tropen en extra-tropen. De atmosferische en oceanische stromingspatronen in de IO zijn complex, veranderen sterk met de seizoenen en een realistische numerieke simulatie van deze stromingen vormt een grote uitdaging. Een speciaal fenomeen is de rug in de thermocliene ten noordoosten van Madagascar waar de koude wateren van de diepe oceaan dicht onder het oppervlak liggen, ook wel de "Seychellen Dome" genoemd (SD). Variaties in de diepte van de thermocliene als reactie op wind variaties leiden gemakkelijk tot SST variaties die de atmosfeer beïnvloeden en tot sterke atmosfeer-oceaan interacties leiden in deze regio. Ons doel was om de aanpassingen van het gekoppelde atmosfeer-oceaan systeem op een ondiepe SD gebeurtenis in detail te onderzoeken. We kozen als onderzoeksmiddel hiervoor het state-of-the-art klimaat model EC-Earth. Eerst hebben we onderzocht in hoeverre EC-Earth in staat is om de complexe klimatologie van de IO goed te beschrijven voordat we ermee de invloed

van SD variaties op het klimaatsysteem gingen onderzoeken.

De klimatologie van een 40 jaar durende simulatie van EC-Earth onder constante jaar-2000 forcering condities (zoals zonnestraling, aerosolen en broeikasgassen) is vergeleken met waarnemingen. De ruimtelijke verdeling van de wind, neerslag, zeewatertemperaturen en de thermische structuur van de oceaan worden tamelijk realistisch gesimuleerd gedurende de hele jaarlijkse gang. Er zijn ook behoorlijke afwijkingen, maar de belangrijke kenmerken worden goed gesimuleerd, zoals de SD met soortgelijke sterke correlaties tussen de diepte van de thermocliene en de waarde van de zeewatertemperatuur als in de waarnemingen. We concludeerden dat EC-Earth een geschikt onderzoeksmiddel is om de ocean-atmosfeer respons op een ondiepe SD gebeurtenis in detail te onderzoeken.

We onderzochten deze respons door twee ensemble experimenten van elk 40 leden uit te voeren, een controle ensemble en een verstoord ensemble. In het controle ensemble werd het gekoppelde systeem gestart in november vanuit een neutrale SD toestand en vervolgens voor 26 maanden geïntegreerd. De leden in het ensemble leidden tot verschillende ontwikkelingen doordat gedurende de eerste dag van de integratie toevallige verstoringen aan de model toestand werden toegevoegd. Het verstoorde ensemble verschilde enkel van het controle ensemble in de toepassing van een windstress anomalie in het SD gebied gedurende november en december om de thermocliene omhoog te brengen. De verschillen tussen de ensemble gemiddelde velden laten de respons van het gekoppelde ocean-atmosfeer systeem zien op de aangelegde windforcering als functie van de tijd. Een sterke lokale koeling van de zeewatertemperaturen leidt tot anomale subsidentie in de atmosfeer boven de SD en verminderde neerslag. Een verzwakking van de equatoriale opwelling ten noorden van de SD leidt tot de excitatie van een paar westwaarts voortbewegende Rossby golven, die na een maand de westelijke-equatoriale IO opwarmen, en een oostwaarts bewegende equatoriale kelvin golf. De combinatie van warme en koude zeewatertemperatuur anomalieën bij de equator en de SD veroorzaakt een noordwaartse verschuiving in de ITCZ die zich in januari over Centraal-Oost Africa uitstrekt en lokaal de neerslag beïnvloedt. Vanwege de opwarming in de westelijke equatoriale IO wordt atmosferische convectie versterkt met als resultaat een aanpassing in de Walker circulatie met gereduceerde convectie over de Indonesische warme wateren en afkoeling van de zeewater oppervlakte temperaturen in dat gebied vanwege sterkere oppervlakte winden. De convectie over het warme water van de Westelijke Pacific verschuift oostwaarts en slaat een oceanische

Kelvin golf aan in de thermocliene. De golf steekt de equatoriale Stille Oceaan over en leidt tot opwarming van de zeewatertemperatuur in de oostelijk equatoriale Stille Oceaan in April. Deze opwarming leidt tot zwakke anomale atmosferische convectie, die in de daaropvolgende maand verdwijnt aangezien de lucht-zee koppeling in dit seizoen relatief zwak is en geen instabiele lucht-zee interacties mogelijk maakt. Ten gevolge van de verandering in atmosferische convectie in de equatoriale IO, worden atmosferische Rossby golven opgewekt die zichtbaar zijn in de winter halfrond golf-geleiders. Aangezien de beschreven aanpassingen op de lokale afkoeling in de SD regio afhangen van de atmosferische toestand op dat moment, verwachten we dat de respons verschillend is als het SD event op een ander moment in de seizoenscyclus plaatsvindt met mogelijke effecten op de timing van de Indische monsoon en El Niño. We doen de aanbeveling om deze experimenten te herhalen met verschillende klimaatmodellen om inzicht te krijgen in de model afhankelijkheid van de resultaten en om de thermocliene op te tillen in verschillende fases van de seizoenscyclus om de mogelijkheid te onderzoeken dat een SD gebeurtenis een El Niño gebeurtenis triggert door de respons in de Stille Oceaan.



## ΠΕΡΙΛΗΨΗ

Η ατμόσφαιρα είναι σύστημα εξαιρετικά ευμετάβλητο και η κατάσταση στην οποία βρίσκεται είναι πολύ σημαντική για την εξέλιξη της ζωής και την ευημερία στη γη. Από τις αέναες αλλαγές των εποχών, μέχρι τα πιο απρόβλεπτα ακραία καιρικά φαινόμενα, όσο περισσότερο ξεδιπλώνουμε τα μυστικά των μηχανισμών των φυσικών διαδικασιών που διέπουν αυτό το ευαίσθητο αλλά πανίσχυρο σύστημα, τόσο περισσότερο μπορούμε να επωφεληθούμε και να βελτιώσουμε τις μακροπρόθεσμες καιρικές προβλέψεις και να κατανοήσουμε καλύτερα τις κλιματικές αλλαγές.

Η ατμόσφαιρα συχνά αντιδρά έντονα σε αλλαγές της κατάστασης της και κάποιες φορές μια τοπική διαταραχή μπορεί να μεταβάλλει τα καιρικά συστήματα ακόμα και στις πιο απομακρυσμένες περιοχές. Κάποια από αυτά τα συστήματα είναι μεγάλης κλίμακας, εμμένουν και επαναλαμβάνονται και ονομάζονται “ηλεκτρονικές”. Οι εξωτροπικές ηλεκτρονικές μπορούν να κατανοηθούν με όρους ατμοσφαιρικών κυμάτων μεγάλης κλίμακας στο πεδίο των ταχυτήτων, όπως είναι τα κύματα Rossby. Οι ηλεκτρονικές των τροπικών ζωνών, εκτός από κύματα Rossby, περιλαμβάνουν επίσης ατμοσφαιρικά και ωκεάνια κύματα Kelvin και ισχυρές αλληλεπιδράσεις μεταξύ ωκεανών και ατμόσφαιρας.

Ο κύριος στόχος αυτής της διατριβής είναι η καλύτερη κατανόηση των αλληλεπιδράσεων των τροπικών ηγών κυμάτων Rossby και των επιπτώσεων τους στις τροπικές και εξωτροπικές ζώνες, εστιάζοντας σε ηλεκτρονικές που σχετίζονται άμεσα ή έμμεσα με τον Ινδικό Ωκεανό, καθώς μελέτες δείχνουν ότι ακόμα και ο καιρός στην Ευρώπη μπορεί να επηρεαστεί από μεταβολές στον Ινδικό Ωκεανό.

Η διάδοση των κυμάτων Rossby στην ατμόσφαιρα επηρεάζεται έντονα από την παρουσία του αεροχειμάρρου, ο οποίος μπορεί να λειτουργεί σαν κυματοδηγός και να μεταφέρει ταχύτατα την ενέργεια του κύματος γύρω από το ημισφαίριο. Οι αεροχειμάρροι είναι στενές ζώνες ισχυρών δυτικών ανέμων που βρίσκονται στην ανώτερη τροπόσφαιρα και των δύο ημισφαιρίων, κυρίως στις εξωτροπικές περιοχές. Οι αεροχειμάρροι έχουν ζωνικό χαρακτήρα, ο οποίος όμως διαταράσσεται από την παγίδευση κυμάτων Rossby κατά μήκος τους, δημιουργώντας στα μέσα γεωγραφικά πλάτη καμπυλώσεις γνωστές ως ράχες υψηλών πιέσεων ή ως κοίλα, δηλαδή ζώνες χαμηλού βαρομετρικού. Οι καμπυλώσεις αυτές επηρεάζουν έντονα τον καιρό μας, καθώς “ανακατεύουν” τις αέριες μάζες και τα καιρικά συστήματα. Παρόλα αυτά δεν έχουν όλοι οι

αεροχειμάρροι την ίδια δυνατότητα να παγιδεύουν κύματα Rossby το ίδιο αποτελεσματικά. Τότε λοιπόν ποια είναι τα χαρακτηριστικά του αεροχειμάρρου που τον κάνουν πιο αποτελεσματικό Rossby κυματοδηγό;

Ο απλούστερος τρόπος να προσεγγίσουμε το παραπάνω πρόβλημα είναι να χρησιμοποιήσουμε ένα μοντέλο μονής επιφάνειας που να περιγράφει το δυναμικό σύστημα μια βαροτροπικής ατμόσφαιρας, δηλαδή μιας ατμόσφαιρας που η πυκνότητα του αέρα εξαρτάται μόνο από την πίεση και που οι ισοβαρικές επιφάνειες είναι επίσης και ισόθερμες. Εφαρμόσαμε τη βαροτροπική εξίσωση του στροβιλισμού σε συνθήκες ανώτερης τροπόσφαιρας και εξετάσαμε συστηματικά την ικανότητα ιδεατών αεροχειμάρρων να παγιδεύουν και να οδηγούν την ενέργεια των κυμάτων Rossby. Οι ιδεατοί αεροχειμάρροι είχαν Γκαουσιανό μεσημβρινό προφίλ, ενώ κάθε φορά διέφεραν στο πάχος, την ταχύτητα και το γεωγραφικό πλάτος τοποθέτησης τους. Η δημιουργία της ενέργειας των κυμάτων Rossby έγινε από σταθερές ιδεατές (υπο)τροπικές πηγές στροβιλισμού. Το συμπέρασμα της έρευνας υποδεικνύει ότι ο αεροχειμάρρος γίνεται πιο αποτελεσματικός κυματοδηγός όσο γίνεται πιο στενός και πιο γρήγορος. Η απόκριση γίνεται μέγιστη όταν το κύμα μεταφέρεται γύρω από ολόκληρο το ημισφαίριο και ο σταθερός ζωνικός κυματαριθμός είναι αχέραιος. Ο ζωνικός κυματαριθμός παίρνει μικρότερες τιμές όσο ο αεροχειμάρρος γίνεται ταχύτερος ή όσο αυτός μεταφέρεται προς βορειότερα γεωγραφικά πλάτη. Το να βρούμε στοιχεία από παρατηρήσεις στην ατμόσφαιρα που να αποδεικνύουν τα παραπάνω λεγόμενα δεν αποδείχτηκε εύκολη υπόθεση, καθώς η αναλογία μεταξύ σήματος και θορύβου είναι ιδιαίτερα μικρή. Παρόλα αυτά υπάρχουν κάποιες παρατηρησιακές ενδείξεις που στηρίζουν τη συσχέτιση μεταξύ κύματος και ζωνικής κυκλοφορίας.

Μεταξύ των πιο σημαντικών εξωτροπικών τηλεσυνδέσεων βρίσκουμε την Κύμανση του Βορείου Ατλαντικού (NAO). Το NAO είναι ένα μεγάλης κλίμακας βόρειο-νότιο δίπολο επιφανειακής ατμοσφαιρικής πίεσης που σχετίζεται με αλλαγές στη θέση και την ισχύ του αεροχειμάρρου και με μετατοπίσεις της τροχιάς των καταιγίδων. Ανάλογα με την κατάσταση του δίπολου το NAO βρίσκεται στην θετική ή την αρνητική του φάση. Η θετική φάση αντιστοιχεί σε ένα ισχυρότερο αεροχειμάρρο και περισσότερες καταιγίδες που κινούνται προς την κεντρική και Βόρεια Ευρώπη, ενώ η αρνητική φάση αντιστοιχεί σε ένα πιο αδύναμο αεροχειμάρρο, ενώ η τροχιά των καταιγίδων εκτρέπεται προς τη Νότια Ευρώπη. Κατά τη διάρκεια της θετικής φάσης οι χειμώνες στην Κεντρική και Βόρεια Ευρώπη και στις Νοτιοανατολικές ΗΠΑ είναι πιο ήπιοι και υγροί, ενώ οι χειμώνες στη Νότια Ευρώπη, το Βορειοανατολικό Καναδά και τη Γριλανδία είναι πιο ψυχροί και ξηροί. Τα αντίθετα καιρικά φαινόμενα παρατηρούνται κατά την αρνητική φάση του NAO. Η τροποποίηση του αε-

ροχειμάρρου σε κάθε φάση επιδρά στις κυματοδηγικές του ικανότητες και ως εκ τούτου επηρεάζει τη δημιουργία και τα χαρακτηριστικά διάδοσης των κυμάτων Rossby. Η μεταβλητότητα του NAO οφείλεται κατά κύριο λόγο σε εξωτροπικά δυναμικά συστήματα, όπως για παράδειγμα το σπάσιμο των ατμοσφαιρικών κυμάτων που σχετίζονται με εξωτροπικά καιρικά συστήματα. Επηρεάζεται όμως και από κύματα Rossby που έχουν δημιουργηθεί σε μικρότερα και μεταδίδονται προς τα μεγαλύτερα γεωγραφικά πλάτη. Σε αυτή τη διατριβή ερευνούμε την επίδραση των τροπικών και εξωτροπικών σημάτων στην μεταβλητότητα του NAO.

Σκοπεύουμε να προσδιορίσουμε την επιρροή των τροπικών και των εξωτροπικών δυνάμεων στη δημιουργία των σχηματισμών του NAO. Παρόλο που η μεταβλητότητα του NAO ποικίλει σε χρονικές κλίμακες, εμείς εστιάζουμε στην κλίμακα των 10 – 60 ημερών. Σε αυτή την κλίμακα υπάρχουν μηχανισμοί που δημιουργούν το χαρακτηριστικό διπολικό σχηματισμό. Εστιάζουμε στις τροπικές πηγές κυμάτων Rossby και στην εξωτροπική δραστηριότητα των στροβίλων. Η τροπική και εξωτροπική ώθηση στροβιλισμού που σχετίζεται με το NAO προέρχεται από δεδομένα “reanalysis” και υποβάλλεται σε ένα ιδεατό βαροτροπικό μοντέλο. Η ώθηση του στροβιλισμού έχει εξαγεί ανάστροφα, λύνοντας την εξίσωση του βαροτροπικού στροβιλισμού, χρησιμοποιώντας σύνθεση δεδομένων ανέμου από το NAO. Και τα δυο ήδη ώθησης (τροπικής και εξωτροπικής) εισήχθησαν στο βαροτροπικό μοντέλο στα τροπικά και στα εξωτροπικά γεωγραφικά πλάτη αντίστοιχα. Ένα σημαντικό αποτέλεσμα ήταν ότι η δράση των τροπικών μειώνει την ένταση του NAO, σαν αποτέλεσμα αρνητικής ανταπόκρισης που δημιουργείται στους εξωτροπικούς. Η άμβλυση είναι μεγαλύτερη, περίπου 30%, κατά την αρνητική φάση του NAO. Κατά τη θετική φάση είναι κατά 50% περίπου μικρότερη. Τα αποτελέσματα δείχνουν ότι η εξίσωση του βαροτροπικού στροβιλισμού μπορεί να αναπαραστήσει το δυναμικό σύστημα και των τροπικών αλλά και των εξωτροπικών δυνάμεων που δημιουργούν τους σχηματισμούς του NAO.

Το επιστημονικό ενδιαφέρον για τον Ινδικό Ωκεανό (ΙΩ) μεγαλώνει καθώς πληθαίνουν οι αποδείξεις για τη σπουδαιότητα της μεταβλητότητας του ΙΩ στην εξέλιξη όχι μόνο του κλίματος των γύρω περιοχών, αλλά ακόμα και απομακρυσμένων περιοχών στην υδρόγειο, καθώς αλλαγές στη θερμοκρασία στην επιφάνεια της θάλασσας μπορούν να επηρεάσουν την ατμοσφαιρική σύγκληση και την ατμοσφαιρική κυκλοφορία και να επιδράσουν στις τροπικές και τις εξωτροπικές τηλεσυνδέσεις. Η ατμόσφαιρα και τα ωκεάνια ρεύματα του ΙΩ είναι περίπλοκα και υφίστανται ισχυρές εποχιακές μεταβολές, και γι’ αυτό το λόγο η μοντελοποίηση της μεταβλητότητας του αποτελεί πρόκληση. Ένα ιδιαίτερο χαρακτηριστικό είναι η “ράχη” του θερμοκλινούς

του ωκεανού στα βορειοανατολικά της Μαδαγασκάρης, όπου κρύα νερά απο τα βαθύτερα στρώματα της θάλασσας ανεβαίνουν κοντά στην επιφάνεια, και συναντάται με το όνομα “ο θόλος των Σεύχελλων” (SD). Μεταβολές στον επιφανειακό ανέμο ή η έλευση ανοδικών και καθοδικών ωκεάνιων κυμάτων μπορούν να μεταβάλλουν το βάθος του θερμοκλινούς. Οι μεταβολές αυτές μπορούν εύκολα να επηρεάσουν την ατμοσφαιρική θερμοκρασία στην επιφάνεια της θάλασσας, και αυτό με τη σειρά του μπορεί να οδηγήσει σε ισχυρές αλληλεπιδράσεις μεταξύ ωκεανού και ατμόσφαιρας στην περιοχή. Σκοπός μας είναι να εξετάσουμε την αντίδραση του συζευγμένου συστήματος ωκεανού-ατμόσφαιρας στην εμφάνιση ενός ρηχού SD περιστατικού, χρησιμοποιώντας το πλήρως συζευγμένο κλιματικό μοντέλο τελευταίας τεχνολογίας, EC-Earth. Ξεκινάμε εξετάζοντας την ικανότητα του μοντέλου EC-Earth να αναπαραστήσει επιτυχώς το πολύπλοκο σύστημα του ΙΩ και στη συνέχεια μελετούμε την επίδραση των μεταβολών του SD στο γενικότερο κλιματικό σύστημα.

Για την εξέταση του μοντέλου EC-Earth η μέση κλιματική κατάσταση προσομοιώσεων 40 ετών συγκρίθηκε με παρατηρήσεις. Το μοντέλο έτρεχε κάτω από σταθερές συνθήκες του έτους 2000 (ηλίου, αερολιμμάτων και αερίων του θερμοκηπίου). Η χωρική κατανομή του ανέμου, της βροχόπτωσης, της ατμοσφαιρικής θερμοκρασίας στην επιφάνεια της θάλασσας, καθώς επίσης και η θερμική δομή του ωκεανού προσομοιώθηκαν αρκετά ρεαλιστικά καθ’ όλη τη διάρκεια του έτους. Παρατηρήθηκαν ασυμφωνίες, αλλά τα σημαντικά χαρακτηριστικά αναπαραστήθηκαν σωστά, συμπεριλαμβανομένου και του θόλου των Σεύχελλων, που παρουσίασε παρομοίως ισχυρή συσχέτιση με τις παρατηρήσεις μεταξύ του βάθους του θερμοκλινούς και των κυμάνσεων της ατμοσφαιρικής θερμοκρασίας στην επιφάνεια της θάλασσας. Τα παραπάνω οδήγησαν στο συμπέρασμα ότι το μοντέλο EC-Earth μπορεί να αποτελέσει χρήσιμο εργαλείο για την έρευνα της αντίδρασης του συζευγμένου συστήματος ωκεανού και ατμόσφαιρας στην εμφάνιση ενός ρηχού SD περιστατικού.

Την αντίδραση σε ένα SD περιστατικό εξετάσαμε μέσω δύο συλλογικών (ensemble) πειραμάτων 40 μελών το κάθε ένα, όπου το ένα σύνολο ήταν ελεγχόμενο και το άλλο είχε δεχτεί ώθηση. Στο πρώτο σύνολο των ελεγχόμενων προσομοιώσεων το συζευγμένο σύστημα ξεκινά το μήνα Νοέμβρη, με το SD να βρίσκεται σε ουδέτερη φάση, και προσομοιώνει τους επόμενους 26 μήνες. Το κάθε μέλος της προσομοίωσης εξελίσσεται λίγο διαφορετικά, καθώς εισάγονται τυχαίες αναταράξεις την πρώτη μέρα εκκίνησης της προσομοίωσης. Το δεύτερο σύνολο διαφέρει από το πρώτο μόνο στην εισαγωγή τύρβης ανέμου πάνω στην περιοχή του θόλου των Σεύχελλων, με σκοπό το



θερμοκλινές να γίνει πιο ρηχό κατά τους πρώτους 2 μήνες της προσομοίωσης. Εξετάζοντας τις διαφορές μεταξύ των δύο αυτών συνόλων μπορούμε να μελετήσουμε την αντίδραση του συζευγμένου συστήματος σε τοπικό και απομακρυσμένο επίπεδο. Παρατηρήθηκε ισχυρή πτώση της ατμοσφαιρικής θερμοκρασίας στην επιφάνεια της θάλασσας, που δημιούργησε μειωμένη ατμοσφαιρική αστάθεια και συνεπώς μείωση της βροχοπτώσης. Βόρεια του SD το ισημερινό θερμοκλινές για να προσαρμοστεί αναγκάζεται να βυθιστεί, γεγονός που δημιουργεί ένα ζεύγος ωκεάνιων κυμάτων Rossby που κινούνται καθοδικά προς τα δυτικά και θερμαίνουν τον Δυτικό-Ισημερινό ΙΩ, καθώς επίσης και ένα καθοδικό κύμα Kelvin που κινείται προς τα ανατολικά. Ο συνδυασμός της θερμής και ψυχρής ανωμαλίας στον Ισημερινό και πάνω από την SD περιοχή αντίστοιχα μετατοπίζουν βόρεια τη διατροπική ζώνη σύγκλισης, όπου τον Ιανουάριο εκτείνεται μέχρι την Κεντρική-Ανατολική Αφρική, επηρεάζοντας εκεί τη βροχοπτώση. Η ανώμαλη θέρμανση του Δυτικού-Ισημερινού ΙΩ πυροδοτεί φαινόμενα ατμοσφαιρικής σύγκλισης, με αποτέλεσμα μια ανωμαλία τύπου κυττάρου Walker, προκαλώντας μειωμένη ατμοσφαιρική αστάθεια πάνω από την Ινδονησία και τη θερμή λεκάνη του Δυτικού Ειρηνικού, και ψυχρότερες θερμοκρασίες στην ίδια περιοχή λόγω ισχυρότερων επιφανειακών ανέμων. Η ατμοσφαιρική σύγκλιση πάνω από τη θερμή λεκάνη του Δυτικού Ειρηνικού μετατοπίζεται ανατολικά και εγείρει ένα ωκεάνιο κύμα Kelvin. Το κύμα διασχίζει τον Ειρηνικό ωκεανό και οδηγεί κατά τον Απρίλιο σε άνοδο της ατμοσφαιρικής θερμοκρασίας στην επιφάνεια της θάλασσας στον Ανατολικό Ισημερινό Ειρηνικό. Εκεί, εξ' αιτίας της θερμικής ανωμαλίας δημιουργείται ατμοσφαιρική αστάθεια, που όμως είναι σχετικά αδύναμη και εξανεμίζεται τον επόμενο μήνα. Αυτό συμβαίνει επειδή η σύζευξη ωκεανού και ατμόσφαιρας τη συγκεκριμένη εποχή είναι σχετικά αδύναμη και δεν υποστηρίζει ασταθείς αλληλεπιδράσεις μεταξύ ωκεανού και ατμόσφαιρας. Ως αντίδραση στις αλλαγές στην ατμοσφαιρική αστάθεια πάνω από τον Ισημερινό ΙΩ ατμοσφαιρικά κύματα Rossby εγείρονται και γίνονται ορατά στους κυματοδηγούς των χειμερινών ημισφαιρίων. Καθώς οι παραπάνω μεταβολές εξαρτώνται από την κατάσταση της ατμόσφαιρας, τα χαρακτηριστικά τους θα διέφεραν εάν το SD περιστατικό συνέβαινε σε άλλη στιγμή του έτους. Προτείνουμε την επανάληψη πειραμάτων σαν και αυτό χρησιμοποιώντας διαφορετικά κλιματικά μοντέλα, ώστε να εξεταστεί η εξάρτηση των αποτελεσμάτων από τα μοντέλα. Επίσης προτείνουμε την επανάληψη τέτοιων SD περιστατικών σε διαφορετικές περιόδους του ετήσιου κύκλου, ώστε να διερευνηθεί η πιθανότητα πυροδότησης ενός φαινομένου Ελ Νίνιο-Νότιας Ταλάντωσης (ENSO) μέσω απομακρυσμένης απόκρισης του Ειρηνικού ωκεανού.



# ACKNOWLEDGEMENTS

Completing a doctorate thesis is a challenging task, full of contrasts. Parts of it are filled with unprecedented difficulties and doubts, while others are filled with excitement, positive energy and the precious joy that comes through gaining new knowledge. Giving me the opportunity to become a PhD student at KNMI, in beautiful Utrecht, was a milestone in my life. I had the chance to improve my skills in a highly appreciated environment and to become more patient and insistent as a person. At the same time living abroad and working with people from every corner of this world was an open minded experience and taught to me to be more kind, understanding and conciliatory. Without these magnificent people I would have never managed to fulfill this demanding task.

First and foremost I would like to thank Frank Selten, my first supervisor, who stood by me like family. He showed me the way and encouraged me and was always keeping a sense of humor when I had lost mine. My gratitude and appreciation to Wilco Hazeleger, my second supervisor, and to Will de Ruijter, my promotor, for their valuable contribution to my work and the fruitful discussions. My deep appreciation goes out to my colleagues at the Global Climate division of KNMI, and especially to Rein, Hylke, Richard and Camiel for the inspiring conversations, the technical support and assistance, but also for the fun moments we shared at KNMI corridors and the 10:15 coffee breaks with the stroopwafel tradition.

This Ph.D. would not have been possible without the funding from NWO for the INATEX project. I gratefully acknowledge the anonymous reviewers who read and evaluated my journal papers, leading to their considerable improvement. My gratitude also goes to the members of my dissertation committee who provided their time and expertise to validate and improve this thesis.

During my Ph.D. studies I made some friends for life. Thank you Sara, my paranymp, and Martina, my paranymp in heart, for just being your wonderful selves, for all the fun, the support, the stories we shared and the positive energy. Thank you Kosta and Marina for making me feel like home. Lucinda, Luca, little snoepje, Alessandro, Jessica, Carlo, Elodie and Julius our lunchtime together and the afterwards amusing discussions at Sara's office made my hard-working days more pleasant. I would also like to thank Andrea, Audine, Helio and Renske who were there before

me and were the first friendly welcome at KNMI.

Aleko, you were the best flatmate. Our laughs and discussions made my staying in Parkstraat memorable. Stavro, Suzette, Stella, Michali, Ana, Yianni, Keterina, Niko, Dewi thank you for your good company and for all those great music and dance nights. To just-married Niko and Anastasia, with whom we spent many relaxed weekends in Eindhoven, I would like to wish a future even more wonderful than they ever dreamed possible.

The establishment of our theater group AMITU had been of great importance for me in these past years. The time we spend together was great, we worked as a team, we bonded and put up some fun improvisation shows. It was a great creativity lesson for me.

A special thanks goes out to my good old friends in Greece who were always showing me their support, even from that far. Especially to Labrini, Lily and Efi, you know that your friendship is of the most valuable things in my life.

I would like to say a heartfelt thank you to my mother, who encouraged me to follow my dreams, to my father, to whom I owe my love for physics, to Nelly and Dinos, who are just the best sister and brother ever, to my Ralou, who is still forgiving me every time I have to leave her back, to Vivi and to our new family member, Promitheas, who is the prettiest and smartest of all kids.

A very special part of these past years was meeting my partner Ioannis. During our concurrent drive to our doctorate degrees, our understanding and support to each other had been a great comfort and relief in times of worrying, as he was making my days brighter and full of love.

# CURRICULUM VITAE



Iris Manola was born on 9 September 1982, in Athens, Greece. She got her primary and secondary education at the schools of Kaisariani. From an early age she was enthusiastic about nature and was curious about its functions and mechanisms. Her passion drove her to study physics at the University of Athens. Her graduation research project was on the energy efficiency in office buildings.

She continued her education at the University of Athens, where, in 2009, she got a Master's degree on environmental physics. Her thesis was about the impact of orography in the distribution of extreme dry and wet spells in Greece.

After that, she moved to Utrecht, in the Netherlands, to continue with a Ph.D. at the global climate division of KNMI, and to get her diploma in 2014 from the University of Utrecht. The subject was on large scale weather patterns and their tropical origins. The motivation, methodology and results of this research are presented in the current dissertation. During her Ph.D. studies she attended her first scientific conferences and wrote her first journal papers.

Her next professional steps will be a surprise.

